

Precious Metal-free Dye-sensitized Solar Cells

by

Hafeez Anwar

**Submitted in partial fulfilment of the requirements
for the degree of Doctor of Philosophy**

at

Dalhousie University

Halifax, Nova Scotia

November 2013

© Copyright by Hafeez Anwar, 2013

DEDICATIONS

This thesis is affectionately dedicated to my brothers and sisters for their gracious guardianship and encouragement, to my mother for her prayers, to my late father who is and will be a source of inspiration for me and to my wife and son (Ibrahim Anwar) for their support during this work.

TABLE OF CONTENTS

LIST OF TABLES	vii
LIST OF FIGURES.....	viii
ABSTRACT.....	xiii
LIST OF ABBREVIATIONS AND SYMBOLS USED	xiv
ACKNOWLEDGEMENTS.....	xvii
CHAPTER 1 INTRODUCTION.....	1
1.1. PHOTOVOLTAIC TECHNOLOGIES.....	3
1.1.1. First generation solar cells.....	4
1.1.2. Second generation solar cells.....	5
1.1.2.1. a-Si/ μ c-Si solar cells	5
1.1.2.2. CdTe solar cells.....	6
1.1.2.3. CI(G)S solar cells.....	6
1.1.3. Third generation solar cells	6
1.1.3.1. Concentrating PV (CPV)	6
1.1.3.2. Organic solar cells (OSCs).....	7
1.1.3.3. Dye-sensitized solar cells (DSSCs).....	8
1.2. AIR MASS AND THE SOLAR SPECTRUM.....	8
1.3. MOTIVATION.....	10
1.4. A NOTE ON THE SUSTAINABILITY OF PT AND RU.....	13
1.4.1. Calculations for Pt	13
1.4.2. Calculations for Ru.....	13
CHAPTER 2 STRUCTURE AND WORKING PRINCIPLES OF DSSCS.....	15
2.1. STRUCTURE OF DYE-SENSITIZED SOLAR CELL (DSSC)	15
2.2. OPERATING PRINCIPLE OF THE DYE-SENSITIZED SOLAR CELL.....	16
2.3. DSSC AND CONVENTIONAL P-N JUNCTION SOLAR CELL	18
2.4. RECOMBINATION PROCESSES/LOSSES.....	18
2.4.1. Reaction 1 (Absorption).....	19
2.4.2. Reaction 2 (Electron injection).....	20
2.4.3. Reaction 3 (Electron transport).....	22
2.4.4. Reaction 4 (Triiodide reduction)	23
2.4.5. Reaction 5 (Regeneration of dye)	24
2.4.6. Reactions 6, 7 and 8 (Recombination).....	24
2.5. PERFORMANCE EVALUATION OF DSSC.....	25
2.5.1 Short-circuit current density (J_{SC}).....	25

2.5.2	Open-circuit potential (V_{OC})	26
2.5.3	Maximum power point (MPP)	26
2.5.4	Fill factor (FF).....	26
2.5.5	Power conversion efficiency (η)	27
CHAPTER 3 BACKGROUND ON CARBON NANOTUBES (CNTS)		28
3.1.	CARBON NANOTUBES (CNTS).....	28
3.2.	SYNTHESIS ROUTES/METHODS.....	29
3.2.1.	Arc-discharge.....	29
3.2.2.	Laser Ablation.....	30
3.2.3.	Chemical vapor deposition (CVD).....	31
3.3.	VERTICALLY-ALIGNED CNTs (VACNTs) GROWTH	32
3.3.1	Growth mechanism of CNTs.....	32
3.4.	2-D CNT THIN FILMS AND THICK PAPERS.....	34
3.4.1	Preparation of CNT Films.....	34
CHAPTER 4 EXPERIMENTAL METHODS		36
4.1.	FABRICATION OF NORMAL DSSC	36
4.1.1	Preparation of photoanode.....	36
4.1.1.1	Substrates	36
4.1.1.2	Depositing the TiO ₂ layer	36
4.1.1.3	Dye impregnation of the electrodes	38
4.1.2	Preparation of counter electrode	38
4.1.3	Sealing the cell and filling of electrolyte	39
4.1.4	Further modifications to the cell design.....	40
4.2.	CARBON NANOTUBES (CNTS).....	42
4.2.1	Preparation of CNT thin films and CNT thick papers	42
4.2.2	Growth of vertical aligned carbon nanotubes (VACNTs) directly on substrates	42
4.2.2.1	Carbon nanotube synthesis considerations and challenges	43
4.2.2.2	Methods of synthesis.....	44
4.2.2.3	Substrates	44
4.2.2.4	Catalysts.....	44
4.2.2.5	Methods of catalyst preparation	45
4.2.3	CNTs CVD growth Procedures	45
4.2.3.1	Method 1 (CVD growth of CNTs using NH ₃ and C ₂ H ₄).....	45
4.2.3.2	Method 2 (CVD growth of CNTs using carbon monoxide and hydrogen)	46
4.2.3.3	Method 3 (CVD growth of CNTs using methanol and hydrogen)	47
4.2.3.4	Method 4 (WA-CVD growth of CNTs using ethylene and hydrogen)	48

4.3.	NANOCRYSTALLINE CELLULOSE (NCC).....	49
4.3.1	Counter electrodes for DSSC	49
4.3.2	Pyrolysis	50
4.4.	CHARACTERIZATION TECHNIQUES USED	50
4.4.1	Electrochemical impedance spectroscopy (EIS).....	50
4.4.2	Cyclic Voltammetry (CV).....	53
4.4.3	Scanning electron microscopy (SEM)	54
4.4.4	Small angle x-ray scattering (SAXS)	55
4.4.5	X-ray photoelectron spectroscopy (XPS).....	57
4.4.6	Mercury drop method for resistance measurements.....	58
4.4.7	Thermal gravimetric analysis (TGA).....	59
4.4.8	Atomic force microscopy (AFM).....	60
	CHAPTER 5 PRELIMINARY WORK.....	62
5.1.	OPTIMIZATION OF NORMAL DSSCS.....	62
5.1.1.	DSSC Testing Revisited	65
5.1.2.	DSSCs with TiCl ₄ treatment	66
5.2.	A NOTE ON ERROR ANALYSIS OF PERFORMANCE MEASURING PARAMETERS	68
5.3.	CNT THIN FILMS AND THICK PAPERS.....	68
5.4.	CONCLUSIONS.....	72
	CHAPTER 6 APPLICATION OF CVD CNTS IN DSSCS	73
6.1.	INTRODUCTION	73
6.2.	CNTS GROWTH (VARIOUS SYNTHESIS METHODS ON VARIOUS SUBSTRATES)	74
6.3.	DSSCS WITH CNT COUNTER ELECTRODES BY THE MEOH CVD METHOD.....	80
6.4.	GROWTH OF CNTS USING THE WATER ASSISTED METHOD (WA-CVD).....	82
6.4.1.	Synthesis	82
6.4.2.	Characterization.....	82
6.4.2.1.	Scanning electron microscopy (SEM)	82
6.4.3.	DSSC fabrication and characterization.....	83
6.4.3.1.	Current density-voltage measurements (J-V curves)	84
6.4.3.2.	Electrochemical impedance spectroscopy (EIS)	86
6.4.3.3.	Cyclic voltammetry (CV).....	88
6.4.3.4.	Small angle X-ray scattering (SAXS)	89
6.4.3.5.	Electrical transport measurements using Hg drop method.....	91
6.4.3.6.	Thermal gravimetric analysis (TGA)	91
6.5.	CONCLUSIONS.....	92
	CHAPTER 7 APPLICATION OF CARBON DERIVED FROM NCC IN DSSCS	93

7.1.	INTRODUCTION	93
7.2.	CHARACTERIZATION OF NCC FILMS AND DSSCs.....	93
7.2.1.	<i>Appearance of drop-cast NCC films</i>	93
7.2.2.	<i>Atomic force microscopy (AFM)</i>	94
7.2.3.	<i>Thermogravimetric analysis (TGA)</i>	95
7.2.4.	<i>DSSC fabrication using drop-cast NCC films</i>	96
7.2.5.	<i>Current density-voltage (J-V) analysis</i>	97
7.2.6.	<i>Electrochemical impedance spectroscopy (EIS)</i>	100
7.3.	PREPARATION OF NCC FILMS BY SPIN COATING	100
7.3.1.	<i>Current density-voltage (J-V) analysis</i>	101
7.4.	CONCLUSIONS.....	102
	CHAPTER 8 PRECIOUS METAL-FREE ORGANIC DYES.....	103
8.1.	BACKGROUND.....	103
8.2.	SYNTHESIS OF ORGANIC DYE SENSITIZERS AND THEIR CHARACTERIZATION.....	104
8.2.1.	<i>Oligothiophene dyes</i>	104
8.2.2.	<i>Cyanoviny l carboxylate and cyanoviny l phosphonate dyes</i>	108
8.3.	A NOTE ON DSSC FABRICATION.....	111
8.4.	DSSCs USING OLIGOTHIOPHENE PHOSOPHONATE AND CARBOXYLATE	112
8.5.	PERFORMANCE ANALYSIS OF DSSCs	115
8.6.	CONCLUSIONS.....	117
	CHAPTER 9 CONCLUSIONS AND FUTURE WORK.....	118
9.1.	THESIS SUMMARY	118
9.2.	FUTURE RESEARCH DIRECTIONS.....	119
	BIBLIOGRAPHY	121
	APPENDIX.....	150
	LICENSE PERMISSION 1.....	150
	LICENSE PERMISSION 2.....	150

LIST OF TABLES

Table 5-1: Metrics extracted from J-V curves of DSSC with TiCl ₄ treatment.....	68
Table 5-2: Efficiencies of DSSCs with stacks of two, four CNT films and thick paper counter electrodes.	72
Table 6-1: Comparison of DSSCs with VACNTs CE already available in literature.	74
Table 6-2: Metrics extracted from DSSC with CNT CE grown with MeOH-CVD under various light intensities without TiCl ₄ treatment. *At 1 sun, the current densities have been scaled linearly to 1 sun (101.0 mW/cm ²) as the data were mistakenly collected at 88 mW/cm ² . Note that in this regime the photocurrent varies linearly with illumination.	82
Table 6-3: Metrics extracted from J-V curves of DSSCs with MW-VACNTs and Pt CEs under 1 sun illumination.....	86
Table 7-1: Metrics extracted from J-V curves of DSSC with drop-cast NCC derived carbon CE under various sun intensities.	98
Table 7-2: Metrics extracted from J-V curves of spin-coated NCC counter electrode DSSC.....	102
Table 8-1: Photophysical properties and comparative parameters for the oligothiophene dyes.	106
Table 8-2: Monolayer characterization parameters of 3TP-6TP dyes; a (SAMs prepared by T-BAG method); b (SAMs prepared by dipping in 0.1 mM in THF).	107
Table 8-3: Photophysical properties and comparative parameters for the cyanovinylyl carboxylate and cyanovinylyl phosphonate dye sensitizers. ^a Absorptions of charge-transfer transition were measured in THF. ^b Absorption spectra were measured in DMF.	110
Table 8-4: Monolayer characterization parameters of phosphonate and carboxylate dyes; ^a (SAMs prepared by T-BAG method); ^b SAMs prepared by dipping in 0.1 mM in THF; ^c SAMs prepared by dipping in 0.1 mM saturated dye solution (~2 mM in THF).	111
Table 8-5: DSSC performance metrics for oligothiophene and oligothiophene with phosphonate and carboxylate dyes at 1 sun. * TiO ₂ with TiCl ₄ treatment.	114

LIST OF FIGURES

Figure 1-1: World total primary energy consumption [EIA, http://www.eia.gov].	2
Figure 1-2: World renewable energy generating capacity [US energy information administration, AEO tables (2013)].	2
Figure 1-3: Classification of photovoltaic technologies.	3
Figure 1-4: Current record photovoltaic research-cell efficiencies.	4
Figure 1-5: Air Mass (AM) increases with the angle from the zenith.	9
Figure 1-6: $AM\ 1.5\ G$ reference spectrum.	10
Figure 2-1: A schematic structure of dye-sensitized solar cell (not to scale).	16
Figure 2-2: Schematic representation of the operating principle of DSSC (not to scale).	17
Figure 2-3: Recombination processes in DSSC (not to scale).	19
Figure 2-4: Charge transfer processes between a dye sensitizer molecule and the TiO_2 layer: (1) MLCT excitation; (2) Electron injection, and (3) Charge recombination.	20
Figure 2-5: Circuit of a typical photovoltaic cell.	26
Figure 2-6: Typical shape of the J-V curve of a photovoltaic cell.	27
Figure 3-1: Unrolled graphite sheet to construct CNT with chiral vector C_h and a_1 and a_2 are unit vectors. T is the translational vector of nanotube and ' θ ' is the chiral angle.	29
Figure 3-2: Schematic diagram of an arc-discharge system.	30
Figure 3-3: Schematic diagram of a laser ablation system.	31
Figure 3-4: Schematic diagram of a chemical vapour deposition system.	31
Figure 3-5: Schematic representation of CNT growth mechanism. Tip-growth (upper figure) and base-growth (lower figure).	34
Figure 4-1: Structure of N3 dye molecule.	38
Figure 4-2 (a-d): Various modifications in cell design.	39
Figure 4-3: DSSC assembling (cross-sectional view, not to scale).	40
Figure 4-4: Photoanode with blocking layer.	41
Figure 4-5: Schematic diagram of the WA-CVD apparatus setup for CNTs growth.	43
Figure 4-6: Chemical structure of Nanocel.	49

Figure 4-7: Typical equivalent circuit to model electrolyte/counter electrode interface and series resistance of an electrochemical cell.....	52
Figure 4-8: Nyquist plot for equivalent circuit to model electrolyte/counter electrode interface with charge transfer resistance, R_{CT} , in parallel with a capacitor (solid line) and CPE (dashed line) and series resistance, R_S	52
Figure 4-9: A typical cyclic voltammogram for reversible system.	54
Figure 4-10: A schematic setup of a SAXS experiment.	56
Figure 4-11: Working principle of XPS.....	58
Figure 4-12: (a) Schematic diagram of setup and (b) built setup.	59
Figure 4-13: Working principle of AFM.	61
Figure 5-1: J-V of the first DSSC fabricated with only a screen printed TiO_2 photoanode and a Pt-based counter electrode at 1 sun. Inset: dark J-V.....	62
Figure 5-2: J-V of the second DSSC with improved sealing and filling at 1 sun. Inset: dark J-V.....	63
Figure 5-3: J-V of DSSC with spin-coated and screen printed TiO_2 layers at 1 sun. Inset: dark J-V.....	64
Figure 5-4 : (a) Top view of screen printed TiO_2 on FTO, (b) Cross-sectional view of screen printed TiO_2 on FTO.....	65
Figure 5-5: (a) Top view of spin-coated TiO_2 on FTO, (b) Cross-sectional view of spin-coated TiO_2 on FTO.....	65
Figure 5-6: J-V curve of DSSC with fully illuminated area (0.04 cm^2) at 1 sun. Inset: dark J-V.....	66
Figure 5-7: J-V curve of DSSC with $TiCl_4$ treatment under dark.....	67
Figure 5-8: J-V curves of a 0.04 cm^2 DSSC with $TiCl_4$ treatment under various illumination intensities.....	67
Figure 5-9: J-V curve of a DSSC with a stack of two CNT films on FTO as a counter electrode at 1 sun. Inset: dark J-V.....	70
Figure 5-10: J-V curve of a DSSC with a stack of four CNT films on FTO as counter electrode at 1 sun. Inset: dark J-V.....	70
Figure 5-11: J-V curve for DSSC with thick CNT paper as a counter electrode at 1 sun. Inset: dark J-V.	71

Figure 6-1: SEM of VACNTs grown with CVD method with electron beam evaporation deposited (a, b) and sputtered (c, d) Fe samples.	75
Figure 6-2: SEM of CNTs grown at 580°C on a) Aluminum Alloy/Cr/Invar; b) Directly on SS; c) SS/Invar; d) Quartz/Cr/Invar.	76
Figure 6-3: SEM of (a) As-received FTO, post-exposure to: (b) WA growth conditions, (c) MeOH growth conditions, (d) NH ₃ -C ₂ H ₄ growth conditions.	77
Figure 6-4: The XPS – F 1s signal is completely absent following exposure to growth conditions (left), indicating a loss of the dopant from the conducting oxide. The appearance of the Si 2p peak following exposure indicates de-wetting of the SnO _x revealing the glass substrate beneath the FTO (right), consistent with interpretation of the SEM results.	79
Figure 6-5: UV-vis spectra of as-received and post-exposure FTO.	80
Figure 6-6: DSSC with CNT CE grown with the MeOH-CVD in the dark without TiCl ₄ treatment.	81
Figure 6-7: DSSC with CNT CE grown with the MeOH-CVD under various light intensities, without TiCl ₄ treatment.	81
Figure 6-8: Growth of MW-VACNTs (exposure time versus CNT length). Each data point represents the average of 5 samples.	83
Figure 6-9: Growth of MW-VACNTs on SS with different exposure times a) 10 s b) 20 s c) 40 s and d) 60 s.	84
Figure 6-10: Dark J-V curves of DSSCs with MW-VACNTs counter electrodes.	85
Figure 6-11: J-V curves of DSSCs with MW-VACNTs and Pt CEs under 1 sun.	85
Figure 6-12: Electrochemical impedance spectroscopy of Pt-Pt and MW-VACNT-Pt. cells in dark (measured data).	87
Figure 6-13: Equivalent circuit used to fit EIS plots for MW-VACNT-Pt cells.	87
Figure 6-14: An enlargement of the high frequency side of the above EIS spectra.	88
Figure 6-15: R _{CT} and capacitance of MW-VACNT/electrolyte interface –Pt as a function of CNT length from EIS of two terminal electrochemical cells characterized in the dark.	88
Figure 6-16: Cyclic voltammograms of MW-VACNT-Pt cells with varying CNT lengths in the dark.	89

Figure 6-17: SAXS of MW-VACNTs with different lengths grown on Cu foil (5 μm). .	90
Figure 6-18: Effect of MW-VACNTs length on radius extracted from SAXS data.	91
Figure 6-19: TGA and DTG plots of MW-VACNTs grown with WA-CVD.....	92
Figure 7-1: a) Drop-cast NCC film on FTO before pyrolysis, b) Drop-cast NCC film on FTO after pyrolysis.....	94
Figure 7-2: a) NCC film as-cast on FTO, b) Pyrolyzed NCC film on FTO.	95
Figure 7-3: TGA and DTG of 1 hr pyrolyzed NCC.....	96
Figure 7-4: TGA of NCC pyrolyzed for 1, 4 and 8 hrs.....	96
Figure 7-5: Dark J-V curve of DSSC with drop-cast NCC derived carbon CE.	97
Figure 7-6: J-V curves of DSSC with drop-cast NCC derived carbon CE under various sun intensities.	98
Figure 7-7: Cell metrics of DSSC with drop-cast NCC-derived carbon CE under various illumination intensities.	99
Figure 7-8: Open-circuit voltage of DSSC with drop-cast NCC derived carbon CE under various sun intensities. Inset: short-circuit current density as a function of illumination intensity.	99
Figure 7-9: Nyquist plot of FTO\NCC two terminal symmetric cell of drop-cast pyrolyzed NCC film electrodes.	100
Figure 7-10: Dark J-V curve of spin-coated NCC counter electrode DSSC.	101
Figure 7-11: J-V curves of spin-coated NCC counter electrode DSSC under various sun intensities.....	102
Figure 8-1: The structure of oligothiophene phosphonates dye sensitizers.....	105
Figure 8-2: Absorption spectra of 3TP-6TP in THF.....	105
Figure 8-3: AFM images of TiO_2 (2 nm)/ SiO_2 /Si: (a) 5 μm x 5 μm (rms roughness: 0.28 nm); (b) 1 μm x 1 μm (rms roughness: 0.37 nm).	107
Figure 8-4: AFM images of 4TP (1.5 nm)/ TiO_2 / SiO_2 /Si: (a) 5 μm x 5 μm (rms roughness: 0.24 nm); (b) 1 μm x 1 μm (rms roughness: 0.38 nm).	107
Figure 8-5: The structure of cyanovinyl carboxylate and cyanovinyl phosphonate dyes.	108
Figure 8-6: Absorption spectra in THF of cyanovinyl phosphonate species (3TCP, 4TCP) with cyanovinyl carboxylate species (3TCC, 4TCC).....	109

Figure 8-7: Absorption spectra in THF of cyanovinyl-substituted oligothiophene phosphonate (3TCP, 4TCP) with their unsubstituted phosphonate congeners (3TP, 4TP).....	109
Figure 8-8: AFM images of (a) 4TCP (2 nm)/TiO ₂ /SiO ₂ /Si (rms roughness: 0.37 nm) and (b) 4TCC (2.0 nm)/TiO ₂ /SiO ₂ /Si (rms roughness: 0.42 nm). Scan area is 5 μm x 5 μm.....	111
Figure 8-9: J-V curves for 3TP-6TP DSSCs at 1 sun.	112
Figure 8-10: J-V curves for 3TP, 3TCC and 3TCP DSSCs at 1 sun.	113
Figure 8-11: J-V curves for 4TP, 4TCC and 4TCP DSSCs at 1 sun.	114
Figure 8-12: Comparative DSSC device performance of (oligothiophene) phosphonate, (cyanovinyl) phosphonate, and (cyanovinyl) carboxylate dyes. *TiO ₂ first treated with TiCl ₄	115
Figure 8-13: Plot of V _{OC} as a function of ln of J _{SC} for nTP DSSCs.	116

ABSTRACT

Exploring new technologies that can meet the world's energy demands in an efficient and clean manner is critically important due to the depletion of natural resources and environmental concerns. Dye-sensitized solar cells (DSSCs) are low-cost and clean technology options that use solar energy efficiently and are being intensively studied. How to further reduce the cost of this technology while enhancing device performance is one of the demanding issues for large scale application and commercialization of DSSCs. In this research dissertation, four main contributions are made in this regard with the motivation to reduce further cost of DSSC technology. Firstly, ~10% efficiencies were achieved after developing understanding of key concepts and procedures involved in DSSCs fabrication. These efficiencies were achieved after step-by-step modifications in the DSSC design. Secondly, carbon nanotubes (CNTs) were successfully employed as an alternative to Pt in the counter electrodes of DSSCs. DSSCs fabricated with CNTs were ~86% as efficient as Pt-based cells. Non-aligned CNTs were successfully grown using four different CVD methods and finally, multi-walled vertically aligned CNTs (MW-VACNTs) were synthesized using water-assisted chemical vapor deposition (WA-CVD). Thirdly, carbon derived from pyrolysis of nanocrystalline cellulose (NCC) was successfully employed in counter electrodes of DSSCs instead of Pt. DSSCs with NCC were ~58% as efficient as Pt-based DSSCs. Fourthly, novel organic metal-free dyes were designed and employed instead of commonly used Ru-based dyes. DSSCs with these novel sensitizers were ~62% as efficient as those using the conventional Ru-based dyes. Characterization techniques including current-voltage measurements, scanning electron microscopy (SEM), electrochemical impedance spectroscopy (EIS), cyclic voltammetry (CV), thermogravimetric analysis (TGA), small angle x-ray scattering (SAXS), atomic force microscopy (AFM) and x-ray photoelectron spectroscopy (XPS) were used.

LIST OF ABBREVIATIONS AND SYMBOLS USED

$\mu\text{c-Si}$	Micro-crystalline silicon
AFM	Atomic force microscopy
<i>AMI.5G</i>	Air mass 1.5G
Ar	Argon
a-Si	Amorphous silicon
BTU	British thermal unit
C_2H_4	Ethylene
CB	Conduction Band
CdTe	Cadmium telluride
CE	Counter Electrode
C_h	Chiral vector
CIGS	Copper-indium-gallium-selenide
CIS	Copper-indium-selenide
CNTs	Carbon nanotubes
CO	Carbon monoxide
Co	Cobalt
CO_2	Carbon dioxide
COOH	Carboxylate group
CPE	Constant phase element
CPV	Concentrating PV
c-Si	Crystalline silicon
CV	Cyclic voltammetry
CVD	Chemical vapour deposition
DFT	Density functional theory
DI	de-ionized water
DMF	Dimethylformamide
DSSC	Dye-sensitized Solar Cell
ϵ	Extinction coefficient
EIA	US energy information administration

EIS	Electrochemical impedance spectroscopy
eV	Electron volt
Fe	Iron
FF	Fill factor
fs	femtosecond
FTO	Fluorine-doped tin oxide
GT	Gigatons
GW	Giga watt
H ₂	Hydrogen gas
HOMO	Highest Occupied Molecular Orbital
I ₃ ⁻ /I ⁻	Triiodide/Iodide
ID	Internal diameter
ITO	Indium-tin oxide
J _{sc}	Short-circuit current density
LUMO	Lowest Unoccupied Molecular Orbital
mc-Si	Multi-crystalline silicon
MeOH	Methanol
MLCT	Metal-to-ligand charge transfer
ms	millisecond
MW	Megawatt
MWCNTs	Multi-walled CNTs
NCC	Nanocrystalline Cellulose
NH ₃	Ammonia
Ni	Nickel
ns	nanosecond
O ₂	Oxygen gas
O.D.	Outside diameter
OSC	Organic solar cells
Pt	Platinum
PV	Photovoltaic
QCM	Quartz crystal microgravimetry

R _{CT}	Charge transfer resistance
Red/Ox	Reduction /Oxidation
RMS	Root mean square
rpm	Revolution per minute
RTP	Rapid thermal process
SAM	Self-assembled monolayer
SAXS	Small angle X-ray scattering
scm	Standard cubic centimeters per minute
SEM	Scanning electron microscopy
Si	Silicon
Si/SiO ₂	Silicon/silicon oxide
SWCNTs	Single-walled CNTs
T-BAG	Tethering by aggregation and growth
TCC	Thiophene with cyanovinyl carboxylate
TCO	Transparent Conducting Oxide
TCP	Thiophene with cyanovinyl phosphonate
TGA	Thermal Gravimetric Analysis
THF	Tetrahydrofuran
TiCl ₄	Titanium tetrachloride
TiO ₂	Titanium dioxide
TP	Thiophene
TW	Terawatt
USD	United States Dollar
UV-vis	Ultraviolet-visible
Voc	Open circuit voltage
WA-CVD	Water-assisted CVD
WE	Working Electrode
XPS	X-ray Photoelectron Spectroscopy
XRD	X-ray Diffraction
η	Solar cell efficiency

ACKNOWLEDGEMENTS

All gratitude is to ALLAH almighty who guided and aided me to bring-forth light this thesis and all respect and reverence for Holy Prophet Muhammad (P.B.U.H) whose teachings are complete guidance for human beings.

I am highly obliged to Prof. Dr. Ian G. Hill, my supervisor, for his best cooperation, positive criticism, constant encouragement, valuable suggestions, fair comments and clarity of thinking in guiding this work. Under his dynamic, able and inspiring supervision the present study was carried out. I am gratefully thankful for his patronage, scholastic guidance and providing the necessary facilities throughout this work.

My ineffable indebtedness is also due to my supervisory committee members, Dr. Ted Monchesky and Dr. Kevin Hewitt, for their keen interest, valuable guidance and marvelous suggestions during the span of this entire study.

Special thanks to Dr. Jeff Dahn and Dr. Laurent Kreplak for permitting the use of their facilities and the support from their research assistants and students. Also to the technicians and support staffs at physics department, especially Andrew E. Geroge.

I also thank all my group members, especially Dr. Douglas Staple, Mathew McDowell, Dr. Ahmad Ismail, Dr. Mingqing Wang, Yousaf Alattar and Jon-Paul Sun for their encouragement and time during my stay here.

I would also thank University of Agriculture, Faisalabad, Pakistan for financial support under the faculty development program (FDP) and higher education commission (HEC) of Pakistan.

Last but surely not least, my special thanks are reserved for my parents and family members, who have given me encouragement and love for whatever I have got so far in my life. I also thank them all for their prayers for successful achievements.

CHAPTER 1 INTRODUCTION

World energy consumption is increasing rapidly, see Figure 1-1, and this energy demand seems to be a major challenge to humanity in the future. In order to maintain economic growth, it is necessary to find a new horizon of energy sources to tackle this energy issue. Within this context, several alternative energy sources such as solar energy, wind energy have attracted the attention of both industry and academia.¹

Solar energy is one of the most promising future carbon-free energy resources as the sun is the most abundant energy source available. Almost all energy sources including wind, fossil fuel, hydro and biomass have their origins in sunlight. The direct conversion of sunlight into electric power by photovoltaic (PV) cells is of particular interest. In PV power generation, electricity is produced without the exhaust of greenhouse gases and without nuclear waste byproducts.² Simultaneously, both reserve depletion and greenhouse gas emissions require a major shift from fossil fuels as the dominant energy source.³

Today, global primary energy consumption is about 16 TW and is predicted to rise to 25-30 TW in 2050.⁴ A total of $\sim 1.73 \times 10^{17}$ W of solar radiation reaches the surface of earth.⁵ The theoretical solar power reaching the earth at any given time is estimated to be 1.2×10^5 TW and practical potential is estimated to be ~ 600 TW.⁶ Even if a fraction of this solar energy can be harvested, it is enough to satisfy world's energy demand.

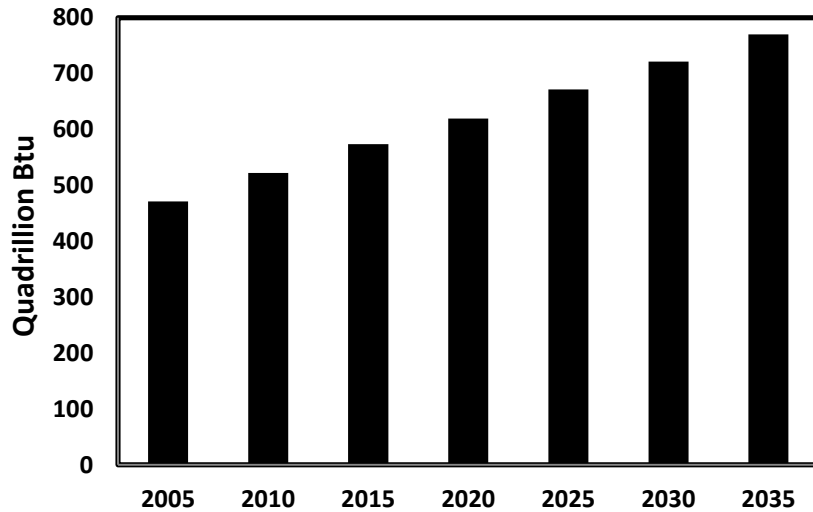


Figure 1-1: World total primary energy consumption [EIA, <http://www.eia.gov>].

Although the use of PV cells is relatively small (~15 GW), it has a particularly promising future, as progressive energy policies are being implemented in many countries to accelerate its deployment. Global PV capacity has been increasing rapidly, at an average annual growth rate of ~40% since 2000, and it has significant potential for long-term growth over the next decades, see Figure 1-2.

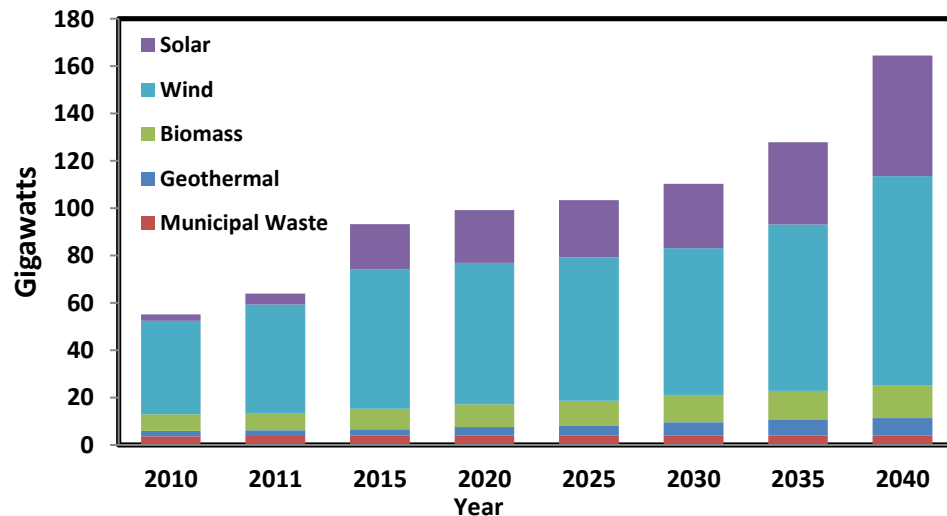


Figure 1-2: World renewable energy generating capacity [US energy information administration, AEO tables (2013)].

It is estimated that PV cells will provide ~11% of global electricity production by 2050, avoiding 2.3 gigatons (GT) of CO₂ emission.⁷ This growth is a result of a combination of recent developments in this field including decrease in prices, increase in investments and the use of low-cost novel thin film technologies.

1.1. PHOTOVOLTAIC TECHNOLOGIES

Photovoltaic technologies can be divided into three generations as shown in Figure 1-3. Current record photovoltaic cell efficiencies are shown in Figure 1-4.

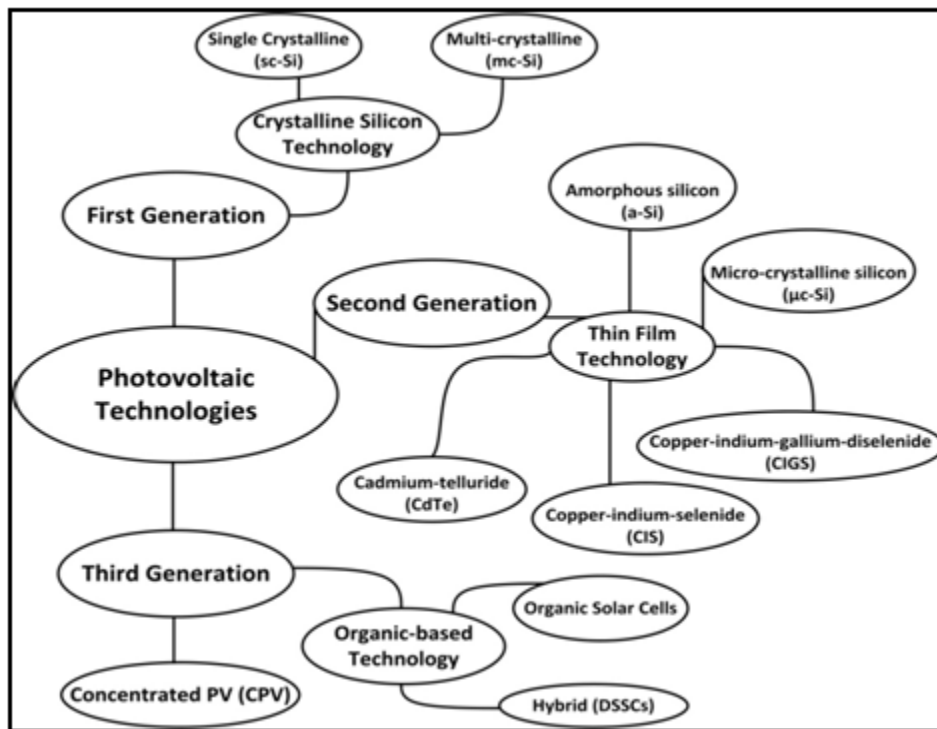


Figure 1-3: Classification of photovoltaic technologies.

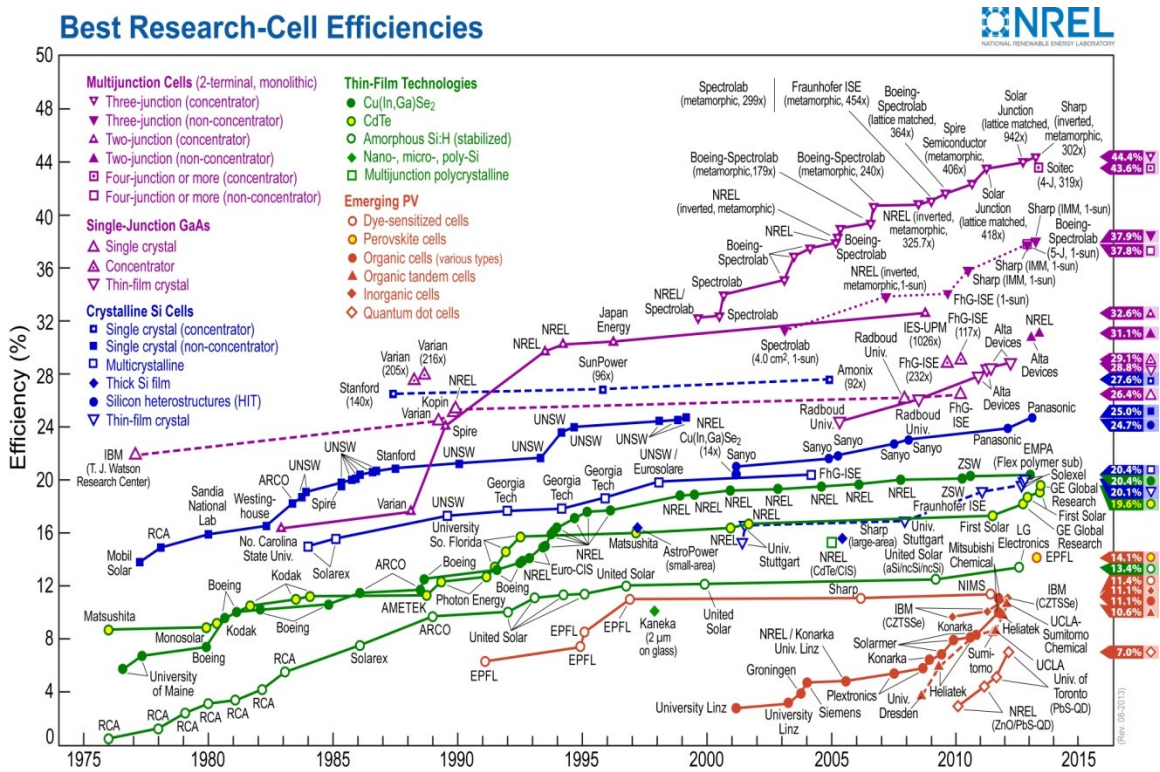


Figure 1-4: Current record photovoltaic research-cell efficiencies.⁸

1.1.1. First generation solar cells

The first solar cell made with silicon (Si) was demonstrated at Bells labs in 1954⁹, providing the foundation of the first generation solar cells. Silicon, a semiconductor material, is available abundantly in the earth's crust. Its energy band gap (1.1 eV) has made it suitable for PV applications. Today, this technology is mature and wafer based crystalline silicon c-Si PV cells and modules dominate the current market accounting for almost 90% of it.¹⁰ These cells and their modules are being produced on a massive scale and are able to produce at the rate of several hundred MW a year, or even at the GW-scale. Crystalline silicon cells can be classified into these main categories, namely:

1. Monocrystalline (Mono c-Si) / single crystalline (sc-Si);
2. Polycrystalline (Poly c-Si) / multi-crystalline (mc-Si);

The theoretical limit (Shockley-Queisser limit) for these cells is ~33%.¹¹ The efficiency of commercially produced modules ranges from 14% to 20%.¹² This is still far away from

the theoretical maximum efficiency value. Si-based PV is relatively expensive due to the high cost of purifying, crystallizing and sawing c-Si. It is also slow to grow Si crystals, requiring thick Si wafers to absorb sunlight. It is strongly believed that these drawbacks can be avoided by reducing the Si quantity in these cells using novel techniques such as thin film solar cells.

1.1.2. Second generation solar cells

Thin film second generation technologies appeared in 1970.¹³ It took almost 20 years of research and development to start deployment of this technology in significant quantities. Second generation PV could provide relatively low-cost electricity as compared to c-Si based technology. Besides its low-cost, second generation PV requires less material and can be packed into flexible and lightweight structures that can easily be integrated into building components. All these factors make second generation PV more attractive than first generation technology. The three primary types of thin-film solar cells that have been commercially developed are:

1. Amorphous silicon (a-Si and a-Si/ μ c-Si);
2. Cadmium telluride (CdTe);
3. Copper-indium-selenide (CIS) and Copper-indium-gallium-diselenide (CIGS)

1.1.2.1. a-Si/ μ c-Si solar cells

Although a-Si has lower efficiency as compared to other thin film solar cells, it was commercialized much earlier. a-Si-based cells have efficiency of $9.5\% \pm 0.3\%$ (1.07 cm^2).¹⁴ The main disadvantage of a-Si solar cells is related to their poor stability under sun exposure.

A variant of a-Si solar cells are multi-junction cells consisting of a-Si cells with layer of μ c-Si such as Kaneka's 11.7% micromorph a-Si/ μ c-Si heterostructures.¹⁵ Although μ c-Si showed good stability under 1 sun illumination¹⁶, the mechanisms related to light-induced degradation are still not well understood.

1.1.2.2. CdTe solar cells

Cadmium telluride (CdTe) thin film PV solar cells are economical, having ~18% efficiency with manufacturing costs under USD 0.75/W.¹⁷ There are some environmental concerns about the toxicity of cadmium and long term availability of tellurium as it is produced as a byproduct of copper processing. However, the small amount of Cd used in thin film solar cells can be recycled at the end of the lifetime of modules in order to isolate them from the environment.

1.1.2.3. CI(G)S solar cells

CI(G)S-based PV cells are a promising type of thin film solar cells. These cells have achieved a record efficiency of 20.3% at the lab level, which is close to the c-Si based solar cells.¹⁸ However, significant cost advantages have not yet been achieved on such modules. Therefore, there is a race to increase efficiency for commercially available modules. Improvements can be achieved by improving the understanding related to thin film processing, and development of new technology to solve equipment and scale-up issues.

1.1.3. Third generation solar cells

Third-generation PV technologies comprise novel concepts that do not fall under previously discussed technologies. Some third-generation PV technologies are beginning to be commercialized, but are still in need of basic research and development. These can be classified into three types:

1. Concentrating PV (CPV);
2. Organic solar cells;
3. Dye-sensitized solar cells (DSSC).

1.1.3.1. Concentrating PV (CPV)

In concentrating PV (CPV) technology, sunlight is concentrated directly on small and highly efficient multi-junction solar cells using lenses or mirrors. These multi-junction solar cells are typically made of semiconductor compounds from groups III and V of the

periodic table. Concentrating sunlight increases the solar illumination power density. Therefore, higher concentration means greater generation of electricity. In order to generate electricity in an efficient manner, the lenses and the mirrors should be permanently oriented towards the sun, achieved using a single- or double-axis tracking systems. Drawing heat off the cells is also important and is achieved using heat sinks.

Silicon-based CPV modules that are commercially available offer efficiencies in the range of 20% to 25%. CPV based on multi-junction solar cells using III-V semiconductors have achieved laboratory efficiency of more than 40%.¹⁹

This technology has some disadvantages including high cost, inefficient operation in cloudy days, need of additional maintenance and management due to the tracking and cooling systems.

1.1.3.2. Organic solar cells (OSCs)

Organic solar cells are promising photovoltaic devices due to their flexibility, low-cost and simple manufacturing processes. They have potential applications in large area, printable and flexible solar panels. Organic solar cells are composed of organic or polymer materials. Their success in recent years has been due to many significant improvements that have led to higher efficiencies. This technology is still in its infancy; however, organic PV module efficiencies are now in the range 4% to 5% for commercial systems and 10.6% in the laboratory for a polymer tandem cell, and 12% efficiency for a commercial tandem cell.^{20,21}

There are mainly two structures of OSCs, namely the bilayer heterojunction and the bulk heterojunctions. Bilayer heterojunctions are analogous to p-n junction Si solar cells, while the bulk heterojunction is an attempt to maximize the p-n interface by intermixing donor and acceptor polymeric materials in a solution.

One of the major challenges that organic solar cells are facing is their instability when exposed to light.^{22, 23, 24, 25} The efficiency of solar cells degrades by 25-50% within a very

short period of exposure to light and/or environment. However, some recent results show that after the rapid decrease in efficiency (~ 25%), the cells appear to stabilize.²⁶

1.1.3.3. Dye-sensitized solar cells (DSSCs)

Dye-sensitized solar cells are photoelectrochemical solar cells that mimic photosynthesis.²⁷ These cells are attractive because they use low-cost materials (TiO₂, for instance) and are simple to manufacture. Laboratory efficiencies of around 12% have been achieved using modern dyes such as zinc porphyrin dye and electrolytes such as cobalt (II/III)-based redox.²⁸ However, commercial efficiencies are low, typically under 4%-5%. DSSCs having liquid electrolytes have some issues regarding stability under UV light. This can be overcome using solid-state electrolyte materials. Recently, 15% laboratory efficiency was achieved for solid-state DSSCs based on Pb-perovskites.²⁹

For a truly significant impact of photovoltaics in our future electricity-mix, we need efficient and low-cost solar cells fabricated using abundant non-toxic materials with simple manufacturing processes.

1.2. AIR MASS AND THE SOLAR SPECTRUM

The sun is a tremendous source of energy. Radiative energy at the surface of sun is reasonably constant^{30,31}, however, it is attenuated by reaching the earth's surface. About 70% of the solar radiation in space reaches the Earth's surface. Apart from the reflection of clouds, attenuation is due to absorption and scattering.³² The degree to which the atmosphere affects the sunlight reaching at the earth's surface is defined by the "air mass". Air mass (AM) is defined as the ratio of the path length at an angle θ from zenith to that at zenith, as shown in Figure 1-5, and can be estimated according to

$$AM = \frac{1}{\cos \theta} \quad (1-1)$$

where θ is the angle measured from the zenith.

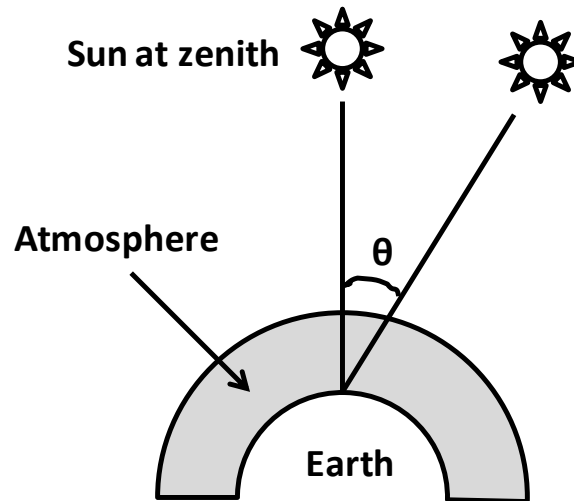


Figure 1-5: Air Mass (AM) increases with the angle from the zenith.

The spectrum outside the atmosphere is designated as $AM\ 0$ and is relevant to satellite and space-vehicle applications. The incident power density for $AM\ 0$ is $1353\ \text{W/m}^2$. The $AM\ 1$ spectrum represents the sunlight at the surface of earth when the sun is directly overhead and has an incident power of about $1040\ \text{W/m}^2$. When the sun is 48 degrees off zenith, the spectrum is called $AM\ 1.5$, see in Figure 1-6. $AM\ 1.5\ G$ corresponds to incident power of $1000\ \text{W/m}^2$ and is regarded as the standard spectrum for measuring the efficiency of solar cells on the surface of earth at mid altitudes. Here in $AM\ 1.5\ G$, G stands for global, and the global spectrum comprises the direct plus the diffuse sunlight.

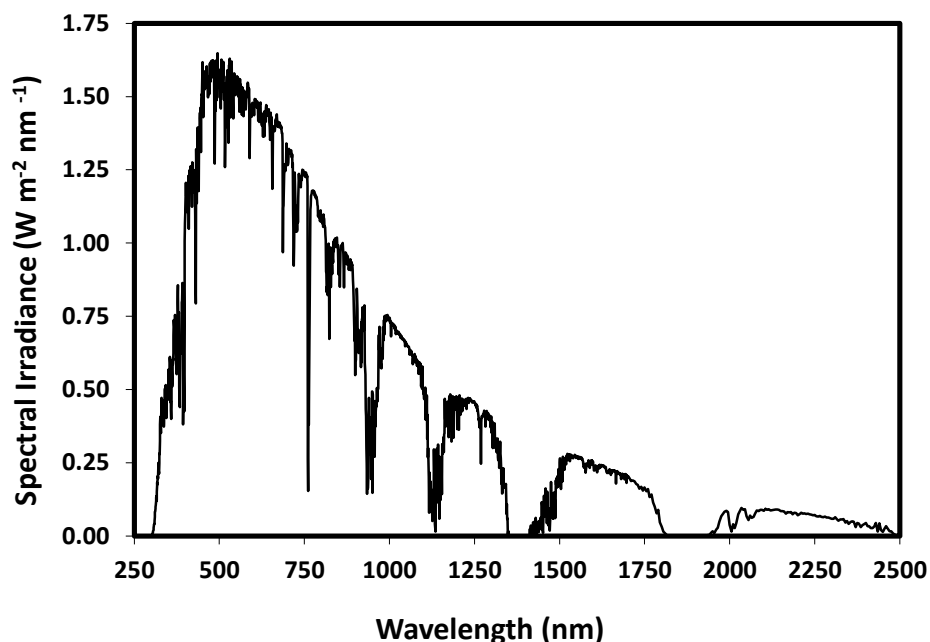


Figure 1-6: *AM 1.5 G* reference spectrum.³³

1.3. MOTIVATION

As discussed above, DSSCs technology is a promising alternative to silicon based solar cells as it has already superseded a-Si solar cells in terms of efficiency. Currently, the most efficient DSSC has ~15% efficiency with solid electrolyte. DSSCs have many advantages over Si based and thin film solar cells including simple and energy-efficient manufacturing, low-cost, non-toxic (compared to CdTe, for instance), and suitability for a wide variety of end-user products. DSSCs also work better than Si solar cells under low light intensities, and can thus be a good choice for indoor applications. For DSSCs to be competitive, they must be low-cost. Cost reductions can be realized if current materials including Pt and Ru can be replaced with lower-cost alternatives.

The counter electrode is one of the most critical components in DSSCs, which reduces triiodide (I_3^-) back to iodide (I^-) used as a redox charge mediator in regenerating the light absorbing sensitizer after electron injection.³⁴ In order to achieve higher electrocatalytic activity, the I^-/I_3^- redox reaction rate on the cathode should be fast. In other words, electrocatalytic activity in I^-/I_3^- redox reaction should be high.

Several studies have shown that platinum is an excellent candidate for use as catalyst in the counter electrode. However, its high cost and limited availability are not compatible with a low cost technology. In a quick calculation, trying to produce the entire world's electricity using this technology would require far more platinum than is present on earth. Also, platinum is found to degrade over time while in contact with the corrosive electrolyte.³⁵ Therefore, efforts are needed to search for a material that can replace platinum.

Another vital component in DSSCs is the photoanode, which accepts electrons injected from the photoexcited dye sensitizers. The dye sensitizers play a key role in DSSCs. To date, the best conversion efficiencies have been achieved using Ru-based complexes as sensitizers³⁶ in liquid-based electrolyte DSSCs. Ruthenium is a rare and potentially toxic heavy metal; ruthenium (Ru) complexes are expensive. Studies have shown that there is not enough Ru present in the world for this technology to meet our energy needs. Consequently, after the transparent conducting oxide (TCO) substrates, the ruthenium sensitizer is the second most expensive component in DSSC manufacture.³⁷ There is therefore a need to develop new precious metal-free dye sensitizers that can replace the traditional ruthenium sensitizers.

The objectives of the present research are to identify and optimize candidate materials for DSSCs which are readily available, cost-effective, sustainable, and capable of showing comparable performance to platinum and ruthenium based DSSCs.

Researchers are working with various approaches and materials in order to replace platinum in DSSCs, such as CoS,^{38,39,40,41} and composites of different conducting polymers.^{42,43,44} There is also a great deal of research that has been done on carbonaceous materials such as graphite^{45,46}, carbon black⁴⁷, activated carbon^{48,49}, hard carbon spheres⁵⁰, carbon nanotubes^{51,52,53}, fullerene⁵⁴ and graphene.^{55,56} A summary of DSSCs using these materials is given in Table 1-1. These materials are very attractive to replace platinum because of their low cost, high electrical conductivity, corrosion resistance to I₂

and high electrocatalytic activity for triiodide.^{57,58,59} Among all these, carbon nanotubes (CNTs) have recently attracted attention because of their catalytic properties, high surface area, and high electrical conductivity and may therefore be a potential candidate as a redox catalyst.^{35,60,140} CNTs may improve mechanical and environmental stability while enhancing conversion efficiency.

Carbonaceous Materials		Dye	Electrolyte	V _{oc} (V)	J _{sc} (mA/cm ²)	FF (%)	η (%)	Ref
Graphite	Sheet	N719	T ₂ /T ⁻	0.634	12.9	59	4.8	45
	Sheet	N719	I ⁻ /I ₃ ⁻	0.717	6.2	53	2.3	45
	Paste	N719	I ⁻ /I ₃ ⁻	0.794	12.7	62	6.2	46
Carbon black	Paste	N719	I ⁻ /I ₃ ⁻	0.790	16.8	68	9.1	47
Activated carbon	Paste	N719	I ⁻ /I ₃ ⁻	0.630	5.4	51	1.7	48
	Paste	N3	I ⁻ /I ₃ ⁻	0.808	7.9	61	3.9	49
Hard carbon spheres	Slurry	N3	I ⁻ /I ₃ ⁻	0.580	15.2	64	5.7	50
Fullerene	Film	N3	I ⁻ /I ₃ ⁻	0.410	2.1	19	0.2	54
Graphene	GNP film	Y123	Co (II/III)	0.878	14.8	72	9.4	55
		D35	T ₂ /T ⁻	0.663	9.5	55	3.5	56
		D35	Co (II/III)	0.813	8.5	65	4.5	56
Carbon nanotubes	MWCN T Paste	N719	I ⁻ /I ₃ ⁻	0.737	13.4	69	6.8	56
		N719	I ⁻ /I ₃ ⁻	0.740	16.20	64	7.7	51
		N719	I ⁻ /I ₃ ⁻	0.588	10.9	65	4.2	52
		N719	T ₂ /T ⁻	0.610	14.25	67	5.8	53

Table 1-1: DSSCs with various counter electrode carbonaceous materials.

In terms of dyes, organic dyes have attracted researchers in recent years. This is because of their variety of molecular structures, high molar extinction coefficients, low-cost and simple and environmentally friendly preparation processes. In the last decade, many

investigations on π -conjugated molecules with donor–acceptor moieties, such as indoline⁶¹, triphenylamine⁶² and coumarin⁶³, have been conducted. Oligothiophenes and their derivatives are also π -conjugated systems and have attracted the interest of the scientific community as new series of metal-free dyes in DSSCs.⁶⁴

1.4. A NOTE ON THE SUSTAINABILITY OF PT AND RU

1.4.1. Calculations for Pt

Let us consider a solar cell module (efficiency = 10%) that has 10 nm of Pt on its counter electrode and is illuminated under average useful solar irradiance of 200 W/m². In order to meet the average global energy consumption (1.6x10¹³ W), this would require a total 170 kt Pt as shown below:

$$1.6 \times 10^{13} W \times \frac{1m^2}{200W \times 10\%} \times 10^{-8}m \times \frac{21.45 \times 10^3 kg}{m^3} \cong 170 \text{ kt of Pt}$$

Annual production of platinum is 180 t whereas known reserves of platinum are 30 kt.

Platinum cost (dollar per peak-watt) can be calculated as given below:

Pt price on October 20, 2013 is USD 1400 per troy ounce (\$ 45000/kg) and this gives

$$\frac{1m^2}{200W \times 10\%} \times 10^{-8}m \times \frac{21.45 \times 10^3 kg}{m^3} \times \frac{\$45000}{kg} \cong \frac{0.50\$}{W}$$

1.4.2. Calculations for Ru

Similarly, for the same module having 2x10⁻⁷ mol/cm² dye loading⁶⁵, the amount of Ru required to meet the average global energy consumption (1.6x10¹³ W) can be calculated as shown below.

$$1.6 \times 10^{13} W \times \frac{1m^2}{200W \times 10\%} \times 2 \times 10^{-7} \frac{mol}{cm^2} \times \frac{10^4 cm^2}{m^2} \times \frac{101g}{mol} \times \frac{1kg}{1000g} \\ \cong 160 \text{ kt of Ru}$$

Annual production of Ru is 15 t whereas known reserves are 5 kt.

Ruthenium cost (dollar per peak-watt) can be calculated as given below:

Ru price on October 20, 2013 is USD 57 per troy ounce (\$ 1900/kg) and this gives

$$\frac{1m^2}{200W \times 10\%} \times 2 \times 10^{-7} \frac{mol}{cm^2} \times \frac{10^4 cm^2}{m^2} \times \frac{101g}{mol} \times \frac{1kg}{1000g} \times \frac{\$1900}{kg} \cong \frac{0.02\$}{W}$$

These calculations have shown that the main challenge is the sustainability of Pt and Ru.

CHAPTER 2 STRUCTURE AND WORKING

PRINCIPLES OF DSSCs

In this chapter, the technology of the dye-sensitized solar cell (DSSC) is introduced starting with a short description of the operating principles of the cell. After this, a more detailed look is taken at cell operation in light of the key steps of photovoltaic conversion, as well as the other important fundamental operational aspects of the cell physics and chemistry. At the end of this chapter, important parameters that determine the performance of DSSCs are also discussed.

2.1. STRUCTURE OF DYE-SENSITIZED SOLAR CELL (DSSC)

A DSSC generally contains four main elements: a photoanode, a dye-sensitizer, a hole transport electrolyte and a counter electrode. The photoanode is a thin nanoporous layer of annealed TiO_2 supported on transparent conducting oxide (TCO) glass. Dye molecules such as ruthenium bipyridine derivatives, which are sensitive to the visible light region in the solar spectrum, are attached chemically onto the semiconductor electrode. The counter electrode consists of a TCO coated with a catalyst layer, typically platinum. There is electrolyte typically containing the I^-/I_3^- redox couple in between these two electrodes. A schematic structure of DSSC is shown in Figure 2-1.

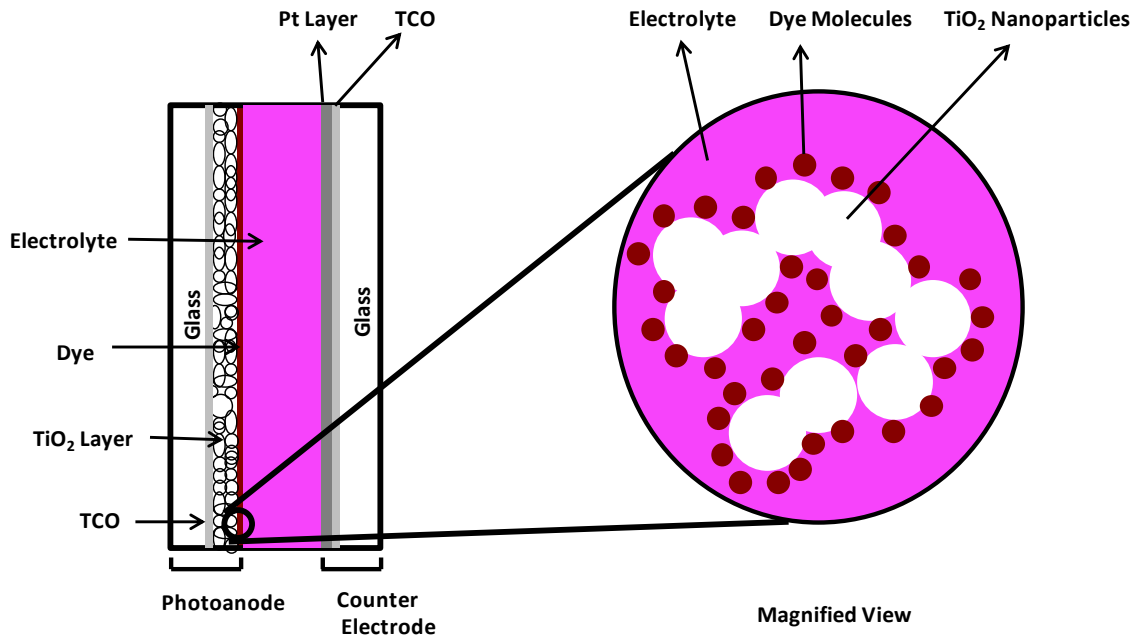


Figure 2-1: A schematic structure of dye-sensitized solar cell (not to scale).

2.2. OPERATING PRINCIPLE OF THE DYE-SENSITIZED SOLAR CELL

Figure 2-2 depicts schematically the regenerative working cycle of the dye-sensitized solar cell. Upon absorbing a photon, an electron is excited from the highest occupied molecular orbital (HOMO) level to the lowest unoccupied molecular orbital (LUMO) level of the dye molecules. This excitation leads to electron injection from the excited state of the dye molecules (S^*) into the conduction band (CB) of TiO_2 . Subsequently, the injected electrons percolate through the TiO_2 and are collected by the TCO. These electrons that pass through the external circuit come to the counter electrode and take part in the reduction of triiodide (I_3^-) to iodide (I^-) ions. The iodide ion in the electrolyte donates an electron to the oxidized dye molecules (S^+) which is reduced to the ground state (S^0).

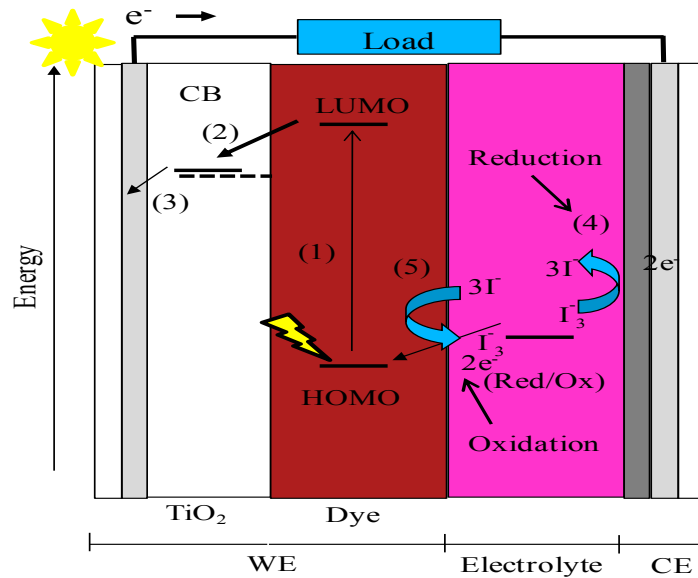
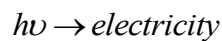


Figure 2-2: Schematic representation of the operating principle of DSSC (not to scale).

The operating cycle can be summarized as given below:



Overall cycle:



Due to the energy level positioning in the system (Figure 2-2), DSSC produces potential difference between its electrodes. Under open-circuit condition, the difference between the conduction band edge of the TiO₂ and the redox potential of the redox couple defines the maximum photovoltage that can be obtained from a DSSC.⁶⁶ This is the maximum potential energy difference through which the electron travels.

2.3. DSSC AND CONVENTIONAL P-N JUNCTION SOLAR CELL

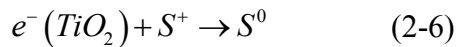
As the DSSC has a different structure and components than a conventional p-n junction solar cell, the operation of the DSSC is also different in many respects from the p-n junction solar cell that can be discussed as follows:

- In a conventional solar cell, light absorption and charge transport takes place in the same material, but in the DSSC these two functions typically happen separately, i.e., dye molecules absorb light and charge transport occurs in TiO₂ nanoporous film electrode and electrolyte.
- The depletion field across the junction is responsible for charge separation in a p-n junction cell whereas no such long-range electric fields exist in the DSSC as the individual particle size of TiO₂ is too small to form space charge layer and also any existing electric fields are screened out upon contact with electrolyte.
- In a conventional cell, the opposite charges produced travel in the same material, while in the DSSC, electrons percolate in the nonporous TiO₂ network and “holes” move in the electrolyte.

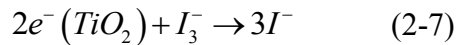
2.4. RECOMBINATION PROCESSES/LOSSES

Recombination processes decrease the efficiency of the DSSCs. The most probable and common losses are shown in Figure 2-3.

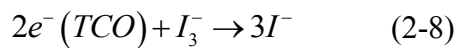
Recombination of electrons with oxidized dye molecules:



Recombination of electrons with the triiodide species in the electrolyte:



Recombination of electrons from bare TCO with the triiodide species in the electrolyte:



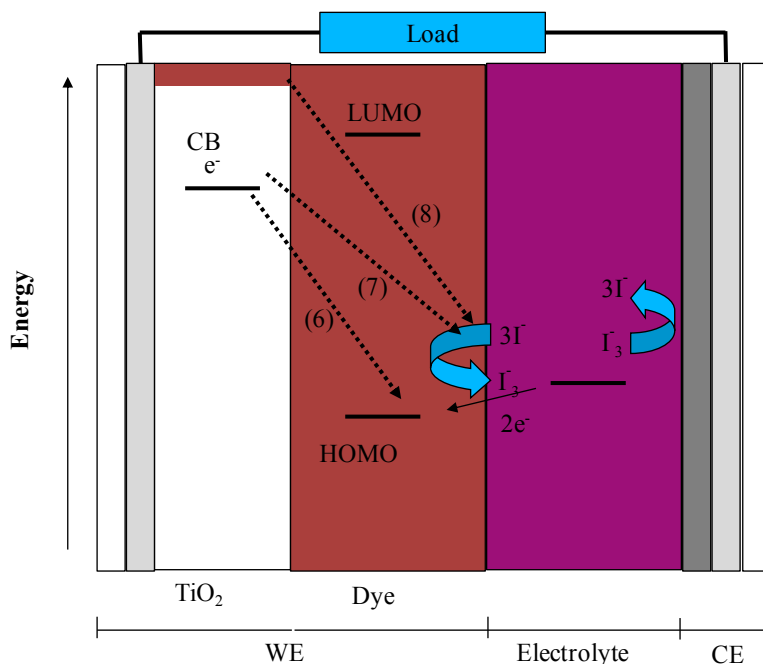


Figure 2-3: Recombination processes in DSSC (not to scale).

DSSC operation is discussed in more details in the following sections. This is discussed in terms of energetics and kinetics.

2.4.1. Reaction 1 (Absorption)

Dye molecules absorb photons due to an excitation between their electronic states, see Figure 2-4. This excitation is of metal-to-ligand charge transfer (MLCT) in nature. This promotes electrons from the HOMO level to the LUMO level of the molecular ground state.⁶⁷

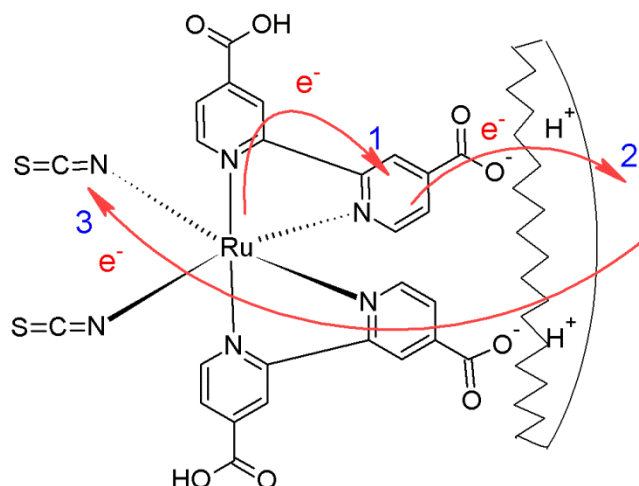


Figure 2-4: Charge transfer processes between a dye sensitizer molecule and the TiO_2 layer: (1) MLCT excitation; (2) Electron injection, and (3) Charge recombination.

The kinetic competition between electron injection and excited state decay of the dye molecule to its ground state has a strong correlation to the overall performance of DSSC. For an efficient DSSC, the rate of the the injection process should be much faster than that of the decay of the excited state of the dye to the ground state. This can be explained in terms of the excited state lifetime of the dye, which for typical Ru-complexes is 20-60 ns.⁶⁸

2.4.2. Reaction 2 (Electron injection)

One of the most amazing findings in DSSC is the ultrafast injection of the electron from the excited state of dye molecule to the TiO_2 conduction band (CB). Although the detailed mechanism of the injection process is yet not understood completely, there is a consensus in scientific community that this process takes place on the femtosecond time scale for the Ru-based complexes.^{69,70,71,72}

Mechanism of electron injection depends upon factors such as the electronic structure of the dye and the matching of excited dye molecule and the CB of the TiO_2 energy levels.⁷³ In comparison to silicon-based technology, the electrolyte in a DSSC has high concentration of charge carriers (ions) that adequately prevent the presence of any of

macroscopic electric fields. Therefore, charge separation solely takes place due to the intrinsic energetics of the different species at the TiO₂/dye/electrolyte interface. The excited state of the dye molecule must be more reducing than the TiO₂ conduction band in order to inject electrons efficiently, or in other words, the excited state of dye molecule (i.e., LUMO level) should have lower electron affinity relative to the conduction band edge of TiO₂⁷⁴, thus favoring electron injection to the TiO₂.

The positioning of energy levels between the dye molecule, conduction band edge of TiO₂ and the redox potential of the electrolyte is a primary mechanism for charge separation in DSSC. In order to separate electrons and holes, the LUMO level of the dye should be above the conduction band edge of the TiO₂ and its HOMO level should be below the redox potential of the redox pair iodide/triiodide in the electrolyte, as shown in Figure 2-2.

There is no macroscopic electric field inside the TiO₂ film, but there is an electric field at the TiO₂/electrolyte interface due to the adsorbed dye molecules. Typical dye molecules generally have carboxylic groups (COOH) and they release protons while binding to the oxide surface of TiO₂. These protons along with the cations in the electrolyte become part of the oxide surface. The potential difference across the Helmholtz layer formed between negatively charged species and the cations is estimated to be approximately 0.3 eV, and it helps to separate the charges as well as to reduce recombination.⁶⁶

Besides the favorable energetics for charge separation, there are also entropic factors at work. In the nanoporous TiO₂ film, the density of delocalized states is comparatively large to the small number of dye molecules on the TiO₂ surface. Under this condition, an increase in entropy occurs following electron injection. Therefore, the electron injection process can be associated with this entropy change. This change in entropy also facilitates the charge separation at the dye molecule/TiO₂ interface by providing a potential difference of ~0.1 eV.⁷⁵

The electron injection process competes with the decay of the excited state of the dye to its ground state. Thus, injection of electron to TiO₂ must be fast in comparison with dye

molecule decay. Typical time scales for dye molecule excitation decay are in the range 10^{-7} – 10^{-10} second. The rate of electron injection depends on a couple of factors such as the electronic coupling between the LUMO of the dye molecule and surface of the TiO_2 , and also on their relative energetics. Studies have shown that such charge separation occurs on a 10^{-15} – 10^{-12} second time scale.^{76,77}

2.4.3. Reaction 3 (Electron transport)

At the time of the discovery of DSSCs, maybe the most ambiguous concept was the highly efficient charge transport through the nanoporous TiO_2 layer. In contrast to their compact analogues, the nanoporous electrodes are very different due to (i) the TiO_2 film is inherently of very low conductivity, (ii) the individual colloidal particles are very small in size (~ 20 nm), so they prohibit a built-in depletion field, and (iii) a junction of large contact area is produced by the interpenetrating networks formed by the oxide nanoparticles and their pores that contain the electrolyte. Although the charge transport mechanisms in DSSC have been studied extensively, these are still under keen debate.^{78,79,80,81,82,83,84,85,86,87} To explain electron transport, various mechanisms and models have been proposed including a diffusion model^{78,79,80,81}, a model that deals with tunneling through potential barriers between the particles⁸², a trapping/detrapping model^{83,84,85,86}, and an insulator–metal transition model.⁸⁷

As already mentioned above, the small size of the TiO_2 particles prevents a built-in electric field inside the film, thus eliminating any considerable drift component of these processes. The transport of electrons occurs due to diffusion processes that arise from the electronic concentration gradient in nanoporous TiO_2 .^{88,89,90}

Studies have also shown that transport of electrons depends upon the incident light intensity.⁹¹ The diffusion coefficient of electrons depends on the electron quasi-Fermi level under illumination. These findings are explained using a multiple trapping (MT) model.^{92,93,94,95} In this model, these electron traps are localized energy states just below the conduction band edge of the TiO_2 and they play a significant role in the electron

transport. The origin, nature and location of these traps in TiO₂ are still a subject of discussion. The electron diffusion coefficient is also affected by the particle size of TiO₂.^{96, 97} As the particle size in the nanoporous layer of TiO₂ increases, the roughness factor of the layer is reduced, and this ultimately increases the diffusion length of electrons due to a reduction in the number of surface trap states.⁹⁸ (The roughness factor is the ratio of total actual surface area to the geometric area).

The geometry of the TiO₂ nanoporous layer also plays a very critical role in terms of electron transport through it.⁹⁹ The path of the electrons becomes excessively lengthy and complex in more porous films thus resulting in slow electron transport.

In DSSCs, charge collection depends upon the kinetic competition between the transport of injected electrons in the nanoporous semiconductor layer and the recombination reaction of these electrons with the redox species in electrolyte or with the oxidized dye molecules. In order to collect charge efficiently, electron transport must be much faster than recombination. Under solar irradiation, typical electron transport times are of the order of milliseconds.^{100,101}

2.4.4. Reaction 4 (Triiodide reduction)

In normal DSSCs, reduction of triiodide to iodide takes place at the counter electrode (reaction 4). For high performance DSSCs, the catalytic activity of the counter electrode must be high for this reaction in order to have low over-potential (energy loss). Platinum (Pt) is commonly used as a catalyst in counter electrodes because of its high catalytic activity for triiodide reduction. The charge transfer reaction at the CE gives rise to a resistance that is known as charge transfer resistance R_{CT} . This resistance at CE/electrolyte interface and the diffusion constants of triiodide are crucial parameters for highly efficient DSSCs.^{102,103,104} Ideally, R_{CT} should be $\leq 1 \Omega \text{ cm}^2$ to avoid important energy losses.¹⁰⁵ A bad counter electrode reduces the fill factor of the cell's current-voltage (I-V) characteristics, ultimately decreasing its overall efficiency.

Diffusion is the main transport mechanism of the redox couple between the electrodes of the DSSC. In order to minimize the effect of the electric field and transport by migration, electrolytes with high ionic conductivity should be used. For a viscous electrolyte, such as ionic liquids, diffusion coefficients can be too small to maintain the required flux of redox couple toward electrodes, thus affecting the photocurrent of the DSSC.¹⁰⁶

2.4.5. Reaction 5 (Regeneration of dye)

The electrolyte in the DSSC is commonly an organic solvent having the I^-/I_3^- redox couple that plays a crucial role in reactions (4) and (5). I_3^- is produced at the TiO_2 electrode, while I^- is produced at the counter electrode, but these are consumed at the corresponding opposite electrodes. In other words, the electrolyte feeds reactions (4) and (5) with redox couple at the electrodes while maintaining the redox potential in the bulk of the electrolyte. The reduction of the oxidized sensitizer (S^+) by iodide follows a multi-step reaction mechanism.¹⁰⁵

Electron transfer from I^- into the oxidized dye molecule is one of the main processes needed to achieve effective charge separation. The electron transfer rate was estimated to be 100 ns using time-resolved laser spectroscopy¹⁰⁷, which is much faster than that of charge recombination between injected electrons and oxidized dye molecules. Thus, this fast reaction also gives rise to effective charge separation.

2.4.6. Reactions 6, 7 and 8 (Recombination)

There is a possibility that electrons in the TiO_2 nanoporous film can recombine with either oxidized dye molecules or triiodide in the electrolyte as these electrons are always within a few nanometers distance of the semiconductor/electrolyte interface.

Reaction (6) is a very slow reaction as compared to electron injection in TiO_2 . Reaction (7), recombination of injected electrons in the TiO_2 with the triiodide ion at the interface, also known as dark current, is one of the undesirable processes in the DSSC. This process is much more probable than process (6).⁷⁴ Recombination (reaction 8) could also occur

on the transparent conducting oxide (TCO) as the TiO₂ film may not fully cover the TCO. However, studies have shown that this effect is small and negligible as platinum-free TCO has very poor electrocatalytic activity towards the iodine/triiodide redox system.⁶⁶

Reaction (6) must proceed slowly as compared to the electron injection and regeneration of dyes in order to have significant charge separation.

The kinetics of reaction (6) follows a multiexponential time law, taking place on a microsecond to millisecond time scale as compared to ultrafast electron injection.^{108,109} It depends on the density of electrons in the semiconductor and the intensity of light.

Recombination of electrons in TiO₂ with triiodide in the electrolyte is usually characterized by the electron lifetime. Long lifetimes (1-20 ms) are observed with the I⁻/I₃⁻ redox couple under 1 sun light intensity.

2.5. PERFORMANCE EVALUATION OF DSSC

One of the standard characterization techniques of solar cells is to measure current density-voltage (J-V) curves under standard illumination and temperature conditions. A circuit and a typical J-V curve for a photovoltaic cell are shown in Figure 2-5 and Figure 2-6, respectively. In Figure 2-5, J_{SC} represents photocurrent source. R_S is the series resistance including charge transfer resistances, ionic transport, and resistive losses in the electrodes, and R_P is the shunt resistance and it is attributed to the recombination processes in solar cells. These two resistances affect the shape of the J-V curve. Analysis of the J-V curves includes the determination of the following parameters:

2.5.1 Short-circuit current density (J_{SC})

This is the maximum current density produced by the cell. J_{SC} is measured at an applied potential of zero volt. J_{SC} is a function of the illumination intensity.

2.5.2 Open-circuit potential (V_{OC})

This is the maximum voltage produced by the cell, measured when the current in the cell is zero. Theoretically, open-circuit corresponds to an almost flat band condition. In a DSSC, it is mainly determined by the difference between Fermi level of TiO_2 and redox potential of the electrolyte.

2.5.3 Maximum power point (MPP)

The point in the J-V curve yielding the maximum absolute value of the product of current density and voltage, i.e. maximum power density (P_{max}), is called the maximum power point. It corresponds to the area of the largest rectangle that can fit inside the JV curve of the cell, as shown in Figure 2-6.

2.5.4 Fill factor (FF)

FF is the ratio of the maximum power density to the product of short-circuit current density and open-circuit voltage:

$$FF = \frac{J_{MPP} \cdot V_{MPP}}{J_{sc} \cdot V_{OC}}$$

This parameter indicates the deviation of the measured J-V characteristic from ideal J-V characteristics.

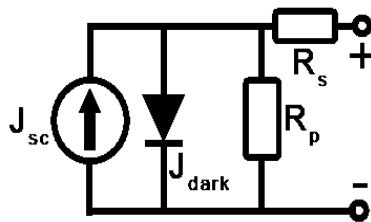


Figure 2-5: Circuit of a typical photovoltaic cell.

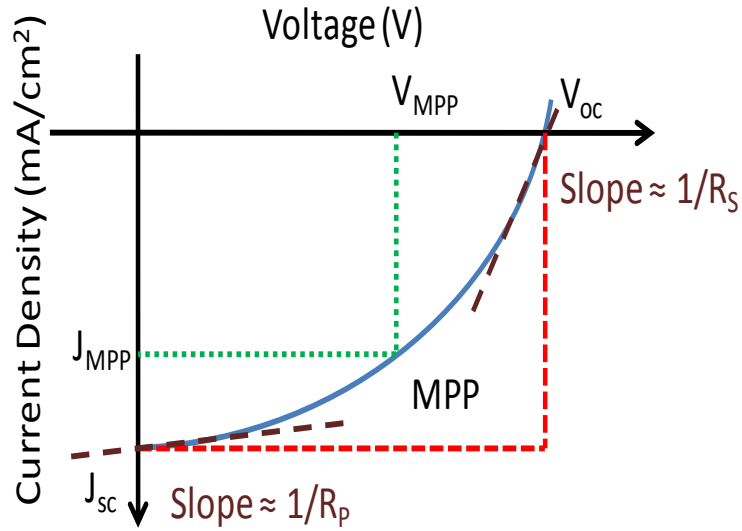


Figure 2-6: Typical shape of the J-V curve of a photovoltaic cell.

2.5.5 Power conversion efficiency (η)

The power conversion efficiency describes the overall performance of the solar cell and is defined as the maximum power produced by the cell (P_{max}) divided by the power incident on the active area of the cell (P_{Light}):

$$\text{Efficiency } (\eta) = \frac{P_{max}}{P_{Light}}$$

In order to compare results from various laboratories, standard measurement conditions have been developed. Under standard conditions while testing solar cells, the light intensity should be 1000 W/m^2 , the light source should have spectral distribution of that of AM1.5 G solar spectrum, and the temperature of the cell should be 25°C . The power output of the solar cell at these conditions is the nominal power of the cell.

CHAPTER 3 BACKGROUND ON CARBON NANOTUBES (CNTs)

This chapter deals with the structure and general background of carbon nanotubes (CNTs). Well known synthesis methods are also discussed in detail.

3.1. CARBON NANOTUBES (CNTs)

Sumio Iijima, an electron microscopist working at the NEC laboratories in Japan, discovered fullerene-based CNTs in 1991 during arc-discharge synthesis of C_{60} .¹¹⁰ Since then, a tremendous amount of research has been conducted to explore synthesis routes/methods, and many different applications due to the extraordinary properties of CNTs.

There are a variety of carbon nanotubes, but only two have been studied extensively, namely single-walled carbon nanotubes (SWCNTs) and multi-walled carbon nanotubes (MWCNTs). SWCNTs consist of a single graphene sheet of sp^2 covalently bonded carbon atoms seamlessly joined as a cylindrical tube, typically 0.7-10 nm in diameter. SWCNTs can be either metallic or semiconducting, depending upon the direction about which the graphene sheet is rolled to form a cylinder, described by the chiral vector (C_h). Various types of SWCNTs are shown in Figure 3-1. Types of SWCNTs can be defined using a pair of integers (n, m) in their lattice representation. The CNT is of the armchair type with $n = m$, zigzag with $n = 0$ or $m = 0$ and chiral for all other (n, m).

$$C_h = na_1 + ma_2 \equiv (n, m), (n, m \text{ are integers}, 0 \leq |m| \leq n)$$

The diameter of the CNT can be calculated using the chiral indices according to

$$d = \frac{\text{circumference}}{\pi} = \sqrt{C_h \cdot C_h} = \frac{a}{\pi} \sqrt{n^2 + m^2 + nm}$$

where $a \approx 2.49 \text{ \AA}$ is a lattice constant slightly greater than typical C-C bond length.¹¹¹

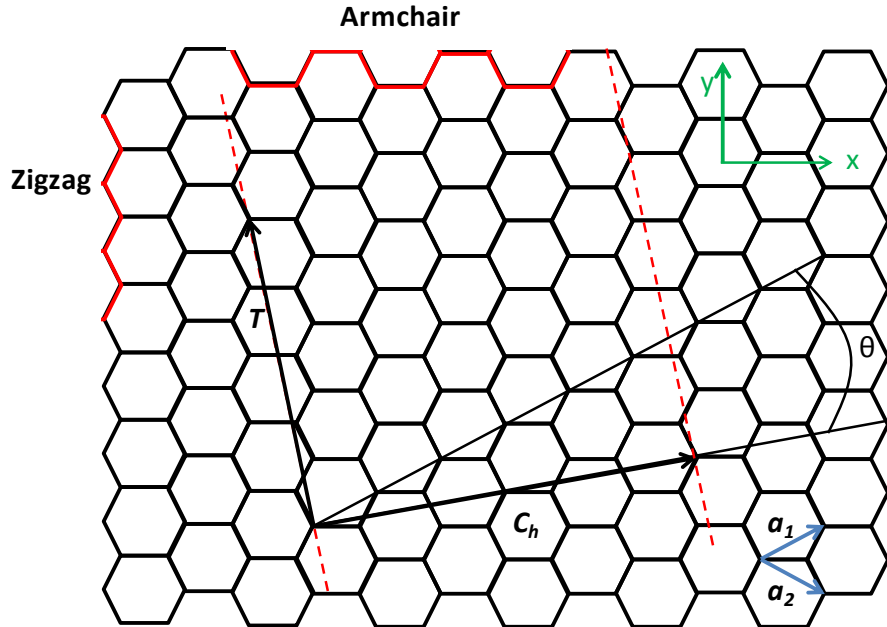


Figure 3-1: Unrolled graphite sheet to construct CNT with chiral vector C_h and a_1 and a_2 are unit vectors. T is the translational vector of nanotube and ' θ ' is the chiral angle¹¹¹.

MWCNTs, which typically have larger diameters, consist of coaxial layers of graphene bonded together through van der Waals forces. Their lengths can vary from several microns to millimeters; their properties are different than those of the SWCNTs. For instance, MWCNTs are mostly metallic but SWCNTs can be either metallic or semiconducting.¹¹²

3.2. SYNTHESIS ROUTES/METHODS

Several ways have been explored to synthesize CNTs. Arc-discharge, laser ablation and chemical vapor deposition (CVD) are well known and are of widespread use. An overall description of each of these is given in the following sections.

3.2.1. Arc-discharge

The arc-discharge method is a process using high temperatures to produce CNTs. In the arc-discharge method, an arc is ignited between two electrodes, typically made from graphite, in a gaseous environment, see Figure 3-2. Carbon is evaporated due to arcing,

cools and condenses in the form of filamentous product that is comprised of multi-walled carbon nanotubes. With modification, single-walled carbon nanotubes can also be produced using this method.

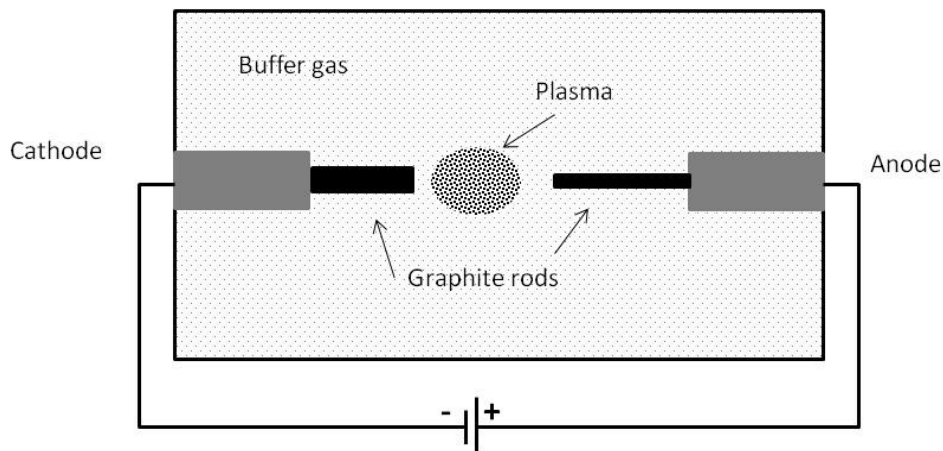


Figure 3-2: Schematic diagram of an arc-discharge system.

3.2.2. Laser Ablation

In the laser ablation method, see Figure 3-3, an intense laser beam (Nd:YAG laser beam, for instance¹¹³) is directed at a carbon surface, typically graphite in a gaseous background. The evaporated carbon condenses on the cold finger (collector) in the form of CNTs. By controlling the process parameters, CNT yield and diameter distribution can be controlled. For bulk production of CNTs, this method is not appropriate but its other features such as CNT quality, diameter control and their distribution makes this a good choice for SWCNT samples for various laboratory applications.

CNTs produced by laser ablation are uniform in diameter, in the form of bundles consisting of hundreds of SWCNTs having diameter 5–20 nm and tens to hundreds of μm length.^{114,115}

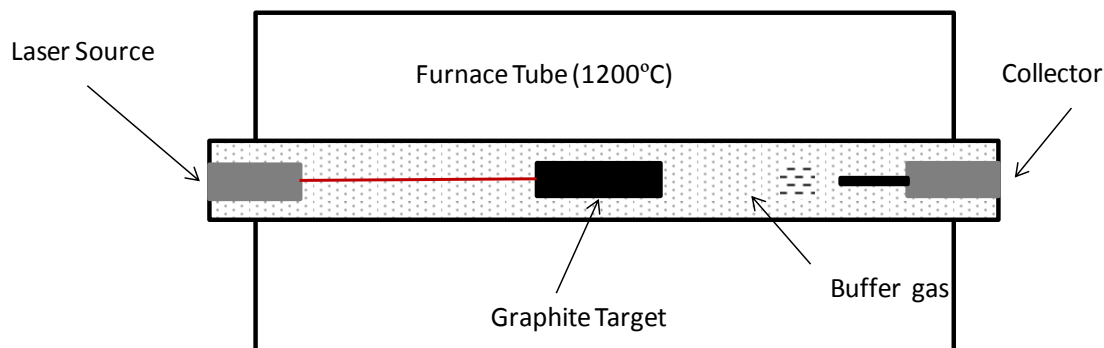


Figure 3-3: Schematic diagram of a laser ablation system.

3.2.3. Chemical vapor deposition (CVD)

In CVD, volatile precursors are used as carbon sources to a catalyst at growth temperatures of 500°C-1200°C (Figure 3-4). Types of CVD methods include thermochemical CVD and plasma enhanced CVD etc. In a typical CVD process, a carbon source gas decomposes, saturates on the catalyst particles and precipitates to form carbon nanotubes.¹¹⁶

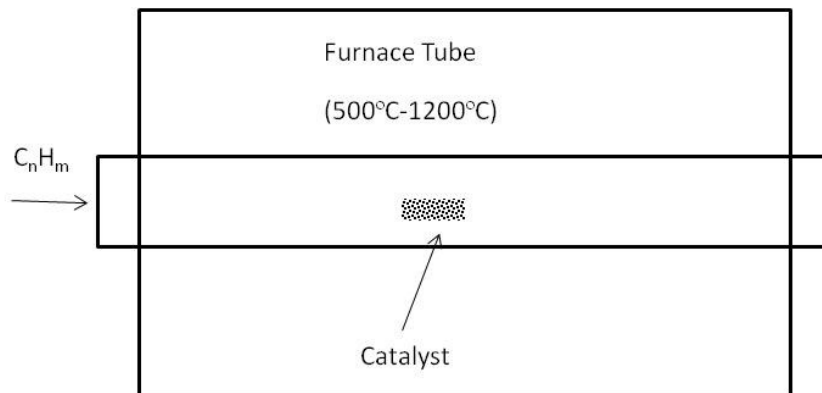


Figure 3-4: Schematic diagram of a chemical vapour deposition system.

In 1988, Endo for the first time, synthesized carbon nanotubes using catalytic decomposition of benzene vapors over an iron catalyst at 1100°C.¹¹⁷ Since, a lot of work has been done on the growth of single-walled and multi-walled CNTs over supported catalysts or with floating catalysts.^{118,119,120,121,122,123} CNTs diameters can be modified by

controlling the catalyst particle size. Transition metals such as Fe, Co and Ni and their alloys are well known catalysts for CNT growth.

3.3. VERTICALLY-ALIGNED CNTs (VACNTs) GROWTH

The CVD method is widely used due to its simple process, relatively low temperature requirement, low-costs and large-scale capability. In addition, CVD has been successfully used to grow relatively pure and aligned CNTs.^{124,125,126}

Extensive literature is available for growing vertically-aligned CNTs.¹²⁷ Here some of the methods of interest are discussed. One method is to use ethylene as a carbon source gas with ammonia and argon as process gases on various substrates. In this case, iron is used as the catalyst, with a growth temperature of typically 720°C. Another method is to use carbon monoxide as a carbon source gas, with hydrogen and argon as process gases and invar, an alloy (Ni:Co:Fe), as a catalyst at 580°C. Yet another method is a modification of the above, with methanol used as the carbon source instead of carbon monoxide. Finally, a well-known and popular method to produce vertically aligned CNT forest of longer heights is the so-called water assisted method.¹²⁸ In this method, ethylene is used as carbon source gas with hydrogen, H₂O and argon as process gases. Iron on alumina was used as catalyst on various substrates at 750°C. These procedures are discussed in detail in chapter 4.2.3.

3.3.1 Growth mechanism of CNTs

CNT growth mechanisms are under investigation and are not well understood. However, an extensive amount of work has been done, in which a number of hypotheses are proposed by the scientific community. The wide variety of growth conditions make it difficult to propose a single mechanism of CNT growth. Therefore, the true growth mechanism may be a combination of these proposed growth hypotheses. The proposed mechanisms can be summarized as follows:

- While adsorbing on the surface of catalyst nanoparticles at elevated temperature, hydrocarbon molecules decompose and result in the formation of hydrogen and carbon species.
- Hydrogen desorbs while carbon species diffuse through or on the catalyst nanoparticles.
- Diffusing carbon species precipitate on the opposite surface of the catalyst nanoparticles, crystallizing into a cylindrical graphene network without any dangling bonds. Hydrocarbon decomposition is an exothermic process while carbon crystallization is an endothermic process. Thus, the growth process continues due to the heat gradient.

There are two common modes for CNTs growth, tip-growth mode and base-growth or root-growth mode.

In the tip-growth mode, see Figure 3-5 (upper), catalyst nanoparticles detach from the substrate due to weak catalyst-substrate interaction. Catalyst nanoparticles move along with the growth process, remaining at the tip of the growing CNTs. This growth process continues as the catalyst top is available for hydrocarbon decomposition.

In base-growth mode Figure 3-5 (lower), catalyst nanoparticles remain on the substrate due to strong catalyst-substrate interactions. Hydrocarbon molecules decompose, and carbon diffuses as in the tip-growth mode. The precipitation process, however, differs: catalyst nanoparticles are not able to detach from the substrate and hence, carbon initially crystallizes out as a hemisphere cap followed by the formation of a graphitic cylinder of CNTs leaving behind catalyst nanoparticles on the substrate.

Catalyst-substrate interaction is related to the wetting property that depends upon the contact angle of the catalyst with substrate at the elevated temperature. Nevertheless, this interaction depends on catalyst and substrate materials. The size of the catalyst nanoparticles determines whether MWCNTs or SWCNTs are formed.¹²⁹

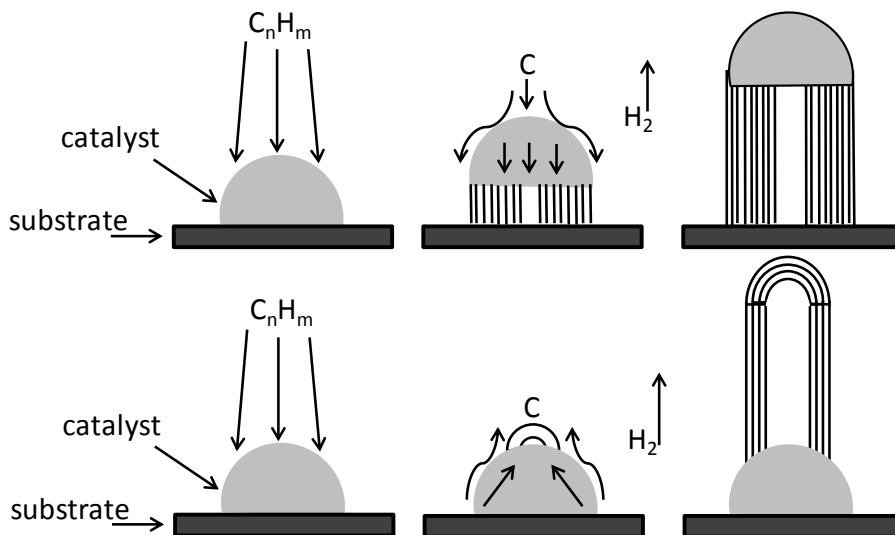


Figure 3-5: Schematic representation of CNT growth mechanism. Tip-growth (upper figure) and base-growth (lower figure).

3.4. 2-D CNT THIN FILMS AND THICK PAPERS

An alternative approach is to make two-dimensional CNT thin films and thick papers using the CNTs grown from methods described in previous section. CNT thin films and thick papers consist of randomly oriented CNTs held together by van der Waals interactions. Thin films of CNTs having thickness in the range of 10-100 nm exhibit high optical transparency and electrical conductivity, and thus have the potential to replace transparent conducting oxide electrodes such as indium tin-oxide (ITO).^{130,131,132,133} Furthermore, thick CNT nanoporous films (Buckypapers) can be used as electrodes for super capacitors, fuel cells, solar cells and battery applications.^{134,135,136,137}

3.4.1 Preparation of CNT Films

The most widely used preparation methods for CNT films are to disperse CNTs in a solvent, using ultrasonication. Surfactants or chemical modifications may be used to aid the process. CNT thin films are then prepared by evaporating the dispersion, spray coating, spin coating, or vacuum filtration.^{138,139} Among these methods, vacuum filtration

is a promising approach, as it facilitates surfactant removal.¹³⁸ Filtration also has many other advantages, such as uniform film thickness and easy control over thickness.¹⁴⁰ Nevertheless, procedures are needed to transfer these films from the filter membrane to desired substrate after filtration.¹³⁹

CHAPTER 4 EXPERIMENTAL METHODS

This chapter can be divided into four portions. The first portion describes the fabrication of Pt counter electrode DSSCs with ~10% efficiency. This includes step-by-step modifications in cell design, fabrication procedures and device characterization. In the second portion, all experimental work related to CNTs including their synthesis and their application in counter electrodes of DSSCs is presented. The third portion deals with the work done on nanocrystalline cellulose (NCC) and its application as a catalyst in CE of DSSCs. The fourth portion is about characterization techniques used in this work.

4.1. FABRICATION OF NORMAL DSSC

4.1.1 Preparation of photoanode

4.1.1.1 Substrates

Glass coated with fluorine-doped tin oxide (FTO-coated glass, TCO22-15) was purchased from Solaronix. These were cut into 2.5 cm x 2.5 cm substrates. Ethanol (nominally 100%) was purchased from Commercial Alcohols Inc. Before TiO₂ deposition, the substrates were cleaned using the following procedure:

- Sonicated in detergent for 2 minutes
- Rinsed with DI water
- Sonicated in DI water for 10 minutes
- Rinsed with ethanol
- Sonicated in ethanol for 15 minutes and blow dried
- Cleaned in oxygen plasma etcher for 1 minute at 200 mTorr, 250 W and oxygen flow rate of 20 sccm where sccm is standard cubic centimeter per minute. One standard cubic centimeter of gas is defined at 0°C and 1 atm.

4.1.1.2 Depositing the TiO₂ layer

Porous nanocrystalline TiO₂ layers can be deposited by tape casting techniques¹⁴¹, screen printing¹⁴² or spray painting.¹⁴³ Subsequently, TiO₂ is sintered at 450°C for 30 minutes.

Nanoporous TiO₂ films have high specific surface areas, typically a factor of ~1000 larger than the area of the film. This porosity facilitates dye uptake. TiO₂ nanoporous films typically contain a mixture of small size (20 nm) and large size (250-300 nm) TiO₂ nanoparticles. These larger particles scatter photons into the plane of the film, which in turn improve light-harvesting efficiency by increasing the average path length that a photon travels through the film.

In this work, TiO₂ paste (18NR-O) was purchased from Dyesol Limited. Titania paste has 30 wt% TiO₂ loading. It consists of 20 wt% of 20 nm and 10 wt% of 200 nm anatase nanoparticles. The TiO₂ layer was deposited on FTO-coated glass by screen printing using a 43-thread/cm mesh. Initially, the area of TiO₂ layer was 1 cm² reduced to 0.04 cm² in later cells, as discussed below, which also defined the area of the DSSC. After screen printing, the photoanode was calcined in air in a Lindbergh furnace with the following program:

- 10°C/ minute to 100°C
- Hold at 100°C 20 minutes
- 20°C/ minute to 450°C
- Hold at 450°C 30 minutes and cool down to room temperature

When completed, the films had a bone-white colour. The thickness of the TiO₂ film was 12 µm. The properties of the nanostructured TiO₂ electrodes are crucial for the efficiency of the DSSCs. Controlling the morphology and interfacial properties of the TiO₂ electrode is critical to preparing high efficiency DSSC. For example, the internal surface area of the film determines the dye uptake, the pore size distribution affects ion diffusion, the particle size distribution determines the optical scattering properties, and the electron percolation depends on the interconnection of the TiO₂ particles.¹⁴⁴ The scattering properties of the film are important for light harvesting efficiency of the film once a monolayer of dye is deposited on it. Efficient light harvesting can be achieved by using mixture of larger and smaller TiO₂ particles in the film.

4.1.1.3 Dye impregnation of the electrodes

A monolayer of dye molecules is formed on the nanostructured TiO₂ electrode by immersing the sintered electrode into a dye solution for a long enough period to fully impregnate the electrode. The electrode is sensitive to moisture during the impregnation process.¹⁴³ In order to avoid moisture, the electrode should be warm before immersing it into the dye solution.

A Ru-based complex called N3 dye (see Figure 4-1) was purchased from Dyesol Limited. A solution was prepared by sonicating 30 mg of N3 powder in 150 mL of ethanol in a clean beaker with a Teflon lid for 30 minutes. The bath was protected with opaque covers. Before putting the electrode into the bath, the substrates were heated to 70°C in order to get rid of moisture. The electrode was immersed for 24 hrs in the dye solution at room temperature. The electrode was removed from the dye solution and rinsed with ethanol. The dyed TiO₂ layer was purple in colour due to dye absorption.

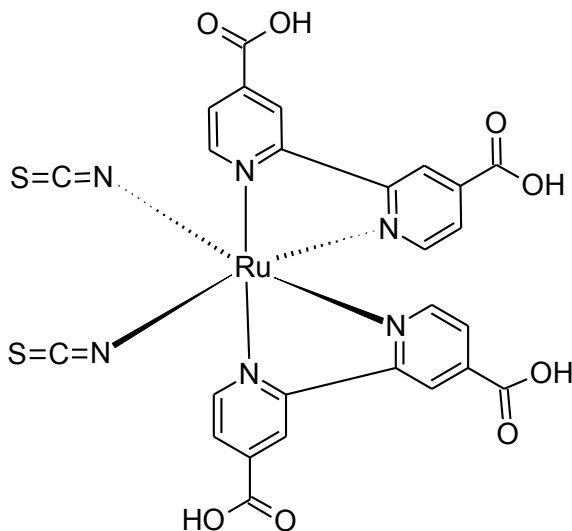


Figure 4-1: Structure of N3 dye molecule.

4.1.2 Preparation of counter electrode

Platinum was used as a catalyst for triiodide reduction. It was deposited on indium tin-oxide (ITO) substrate using sputtering at 50 W DC in ~ 0.85 mTorr argon gas. The platinum layer was very reflective and it was expected that it increased conversion

efficiency by reflecting light back to photoanode, further increasing the probability of photon absorption.

4.1.3 Sealing the cell and filling of electrolyte

Thermal adhesive polymer sheets such as Surlyn (25 μm and 60 μm thickness) were purchased from Dyesol Limited and were used as a sealing material. A series of modifications were performed to optimize the sealing and filling procedure: Surlyn was cut to fit around the TiO_2 layer as shown in Figure 4-2 (a-d).

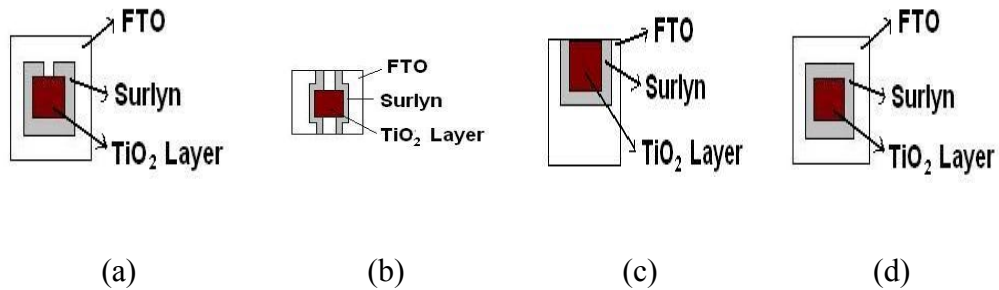


Figure 4-2 (a-d): Various modifications in cell design.

Finally, the sealant design shown in Figure 4-2 (d) was used. This was the most preferable design as it facilitated both filling and sealing. To use this design, holes (0.75 mm in dia.) were drilled in ITO counter electrodes before platinum deposition using diamond drill bits.

In the optimized sealant design, Surlyn was placed on the photoanode and the counter electrode was put on it in such a way that the platinum and TiO_2 faced each other, see Figure 4-3. This unit was placed on a hot plate at 120°C for 1 minute under a small mass of 0.45 kg. A good seal should have no bubbles, look transparent and be difficult to pry apart once cool.

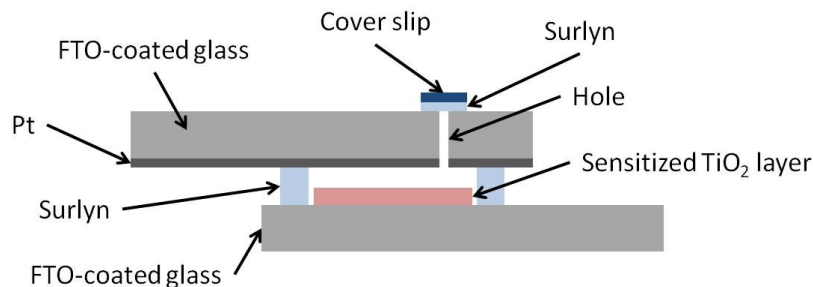


Figure 4-3: DSSC assembling (cross-sectional view, not to scale).

Electrolyte (EL 141) was purchased from Dyesol Limited. The electrolyte was filled through the drilled holes on the counter electrode with a micropipette. A good filling should not have any air bubbles. After filling the cell with electrolyte, it was wiped with acetone to remove any electrolyte on the outside of the cell. A piece of Surlyn and a piece of glass cover slip were used to seal the filling holes. This final seal was made by heating and applying pressure to the cover slip using a soldering iron.

4.1.4 Further modifications to the cell design

Modifications were also performed to optimize the cell design and fabrication procedures as discussed below:

- After screen printing the TiO_2 layer, it was left under ambient conditions to flow for some time with the aim of reducing surface irregularity of the TiO_2 layer.
- In DSSCs, dark current is produced due to the recombination of charge carriers by reduction of I_3^- at the dye-free sites at the TiO_2 particle surfaces or the FTO surface. This results in a loss of photocurrent. In order to reduce the possible dark current at the TCO-electrolyte interface and further improve the specific surface area of the TiO_2 electrode, a TiO_2 (particles size 20 nm) underlayer was introduced between the TCO and the screen printed TiO_2 layer. This layer is also called a blocking/compact layer. TiO_2 (Aerodisp, W740X) was purchased from Evonic Degussa Corporation as a dispersion in DI water. This layer (1.5 μm) was deposited by spin coating at 1500 rpm for 1 minute. After spin coating, the electrode was annealed for 6 minutes at 125°C on a hot plate. Subsequently, it

was calcinated in air at 450°C for 30 minutes prior to screen printing of the TiO₂ paste overlayer. The photoanode design is shown in Figure 4-4.

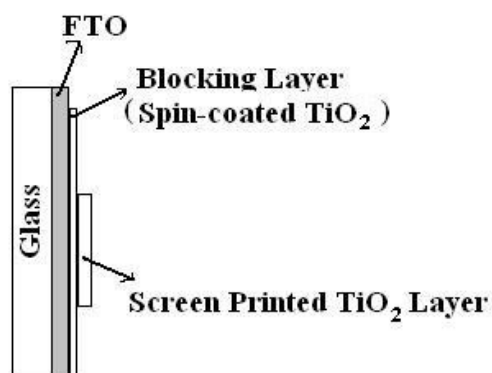


Figure 4-4: Photoanode with blocking layer.

- Exposure of cell area under illumination

It was also found that while testing DSSCs, the full cell area (1 cm²) was not exposed under the sun illumination due to limitation in our testing setup. In this case, the un-exposed area was contributing dark current into the overall photocurrent, thus decreasing the overall efficiency of device. In order to exploit maximum performance of device, DSSCs with smaller area (0.04 cm²; defined by 2mm x 2mm printing screen aperture) were fabricated and fully exposed under *AM 1.5G* illumination.

- TiCl₄ treatment of the TiO₂ electrode

Following calcinations, the TiO₂ electrode was treated with TiCl₄ solution: the photoanode was soaked in 40 mM TiCl₄ aqueous solution at 70°C for 30 min in an oven. After this, it was rinsed with DI water and ethanol, respectively, and blow dried. It was again sintered in a furnace at 450°C for 30 minutes. After cooling to 80°C, the TiO₂ was immersed in N3 dye solution. Studies have shown that TiCl₄ treatment of the TiO₂ electrode improves the efficiency of DSSC.¹⁴⁵ This treatment increases necking between TiO₂ particles that facilitates the percolation of the electron from one particle to another that leads to an increase in photocurrent and hence the efficiency of the DSSC.

4.2. CARBON NANOTUBES (CNTs)

4.2.1 Preparation of CNT thin films and CNT thick papers

Vacuum filtration of a suspension of dispersed CNTs is a common and convenient method^{146,147} to prepare randomly oriented 2D networks with control of film area and thickness. In addition to this, it also has the advantages of easy, rapid, solvent-free detachment that further provides a simplistic method to transfer these CNTs films to desirable substrates. CNT films are promising materials for use as electrodes because of their low sheet resistance, transparent properties and flexibility.

SWCNTs were purchased from Helix Material Solutions, Inc. Thin CNT films were prepared using a vacuum filtration procedure.¹⁴⁸ Suspensions of SWCNTs were prepared via ultrasonication of 0.05 mg/mL of SWCNTs in nanopure water ($> 18 \text{ M}\Omega \text{ cm}$) with 2 mass% sodium cholate (sodium cholate hydrate, 98%, Aldrich). Here, sodium cholate was used as a surfactant. Carbon nanotubes that did not disperse well (clumps) were removed by centrifuging first at 8000 rpm, and then 4000 rpm. The supernatant was pipetted out after each centrifuging step. Known volumes of the suspensions were diluted with an equal volume of nanopure water. These were then vacuum-filtered through cellulose acetate filter membranes (Advantec, 47 mm diameter, 0.22 μm pore size) to prepare thin SWCNT films. In order to detach these SWCNT films from the filter membrane, they were rinsed and then submerged in nanopure water.

Similarly, thick papers were made by vacuum filtering the above suspension including undispersed clumps of SWCNTs.

4.2.2 Growth of vertical aligned carbon nanotubes (VACNTs) directly on substrates

The objective of this work was to grow VACNTs directly on FTO so that it could be used as a counter electrode in DSSCs.

Chemical vapor deposition (CVD) was used to grow vertically aligned carbon nanotubes (VACNTs).¹⁴⁹ In a typical CVD process, volatile precursor gases decompose on the surface of a substrate at elevated temperatures and recombine to produce the desired material. During this process, volatile byproducts are also produced, which can be removed by flowing carrier gases through the chamber.

The CVD setup includes a Lindberg tube furnace (model TF55035A) having a simple quartz tube (Technical Glass Products Inc., type 214, I.D. 22 mm, O.D. 25 mm) inside it as a CVD chamber, see Figure 4-5. The flow rates of all the gases used (Ar, NH₃, H₂, CO and C₂H₄, Praxair reagent grade) were controlled with calibrated flow meters.

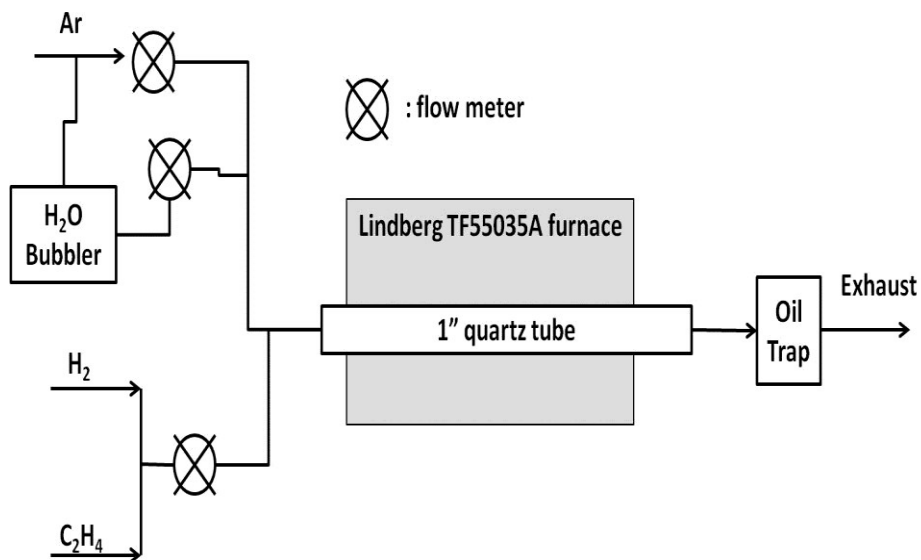


Figure 4-5: Schematic diagram of the WA-CVD apparatus setup for CNTs growth.

4.2.2.1 Carbon nanotube synthesis considerations and challenges

VACNT growth depends on many parameters including the type of catalysts and their pattern, the type of substrates, the carbon source and the etchant gases. These parameters are interrelated; several studies have been done to explore these interrelationships and their trends.^{150,151,152,153,154,155}

4.2.2.2 Methods of synthesis

There are many methods for synthesizing CNTs.^{110,156} Typically, chemical vapor deposition (CVD) and catalytic plasma enhanced chemical vapor deposition (PECVD) are better than laser ablation and arc discharge as only CVD and PECVD allow controlled synthesis. The diameter of CNTs can be controlled by the size of metal catalyst nanoparticles, and their length can be controlled by the combination of process gases, their flow rates, growth temperature and time. In this work, we used CVD for synthesizing VACNTs. CVD methods typically require high growth temperature (700°C-1000°C) for CNTs, not suitable for FTO substrates. Here, we have optimized the CVD method to grow CNTs on FTO at temperatures of ~ 550°C.

4.2.2.3 Substrates

The substrate is a key component in CNT synthesis, interfacing with the catalyst and interacting with the growth environment. Silicon/silicon dioxide is one of the most commonly used substrates, although there are an almost infinite number of possible choices. There are several concerns regarding the selection of substrate including deposition of catalyst, incompatibility with catalyst materials, the gases involved, and growth temperature. Our initial substrate choice was FTO. This was not feasible, due to several issues:

- It can't withstand at temperatures greater than 550°C due to glass softening.
- In CVD at 720°C under flowing carbon source gases (hydrocarbon gases such as NH₃, C₂H₄) or even process gases (H₂), the sheet resistance of FTO becomes very high and tin oxide is reduced to metallic tin.

To address these issues, extensive work was done on different substrates for growing CNTs directly on them such as silicon, quartz, aluminum alloy (6061, McMaster Carr), stainless steel (316, McMaster Carr) and copper foil (McMaster Carr).

4.2.2.4 Catalysts

The growth of CNTs is controlled catalytically. The catalyst particle breaks bonds and adsorbs carbon at its surface. This carbon then diffuses through or around the catalyst surface where it forms graphitic planes.¹⁵⁷ Initially, iron has been used as a catalyst in this

work, although other catalysts were also investigated including Ni and invar (Ni:Fe:Co = 42:52:6, (w/w/w)].

4.2.2.5 Methods of catalyst preparation

Catalyst particles can be prepared in many ways including physical vapor deposition (PVD), electro- and electro-less plating, and co-precipitation methods. The most common method is to deposit a thin film of catalyst using sputtering or evaporation techniques and subsequently annealing it to form discrete nanoparticles through de-wetting of the metal. In this work, where not otherwise stated, the catalyst was deposited by electron beam evaporation or thermal evaporation from tungsten filaments.

4.2.3 CNTs CVD growth Procedures

In this work, four commonly used CVD procedures for growing CNTs were investigated and these are discussed in detail in the following sections. All parameters for each CVD method are the result of systematic optimization.

4.2.3.1 Method 1 (CVD growth of CNTs using NH₃ and C₂H₄)

Initially, SiO₂/Si wafers were used as substrates and iron was used as a catalyst in CVD growth of VACNTs. Iron was deposited using either sputtering or thermal and electron beam evaporation techniques.

In the case of sputtering, the iron catalyst was sputtered on a SiO₂/Si wafer using a “linear out” mask in order to deposit a linear gradient of iron from 0 to 4.5 nm at 15 W for 500 W-min over a distance of 76 mm. The argon flow rate was 7.5 sccm and chamber pressure was 2.25 mTorr. In case of thermal and electron beam evaporation, the iron layer has a uniform thickness of 2.1 nm and 2.5 nm, respectively.

After depositing iron on the substrates, these were annealed in O₂ using rapid thermal processing (RTP) at 550°C for 10 minutes. RTP was done using a Modular Process Tech. Corp. model RTP-600S. In a typical RTP process, before heating, the chamber was

purged with pure oxygen (Praxair 99.999% research grade) at 10 L/min for 5 minutes. The oxygen flow rate was then reduced to 2 L/min and the sample was heated at 20 to 30°C/s to 550°C, was held at 550°C for 10 minutes, and gradually cooled down to room temperature using nominal cooling rates of 25°C/s with 10 L/min O₂ flow.¹⁴⁹

In this method, a typical CVD experiment has the following steps:

- Substrate was loaded into the center of the chamber and end caps were installed.
- The chamber was evacuated to ~ 50 mTorr.
- The chamber was purged with argon.
- The chamber was flushed with argon at 300 sccm for 10 minutes.
- Argon flow was turned off.
- NH₃ flow was turned on at 420 sccm for 5 minutes.
- NH₃ flow was reduced to 70 sccm.
- The furnace was heated to 720°C at 1°C/sec.
- The system was held at 720°C for 5 minutes before ethylene valve was opened.
- Ethylene flow was turned on at 95 sccm for 20 minutes.
- Ethylene and NH₃ flow were turned off 2 minutes before the furnace began to cool; at the same time argon flow was turned on at 300 sccm.
- The furnace lid was opened to allow the chamber to cool rapidly.

4.2.3.2 Method 2 (CVD growth of CNTs using carbon monoxide and hydrogen)

The objective to use this method was to optimize the CNT growth temperature to as low as possible in order to grow CNTs on FTO. Various additional substrates were used (Si/SiO₂, quartz, stainless steel, aluminum alloy) as well as various catalysts (Fe and invar). Catalyst materials were deposited (layer thickness 6.5 nm) using electron beam evaporation. Prior to depositing invar catalyst on quartz substrates, a 35 nm layer of chromium was deposited. For growth temperature optimization, a range of temperatures (480°C-580°C) was considered. The detailed growth procedure was as follows:

- The sample was loaded into the tube furnace and then it was evacuated to ≤ 100 mTorr.
- The furnace tube was backfilled and purged with Ar (300 sccm) for 15 min prior to heating.
- The furnace was heated to 480°C-580°C at 30°C /minute.
- When the desired temperature was achieved, Ar flow was stopped and CO (80 sccm) and H₂ (1270 sccm) were introduced to the furnace tube for 30 minutes.
- When the furnace begun to cool, H₂ was turned off.
- Ar flow was maintained until the furnace cooled down to room temperature.

During each run of the above procedure, there was always a shiny layer deposited at the intake end of the furnace tube portion (inner walls), just inside the furnace. It was found by XRD that it was a layer of nickel oxide (NiO). Upon further investigation, we found that it was due to a process called the “Mond Process” in which CO reacts with Ni (our furnace tubing, regulator filter and diaphragm were made of stainless steel) to form nickel carbonyl at 50°C-60°C, which then decomposes into Ni at 200°C-250°C. Therefore, at the quartz tube end, which was inside the furnace (temperature 580°C), we had Ni deposited inside the walls of furnace tube.

4.2.3.3 Method 3 (CVD growth of CNTs using methanol and hydrogen)

In order to avoid above Ni deposition issue, we decided to use CO produced by the decomposition of methanol as methanol can be decomposed into CO and H₂ at 200°C-400°C.^{158,159} The detailed growth procedure was as follows:

- The sample was loaded into the tube furnace and then it was evacuated to ≤ 100 mTorr.
- The furnace tube was backfilled and purged with Ar (300 sccm) for 15 min prior to heating.
- The furnace is heated to 480°C-580°C at 30°C/minute.

- When the desired temperature achieved, Ar was stopped and H₂ was introduced into the tube in two streams: 600 sccm through the bubbler containing methanol, and 600 sccm directly into the reactor for 20 minutes.
- When the furnace was begun to cool, H₂ flow was turned off.
- Ar flow was maintained until the furnace cooled down to room temperature.

4.2.3.4 Method 4 (WA-CVD growth of CNTs using ethylene and hydrogen)

The water assisted CVD (WA-CVD) method is well known for giving remarkable features such as dense, impurity-free and vertically-aligned CNTs.¹²⁸ In this procedure, stainless steel (316) and copper foil were used as substrates and iron (~1.5 nm) on alumina (~10 nm) as the catalyst. The detailed procedure was as follows:

- The sample was loaded into the tube furnace and then it was evacuated to ≤ 100 mTorr.
- The furnace tube was backfilled and purged with Ar (300 sccm) for 15 min prior to heating.
- All gas lines were purged for approx. 15 minutes.
- Ethylene flow was stopped and furnace tube was purged for 5 minutes.
- Argon (300 sccm), hydrogen (200 sccm) and DI water vapor (4 sccm Ar through a DI water bubbler) were introduced to the reactor while the furnace was heated to 750°C at 60°C/min.
- The furnace was held at 750°C for 1 minute.
- Ethylene flow (100 sccm) was introduced for desired growth time.
- Ethylene flow was turned off before cooling of furnace.
- When the furnace began to cool, DI water vapor was turned off.
- When the furnace temperature reached below 500°C, H₂ flow was turned off.
- The furnace lid was opened for rapid cooling.
- Ar flow was maintained until the furnace was cooled down to room temperature.

4.3. NANOCRYSTALLINE CELLULOSE (NCC)

Here we present the first time that carbon derived from NCC after its pyrolysis has successfully been used as a catalyst to reduce triiodide in DSSCs.

Cellulose is one of the most abundant natural biopolymers available today. It is low cost, renewable, biodegradable and non-toxic. It is one of the emerging nano materials that have been a subject of a huge amount of research efforts in many different fields from food industry to pharmaceuticals¹⁶⁰. NCC can be derived from acid hydrolysis of cellulose fibers¹⁶¹; it has different properties as compared to cellulose such as nanoscale dimensionality, high strength, high surface area and special optical properties.¹⁶²

4.3.1 Counter electrodes for DSSC

An aqueous dispersion (5.5 wt %) of NCC (Nanocel, BioVision Technology Inc) was used as-received in this work. The chemical structure is shown in Figure 4-6. Carbon obtained after NCC pyrolysis was used as the counter electrode of the DSSCs as an alternate to Pt.

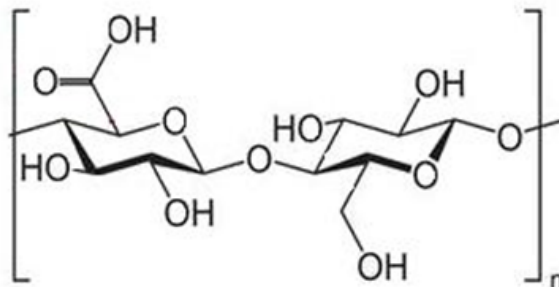


Figure 4-6: Chemical structure of Nanocel.

4.3.2 Pyrolysis

NCC films were prepared by drop casting the 5.5 wt% dispersion directly onto the counter electrode substrate. A drop of NCC solution ($\sim 10 \mu\text{L}$) was put on an FTO glass substrate and left to dry at room temperature. After drying, it was placed in Lindberg tube furnace (Model TF55035A) for pyrolysis under N_2 (UHP or research grade). An alumina piece was placed underneath the FTO glass substrate in order to avoid any deformation. The following procedure was used for NCC pyrolysis of this sample:

- The sample was loaded into the furnace tube and then it was evacuated to ≤ 100 mTorr.
- The furnace tube was backfilled with N_2 and then again evacuated. Evacuation and backfilling was done 3 times in order to make sure that no oxygen traces were left in the system.
- The furnace was purged with N_2 (100 sccm) for 1 hour prior to heating.
- Heating was done in two steps. In the first step, furnace was heated to 200°C at $3^\circ\text{C}/\text{minute}$ and was held at this temperature for 5 hours for dehydration. Then, in the second step, it was heated to 600°C at $3^\circ\text{C}/\text{minute}$ and was held at this temperature for 1 hour.

N_2 flow was maintained until the furnace cooled down to room temperature.

4.4. CHARACTERIZATION TECHNIQUES USED

4.4.1 Electrochemical impedance spectroscopy (EIS)

Impedance spectroscopy is a non-steady state technique that provides detailed information about internal system dynamics. It is a powerful method for the investigation of electrochemical properties of materials and their interfaces including kinetics, diffusion coefficients, charge transfer resistance and double layer capacitance. Time dependent electrical perturbation of the system of interest and the measurement of the response produce additional information about the internal processes. External perturbation such as AC potential modulation pushes the system out of equilibrium;

system response as a result of this small AC signal is monitored and analyzed over a range of frequencies.

Generally, analysis of EIS data is performed by fitting the frequency response to an equivalent circuit model. The equivalent circuit model typically consists of electrical elements such as resistors, capacitors, and inductors, representing various physical processes in the system. Care should be taken while fitting the equivalent circuit elements as there is the possibility to fit the same response with many different circuits. Therefore, a deep understanding of the system and its dominant physical processes is required to obtain meaningful results. It is also valuable to obtain information from other experimental techniques about the system before fitting the EIS data. As already mentioned, electrical elements are being used to identify the frequency response of a system, e.g., a parallel combination of a resistor and a capacitor is used to fit any electrochemical interfaces in system. In such equivalent circuits, resistors represent physical processes at any interfaces inside the system that cause resistance to charge flow in response to applied transient conditions without having a phase shift. This resistance is known as the “charge transfer resistance” and makes a significant contribution to the overall impedance of the system. The capacitors represent the physical processes in which an ionic double layer develops at the system interface, typically at the electrolyte/electrode interface in DSSCs. Furthermore, the overall series resistance of any system can also be represented by a resistor in the equivalent circuit. Another important and frequently used element is the “constant phase element” (CPE). It is an empirical element representing a physical process related to non-ideal capacitive behavior at the interface of a system and is defined as follows:

$$Z_{CPE} = \frac{1}{Q(i\omega)^n} \quad (0 \leq n \leq 1) \quad (4-1)^{163}$$

where Q is a proportional factor. For $n = 0$, Z_{CPE} represents impedance of a pure resistor ($Q = 1/R$) whereas for $n = 1$, it represents impedance of a pure capacitor ($Q = C$). The phase shift between the voltage and current is independent of frequency and equal to $n\pi/2$. This element is generally used when the electrode of the system is rough, having inhomogeneous reaction rates.

Let us consider one of the interfaces of electrochemical cell, such as the electrolyte/counter electrode interface, in series with a resistance representing transport in the electrolyte. As mentioned above, a parallel combination of resistor and a capacitor can be used to fit the Nyquist plot for this interface, as shown in Figure 4-7. Real and imaginary components of the impedance can be calculated as shown in equation 4-2. The resistor has only real impedance (R) and the capacitor has only imaginary impedance ($1/i\omega C$).

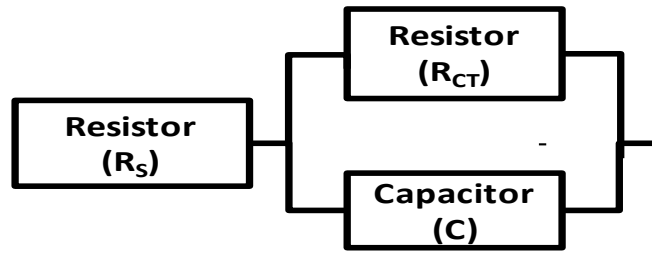


Figure 4-7: Typical equivalent circuit to model electrolyte/counter electrode interface and series resistance of an electrochemical cell.

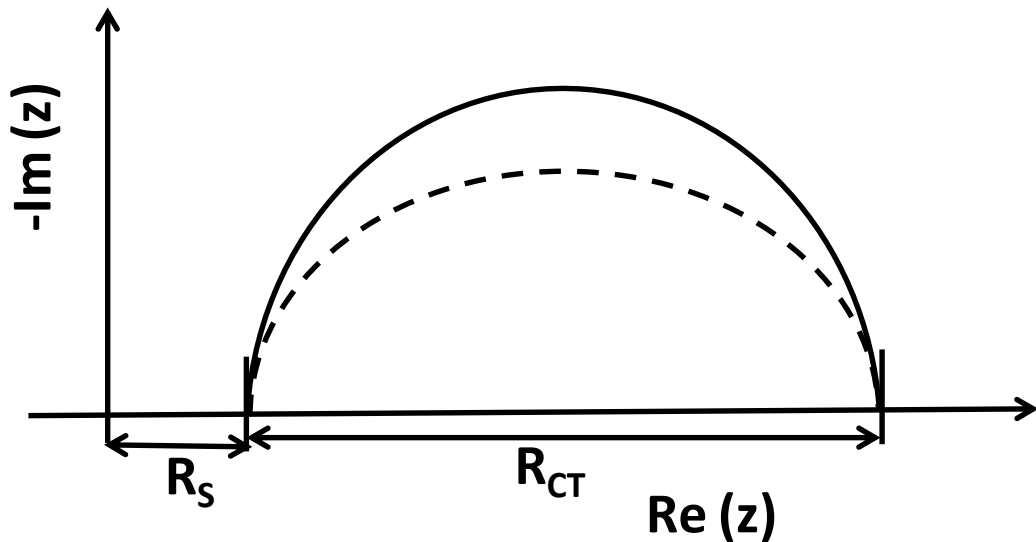


Figure 4-8: Nyquist plot for equivalent circuit to model electrolyte/counter electrode interface with charge transfer resistance, R_{CT} , in parallel with a capacitor (solid line) and CPE (dashed line) and series resistance, R_S .

$$Z = R_S + \frac{R_{CT}}{1 + R_{CT}^2 \omega^2 C^2} - i \frac{R_{CT}^2 \omega C}{1 + R_{CT}^2 \omega^2 C^2} \quad (4-2)$$

Here, R_S represents resistance to the ionic charges in the electrolyte, R_{CT} represents resistance to charge transfer at the interface, and C is the double-layer capacitance. At infinite and zero frequencies, impedance of this network is purely resistive. At intermediate frequencies, the impedance has both real and imaginary components, and will produce a semi-circular Nyquist plot ($\text{Im}(z)$ vs $\text{Re}(z)$), see Figure 4-8. In the case of a CPE, the semicircle is centered below the $\text{Re}(z)$ axis, resulting in a “flattened” semicircle as illustrated in Figure 4-8 (dashed line). In this work, EIS was performed using a Solartron Analytical ModuLab-ECS system on two-terminal electrochemical cells, spectra were collected at 0 V bias, 10 mV AC, between 1 MHz and 100 mHz. Spectra were analyzed using *z-view* software (version 3.2, Scribner Associates Inc., USA).

4.4.2 Cyclic Voltammetry (CV)

Cyclic voltammetry is an electrochemical method in which current is measured by applying a cyclic potential ramp to the working electrode of an electrochemical cell between low and high endpoints with a constant ramp. Usually, in a 3-electrode cell, the potential is applied with respect to a reference electrode. In the case of a 2-electrode cell (as reported here), the counter electrode doubles as a pseudo-reference electrode. It is a powerful technique that provides detailed information about electrochemical processes in terms of redox reactions within the cell. The oxidation potential (E_{pa}) and reduction potential (E_{pc}) for an active redox material can be found using this technique. Corresponding anodic (i_{pa}) and cathodic (i_{pc}) currents can also be found as shown in Figure 4-9. In case of reversible systems which are diffusion controlled, the ratio of cathodic current to anodic current is unity and separation between the current peaks is given by

$$\Delta E_p = E_{pa} - E_{pc} = \frac{59}{n} mV \quad (4-3)$$

where n is number of electrons involved in the reaction. E_p is independent of scan rate and current is proportional to $t^{-1/2}$ after E_p .

In the case of irreversible or quasi-irreversible systems, which are activation controlled, the electron exchange is slow. The splitting between potential peaks is larger than $\frac{59}{n} mV$.

This spreading of the peaks is an indication of an irreversible system. The height of the current peaks (i.e., $i(E_p)$) decreases in size as currents take more time to respond to the applied voltage as compared to reversible systems.

In general, CV is performed using a 3-electrode system, namely the working electrode (WE), counter electrode (CE) and reference electrode (RE). Working electrode is the electrode under study. The voltage is applied between the WE and RE whereas current flows between WE and CE. In case of using two electrodes (No RE), a small error is introduced, as the current flowing across the double layer at the CE results in a potential offset.

In this work, CV was performed using a Solartron Analytical ModuLab-ECS system on two-terminal electrochemical cells at 20 mV/s scan rate, unless otherwise noted.

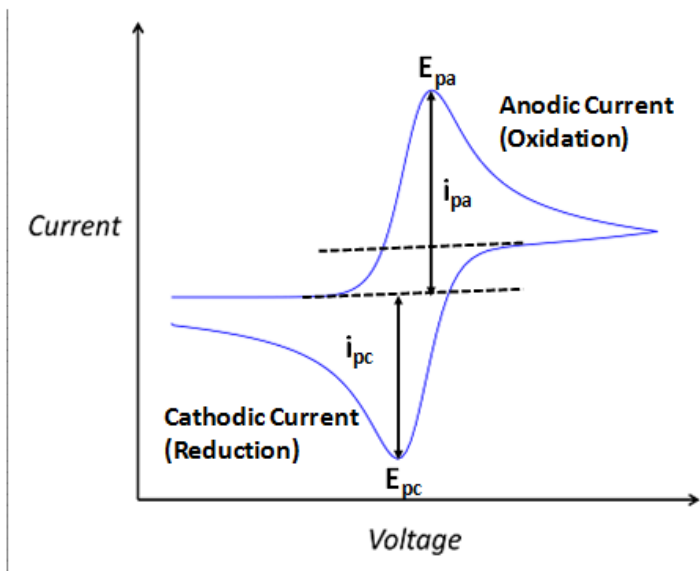


Figure 4-9: A typical cyclic voltammogram for reversible system.

4.4.3 Scanning electron microscopy (SEM)

The VACNT forests were investigated using a scanning electron microscope (SEM). In a typical SEM, a beam of high-energy electrons from a cathode (thermionic, field-emission) is accelerated towards an anode through a voltage difference between cathode

and anode. This electron beam has energy in the range of a few hundreds of eV to 100 keV. The electron beam is then focused on to the sample in the form of a narrow beam having a fine focal spot of 0.4 nm to 5 nm diameter by means of condenser lenses. The electron beam is generally scanned in a raster scan pattern. Upon reaching the sample, primary electrons lose their energy by scattering and absorption within an interaction volume that can extend in the range of ~ 100 nm to ~ 5 μ m below the surface of the sample. Due to energy exchange between the electron beam and the sample, a variety of signals are produced including secondary electrons, back scattered electrons, characteristic x-rays and heat. Secondary electrons, which are products of inelastic scattering, are commonly used to produce SEM images as these are most valuable to show morphology. These secondary electrons are detected by using secondary electron detectors i.e., Everhart-Thornley (E-T) detector. The SEM used in this work was a Hitachi S4700 cold field emission SEM. VACNT forest samples were mounted to an aluminum stage using conductive double-sided copper tape before insertion into the SEM chamber. In order to study VACNT length and morphology, scratches were made on various locations along the samples using a scalpel blade, as only the top surface of the VACNT forest could be otherwise observed with the SEM.

4.4.4 Small angle x-ray scattering (SAXS)

SAXS is a reliable and non-destructive technique for studying nanostructures. It provides information such as the size of the particles, their shapes and their spacing. In SAXS measurements (Figure 4-10), a monochromatic collimated beam of x-rays (\mathbf{K}_i) is brought to a sample. Upon interaction with the sample, some of the x-rays scatter elastically by electrons in the sample volume while the rest of them pass through the sample without interacting. The experimentally observed scattered intensity describes the constructive interference of the scattered x-rays (\mathbf{K}_s) as a function of scattering angle.

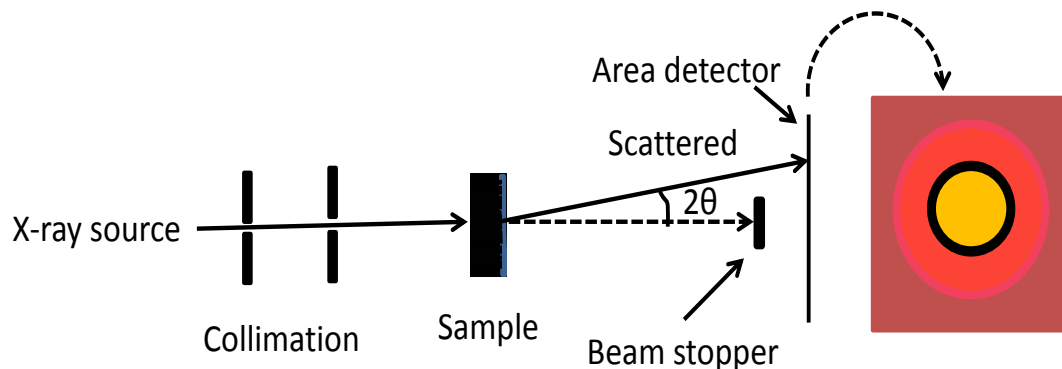
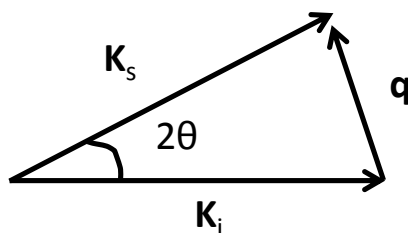


Figure 4-10: A schematic setup of a SAXS experiment.

The angle at which scattered x-rays are detected is denoted by 2θ . However in SAXS, scattering is generally determined in terms of the magnitude of the scattering vector $|\mathbf{q}|$ as defined in equation 4-4.



$$\mathbf{q} = \mathbf{K}_s - \mathbf{K}_i$$

$$|\mathbf{q}| = \frac{4\pi}{\lambda} \sin(\theta) \quad (4-4)$$

SAXS was done using a Bruker Nanostar system. The X-ray source was Cu $K\alpha$ having a wavelength (λ) of 1.54 Å. For SAXS measurements, a thin Cu foil (5 μm thickness) was used as the substrate to grow VACNTs because x-rays attenuate significantly less with Cu as compared to the same thickness (5 μm) of Fe, Ni and Cr, which are the main constituents of stainless steel. X-rays were incident parallel to the plane of VACNTs forest as shown in Figure 4-10. These VACNTs were modeled as cylinders. As there was no orientation in the plane, x-rays were scattered from these cylinders giving 2D plot in the form of circular rings on the area detector. Angular integration was performed to produce a plot of intensity versus scattering vector magnitude. After background subtraction, the position of the first broad peak maximum was used to calculate the

average radius of cylinder. This broad peak is due to the fact that there is a distribution of radii.

4.4.5 X-ray photoelectron spectroscopy (XPS)

X-ray photoelectron spectroscopy (XPS) is a surface analysis technique which is used to find elemental compositions and chemical states of elements present in the sample material.

The working principle of XPS is shown in Figure 4-11. X-rays having characteristic energy ($h\nu$) interact with the electrons in core shells of the elements in a sample and photo-excite these electrons from their initial states with characteristic binding energies (BE). These photoelectrons move through the sample to the surface. Some of them experienced inelastic scattering and appeared as a background in the XPS spectrum whereas photoelectrons generated near to the sample surface are emitted to the vacuum after overcoming the work function threshold (ϕ_S). The kinetic energy (KE) of this photoelectron in vacuum just outside the sample is given by $h\nu - BE - \phi_S$. Due to contact potential difference, the KE measured by the analyzer with work function ϕ_A and can be found as given below:

$$\begin{aligned} KE_A &= h\nu - BE - \phi_S - (\phi_A - \phi_S) \\ KE_A &= h\nu - BE - \phi_A \end{aligned} \quad (4-5)$$

Using equation (4-5), the BE of photoelectron can be determined as the analyzer work function (ϕ_A) is constant (~ 4.5 eV). Equation (4-5) is only valid for conductive samples where Fermi level is constant through the system. The analyzer must be calibrated using metal standards. For insulating samples, the Fermi level is not well defined making situation complicated. In this case, a common reference point, typically set to 285.0 eV¹⁶⁴, is considered by referring all peaks to the C 1s peak from hydrocarbon species that are always present on sample's surface loaded from air. Chemical states of the elements can be determined by finding shifts in the binding energies of these photoelectrons. These small shifts in binding energy are also referred to as chemical shifts. In a typical XPS spectrum, the electron count rate is presented as a function of binding energy. As KE and

BE have opposite signs, an increasing BE scale is plotted from right to left in an XPS spectrum. Peak splitting due to the interaction of the electron spin (s) and the orbital angular momentum (l) is observed in XPS. The total angular momentum can be represented by $j = |l + s|$. Therefore, an electron from a p orbital can have a j value of $1/2$ (higher binding energy) or $3/2$ (lower binding energy). The intensity ratios of these doublets can be found by the expression $(2j + 1)$. Therefore, for an electron from a p orbital, the relative intensities of the $1/2$ and $3/2$ peaks are 1:2. The line shapes in XPS are determined by the convolution of the natural line shape of the excitation source and the pass function of the analyzer. The analyzer contributes a Gaussian shape whereas the core level line shape is Lorentzian. The convolution is known as Voigt function. X-rays are generated by bombardment of high energy electrons on a metallic anode. The most popular anode materials used in XPS are magnesium and aluminum with typical x-ray excitation lines Mg K_{α} (1253.6 eV) and Al K_{α} (1486.6 eV), respectively.

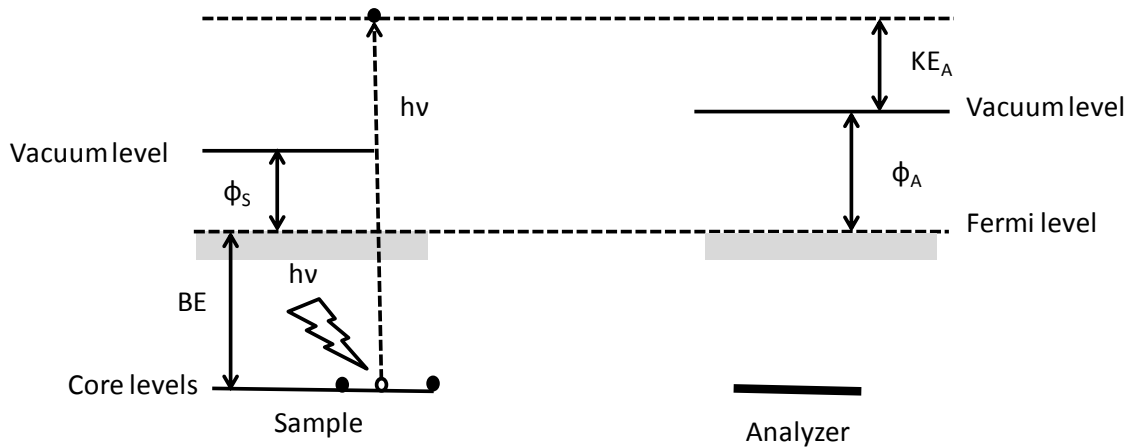


Figure 4-11: Working principle of XPS.

4.4.6 Mercury drop method for resistance measurements

A homemade setup was developed to measure resistance of the VACNTs forests. Mercury has property that it does not wet stainless steel, but it does wet gold¹⁶⁵. Therefore, in a stainless steel rod, a hole was drilled at one end. This hole was then filled with gold, so that mercury only wetted the gold. There was also a CCD camera attached to a microscope to measure the diameter of the circular contact between the Hg and the

CNTs. This is important while calculating the specific resistance of CNTs. The setup is given in Figure 4-12(a, b).

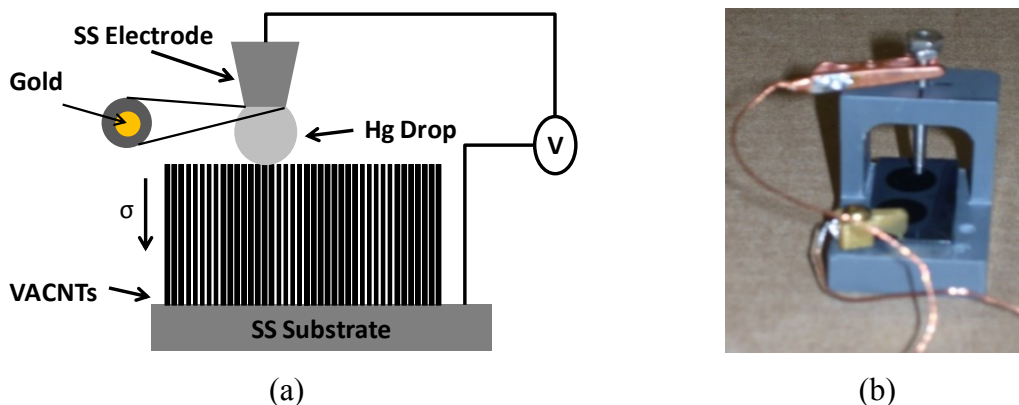


Figure 4-12: (a) Schematic diagram of setup and (b) built setup.

4.4.7 Thermal gravimetric analysis (TGA)

TGA works on the principle that all organic materials decompose if heated to a sufficiently high temperature. It is used to determine thermal stability, investigate decomposition reactions and measure inorganic content in organic material.

In TGA measurements, a controlled temperature program is applied to a substance and the change in mass is measured against time or temperature. Any change in mass can be associated with chemical change in the substance due to combustion, oxidation or decomposition.

In general, a sample is placed in a pan inside a furnace while being suspended from one arm of a precision balance. The change in weight of the sample is recorded while the sample undergoes the desired heating procedure. The TGA curve can be represented in either weight loss of a sample or in differential form and is called the thermogravimetric (TG) curve.

SDT Q600 (TA instruments) was used for TGA of VACNTs grown using the WA-CVD method and NCC after pyrolysis. VACNTs were removed from SS substrates after

synthesis. TGA was done for VACNTs under air (20 ml/min) at 5°C/min from room temperature to 800°C.

The NCC solution first was dried in a petri dish at room temperature. Dried NCC flakes were pyrolyzed using the heating procedure discussed in section 4.3.2. After pyrolysis, flakes were ground and 10-20 mg of the powder was loaded into the alumina pan of the TGA instrument. TGA was done under air (20 ml/min) at 5°C/min from room temperature to 1000°C.

4.4.8 Atomic force microscopy (AFM)

Atomic force microscopy was invented by Binnig et al. in 1986.¹⁶⁶ It is used to study the topography of surfaces with sub-nm resolution. A fine tip is attached to a cantilever which is made of either silicon or silicon nitride. The sample is typically mounted on a 3D piezoelectric scanner which is used to move the tip relative to the sample surface. The tip scans the surface in a raster pattern. The cantilever is deflected by the interaction forces between the tip and the sample surface. These forces are either attractive or repulsive depending upon the distance between the tip and sample surface. The bending of cantilever is detected by optical means using a laser beam as shown in Figure 4-13. This laser beam is reflected from the backside of the cantilever. The position-sensitive detector converts this reflected laser beam to an electronic signal used to generate the image of the sample surface under investigation. AFM can be used in different modes in order to study samples depending upon the type of sample and the required information. These techniques include contact mode, where the tip remains constantly in contact with the surface of the sample and “dynamic modes” such as tapping mode or non-contact mode.

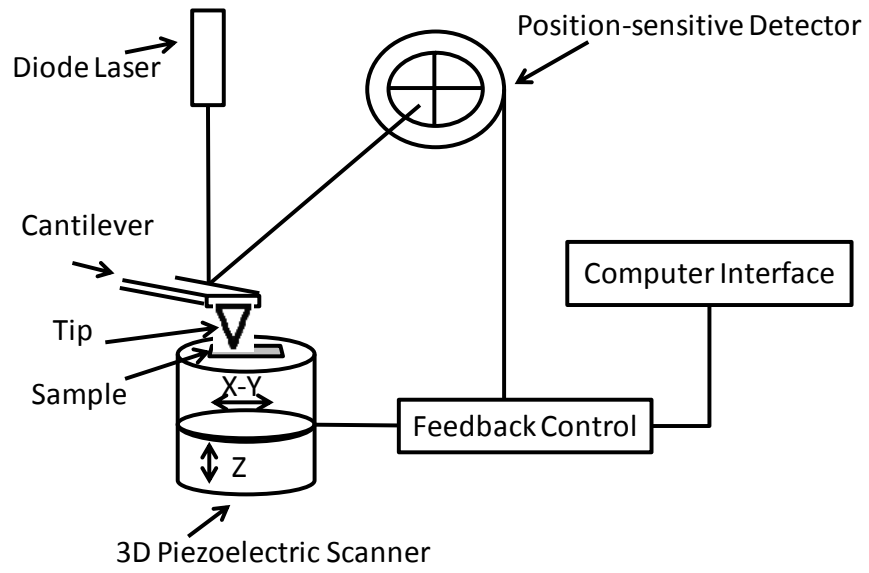


Figure 4-13: Working principle of AFM.

CHAPTER 5 PRELIMINARY WORK

The first part of this chapter is related to the work done on standard DSSCs based on Pt counter electrodes. Results regarding improvements in the device performance with step-by-step modifications are presented. In the second portion, work related to the application of CNT thin films and thick papers in counter electrode is discussed.

5.1. OPTIMIZATION OF NORMAL DSSCs

Fabrication of standard DSSCs with step-by-step modifications was discussed in chapter 4. The first DSSCs fabricated in this study had only a screen printed TiO_2 layer and was tested using standard conditions. Dark and illuminated J-V curves of a typical DSSC are shown in Figure 5-1. At 1 sun, it had $V_{OC} = 0.439$ V, $J_{SC} = 1.04$ mA/cm², FF = 45%, and an efficiency of 0.2%. It was found that the TiO_2 layer was not uniform, and the cell was not sealed or filled properly. In particular, there were bubbles and leakage in the sealing. Therefore, this device had a low power conversion efficiency.

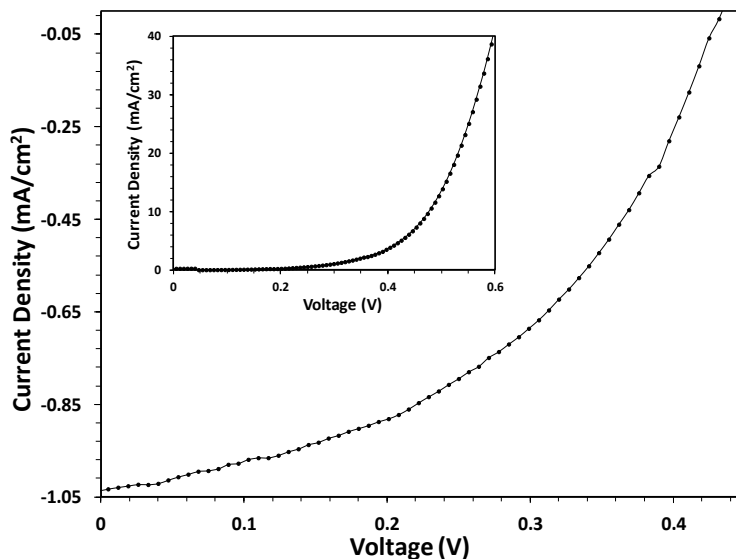


Figure 5-1: J-V of the first DSSC fabricated with only a screen printed TiO_2 photoanode and a Pt-based counter electrode at 1 sun. Inset: dark J-V.

The second DSSC was fabricated similarly to the first. This time, the sealing and filling were of higher quality. Dark and illuminated J-V curves of that DSSC are shown in Figure 5-2. At 1 sun, it had $V_{OC} = 0.538$ V, $J_{SC} = 3.64$ mA/cm², FF = 60%, and an efficiency of 1.2%. All parameters were improved.

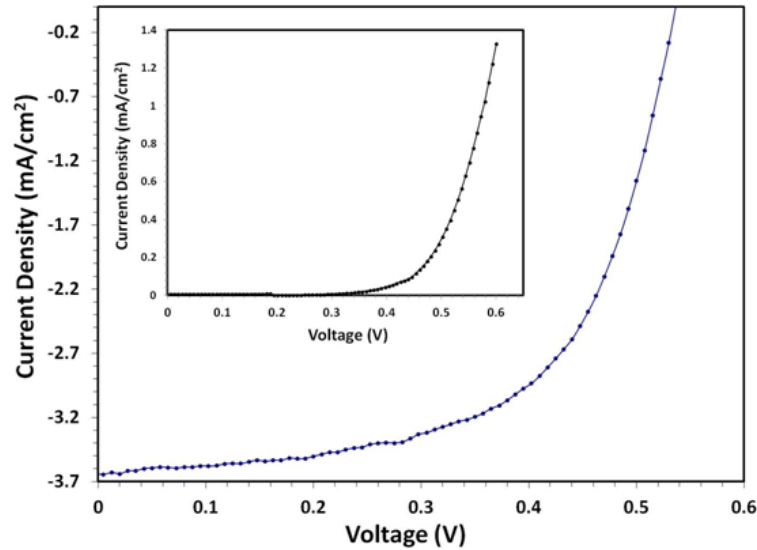


Figure 5-2: J-V of the second DSSC with improved sealing and filling at 1 sun. Inset: dark J-V.

A DSSC was then fabricated after employing the modifications discussed in chapter 4.1.4. Briefly, two layers of TiO₂ were used in this device. The first layer (spin-coated) served as a blocking layer to reduce recombination of photo-injected electrons in the FTO with the electrolyte and the second layer was screen printed as in case of original device. Dark and illuminated J-V curves for this modified device are shown in Figure 5-3. At 1 sun, this device showed a $V_{OC} = 0.631$ V, $J_{SC} = 8.91$ mA/cm², FF = 66%, and an efficiency of 3.72%. These were encouraging results as all performance parameters were higher than the device without a blocking layer of TiO₂.

Due to the variation of cell areas, and the continual improvement in fabrication techniques being developed, a quantitative analysis of the dark current with and without the blocking layer was not possible.

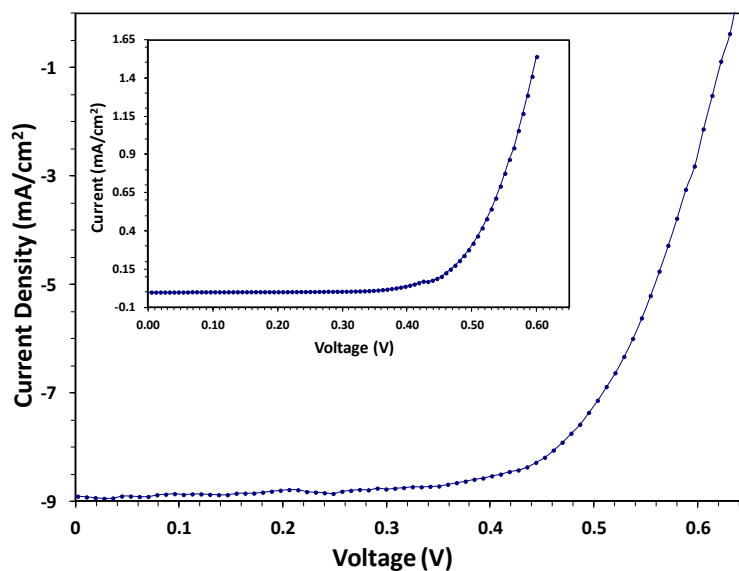


Figure 5-3: J-V of DSSC with spin-coated and screen printed TiO₂ layers at 1 sun. Inset: dark J-V.

The thickness and morphology of deposited TiO₂ layers were also investigated using a scanning electron microscope (SEM) [Hitachi S4700 cold field emission], see Figure 5-4 (a, b) and Figure 5-5 (a, b), respectively. Figure 5-4 (a) clearly shows that the TiO₂ paste used in screen printing is a mixture of 20 nm and 200 nm particles. The spin-coated TiO₂ layer is composed of 20 nm particles and has a thickness of ~ 1.5 μm as shown in Figure 5-5 (a, b).

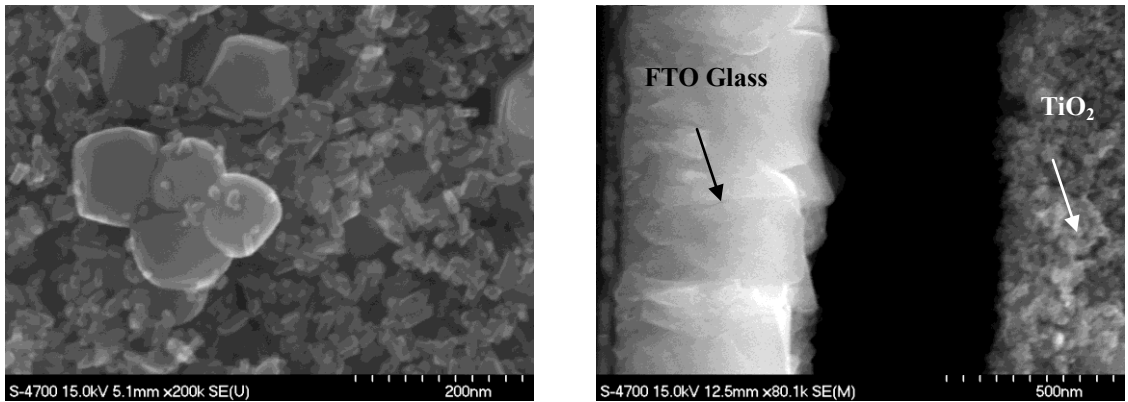


Figure 5-4 : (a) Top view of screen printed TiO_2 on FTO, (b) Cross-sectional view of screen printed TiO_2 on FTO.

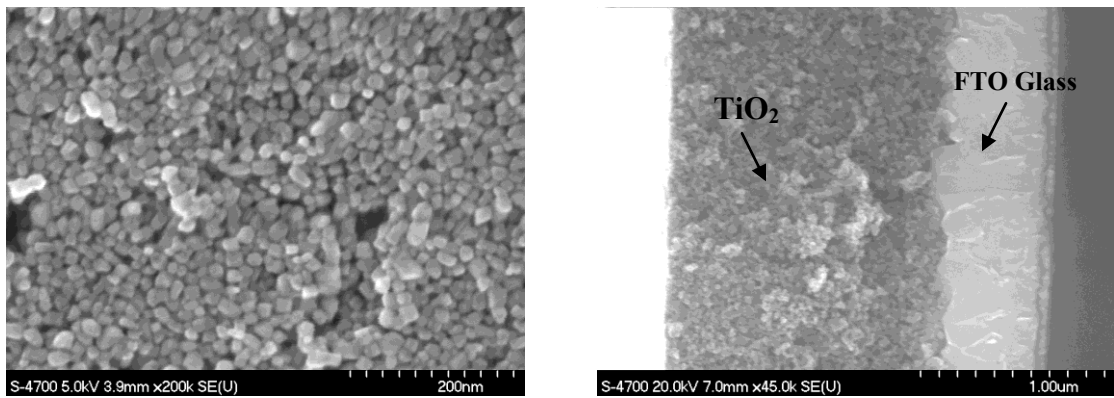


Figure 5-5: (a) Top view of spin-coated TiO_2 on FTO, (b) Cross-sectional view of spin-coated TiO_2 on FTO.

5.1.1. DSSC Testing Revisited

While measuring J-V curves, the cell area was only partially exposed (0.32 cm^2) under illumination. The testing setup has a 0.32 cm^2 aperture defining the illumination spot that was much smaller than the size of the DSSC (1 cm^2). In this case, the dark current through the unexposed area competes with the photocurrent and decreases the cell efficiency. This was corrected by fabricating cells with smaller areas (0.04 cm^2) and exposing the full cell area under illumination. Dark and illuminated J-V curves of this fully illuminated device are shown in Figure 5-6. At 1 sun, this device showed a $V_{OC} =$

0.61 V, $J_{SC} = 16.82 \text{ mA/cm}^2$, $FF = 65\%$, and an efficiency of 6.59%. Clearly, J_{SC} was increased by a factor of two as compared to the previous device.

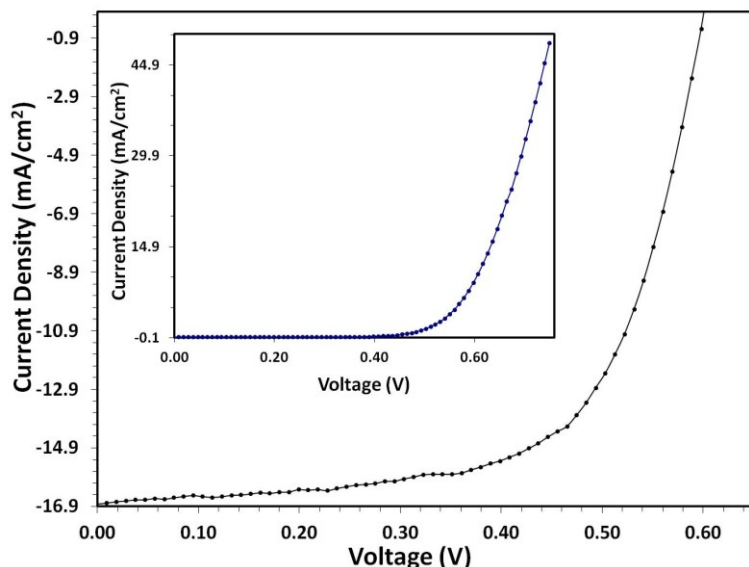


Figure 5-6: J-V curve of DSSC with fully illuminated area (0.04 cm^2) at 1 sun. Inset: dark J-V.

5.1.2. DSSCs with TiCl_4 treatment

As discussed in chapter 4.1.4, TiCl_4 treatment of the photoanode enhances the efficiency of DSSCs. Therefore, the photoanode was treated with TiCl_4 solution. Details of this treatment were already discussed in chapter 4.1.4. DSSCs were then fabricated and tested using this photoanode. Dark and illumination J-V curves under various light intensities are shown in Figure 5-7 and Figure 5-8, respectively. Metrics extracted from these curves are given in Table 5-1. At one sun, this DSSC has an efficiency of $\sim 10\%$. The results are in agreement with the literature in terms of increase in efficiency, which is mainly due to the increase in photocurrent. However, a higher J_{SC} ($\sim 25 \text{ mA/cm}^2$) and a lower V_{OC} (0.59 V) were achieved here as compared to both the DSSC without this treatment and the literature values (0.77 V) for TiCl_4 treated DSSCs. This may be due to the production of some intermediate phases of TiO_2 or the presence of HCl in the nanoporous matrix of TiO_2 even after rinsing with DI water and ethanol.

If the V_{OC} value of the present DSSC can be increased to 0.7 V, the efficiency of the DSSC would be more than 11%.

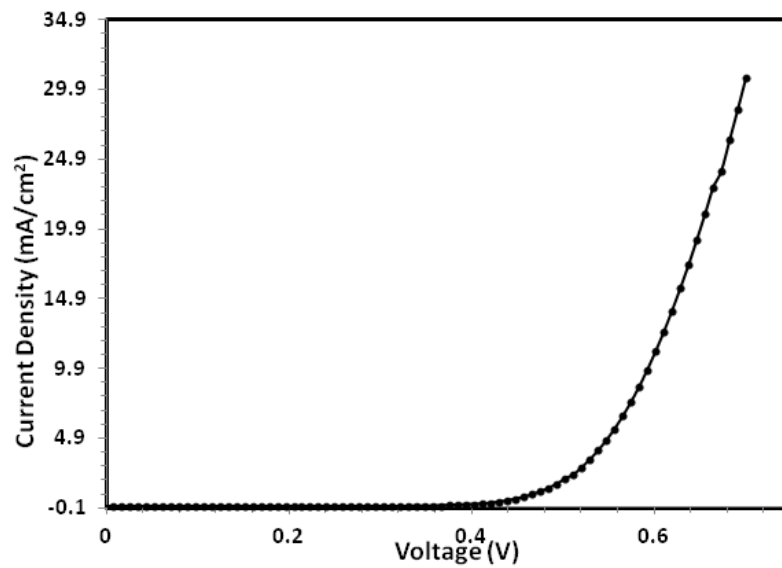


Figure 5-7: J-V curve of DSSC with TiCl₄ treatment under dark.

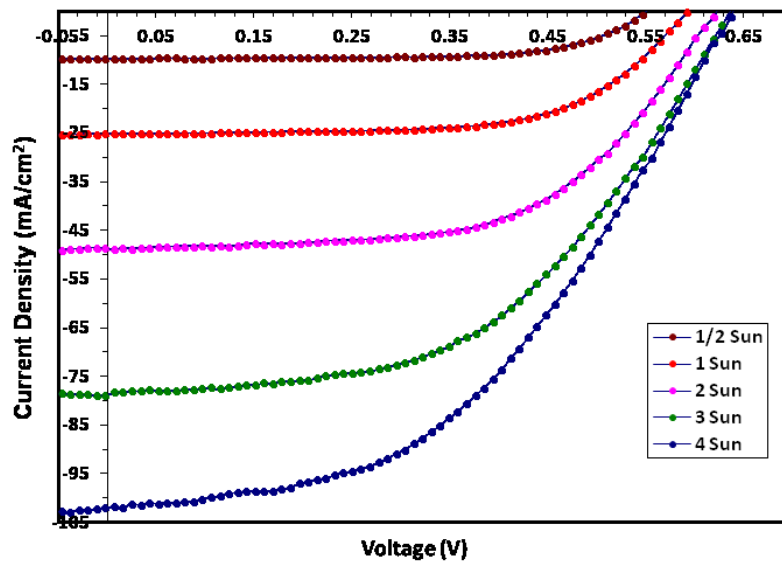


Figure 5-8: J-V curves of a 0.04 cm² DSSC with TiCl₄ treatment under various illumination intensities.

Sun	V_{OC} (V) \pm (0.005)	J_{SC} (mA/cm ²)	FF (%)	η (%)
½ Sun (50.52 mW/cm ²)	0.556	10 \pm 1	67 \pm 1	7.3 \pm 0.7
1 Sun (101.00 mW/cm ²)	0.592	25 \pm 2	63 \pm 1	10 \pm 1
2 Sun (202.00 mW/cm ²)	0.619	49 \pm 5	57 \pm 1	8.7 \pm 0.9
3 Sun (303.00 mW/cm ²)	0.628	79 \pm 8	50 \pm 1	8.4 \pm 0.8
4 Sun (404.00 mW/cm ²)	0.637	100 \pm 10	46 \pm 1	7.4 \pm 0.7

Table 5-1: Metrics extracted from J-V curves of DSSC with TiCl₄ treatment.

5.2. A NOTE ON ERROR ANALYSIS OF PERFORMANCE MEASURING PARAMETERS

Standard error analysis of measured and derived metrics was carried out. It was found that the error in the area of the cells was the dominant source of error, which was estimated at $\pm 10\%$ by measuring the dimensions of the cells under a microscope. The uncertainty in the area is largely due to the irregular edges of the cells caused by the screen printing process. V_{OC} values were determined by linear interpolation between the two measured data points closest to the axis crossing. The uncertainty in V_{OC} was conservatively estimated as ± 0.005 V, or half of the voltage step size in the data, although it is undoubtedly more precise. The uncertainty in the illumination intensity was estimated from the power meter manufacturer's specifications, as well as the observed fluctuations in the measured power of the solar simulator under operation. Calculated errors in J_{SC} and power conversion efficiency were dominated by the uncertainty in the cell area.

5.3. CNT THIN FILMS AND THICK PAPERS

In the case of SWCNTs thin films, it was found that the films were not fully detached from the filter membrane during submerging in nanopure water. Various approaches were adopted to deal with this problem. These approaches included:

- Filter membrane with SWCNT film was dried under pressure between sheets of paper. However, after drying SWCNTs film did not peel off.

- Literature reports of CNT film preparation by filtration procedures often involve dissolving the filter membrane using acetone baths. However, when using this procedure here it was found that the membrane appeared to contract upon contact with the acetone, damaging the SWCNT film. Also, the filter membrane did not dissolve completely.
- Using different filter membranes (Nalgene, 47 mm diameter, 0.22 μm pore size), again, the film did not detach completely. Another filter membrane MCE (Mixed cellulose ester, Millipore) was used and it was found that the SWCNT film was also not detached completely from this filter membrane but this filter membrane dissolved quite well in acetone.
- The MCE filter membrane was partially dissolved in an acetone bath. After refreshing the acetone bath many times, the film was collected on a FTO-coated glass in such a way that the free side of the SWCNT film was in contact with FTO. In order to pyrolyze the remaining filter membrane, this substrate was placed in a furnace at 530°C for 1 hour under argon. The argon flow rate was 15 sccm/minute. It was found that both the filter membrane and SWCNT film were consumed. Perhaps residual oxygen resulting in burning of both the membrane and the CNT film.
- We attempted pretreatment of the FTO substrate with hexamethyldisilazane (HMDS) which is well known adhesion promoter:
 - FTO was rinsed with 98% HMDS solution purchased from Fluka. The filter membrane with SWCNT film was transferred to the treated substrate in such a way that the SWCNT film was between the FTO and the filter membrane. Then, this was placed in an oven at 100°C for 1 hour while pressing under weight. It was found that the film did not stick to the FTO. This method was not pursued further.
 - FTO was soaked in 6.67% HMDS solution for 15 minutes. The filter membrane with SWCNT film was transferred to the treated substrate as above. Then, this was put in an oven at 100°C for 1 hour while pressing under weight. It was again found that the film did not stick to the FTO.

Partially detached SWCNT films were used to make counter electrodes of DSSC. Counter electrodes were made by collecting the partially detached SWCNT films on FTO. Stacks of two films and four films were put in an oven for drying. Dark and illuminated J-V curves with efficiencies of these DSSCs are given in the Figure 5-9 and Figure 5-10, respectively.

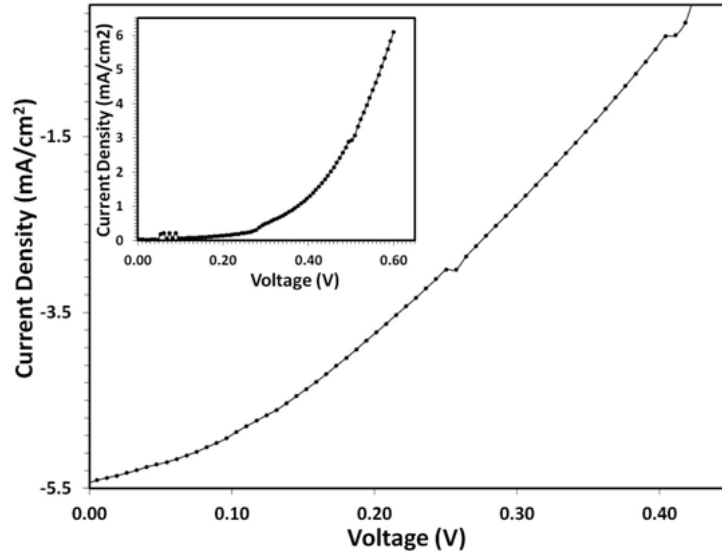


Figure 5-9: J-V curve of a DSSC with a stack of two CNT films on FTO as a counter electrode at 1 sun. Inset: dark J-V.

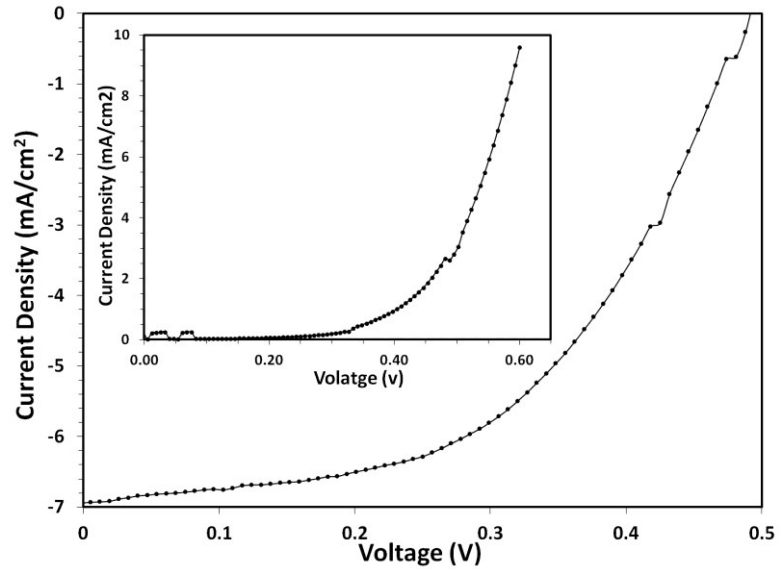


Figure 5-10: J-V curve of a DSSC with a stack of four CNT films on FTO as counter electrode at 1 sun. Inset: dark J-V.

Metrics extracted from these curves are given in Table 5-2. DSSC with stack of four films has better FF and efficiency as compared to stack of two DSSC.

In the case of thick papers, again it was found that they did not detach and peel off from the cellulose acetate filter membrane. As described above, the MCE filter membrane was dissolved in an acetone bath. Thus, these thick papers were used as counter electrodes of DSSCs. There was a chance that these thick papers might touch the TiO_2 layer and short circuit the cell; a porous electrode separator (Celgard A-117-0300M-A) was used to avoid this. Unfortunately, the separator blocked the current completely in the DSSC. Figure 5-11 shows the dark and illuminated J-V curves with the efficiency for a DSSC fabricated with a thick paper counter electrode and the above mentioned separator with a hole cut through it to allow contact of the electrolyte with the electrodes.

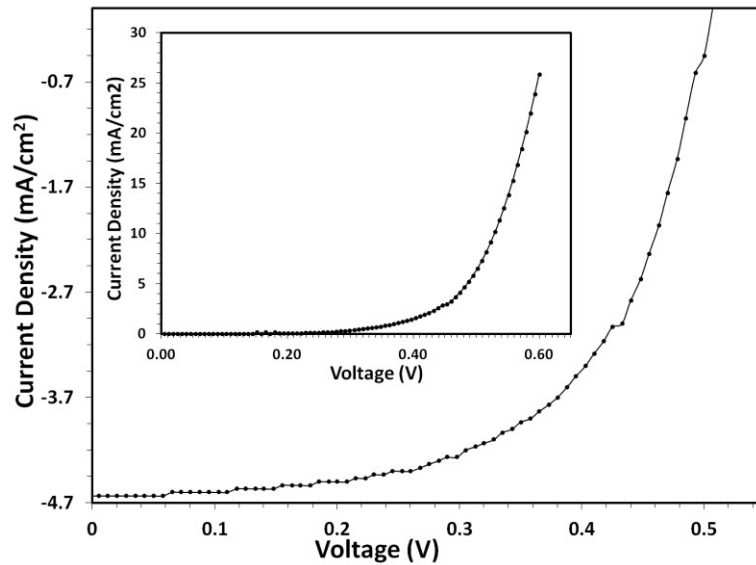


Figure 5-11: J-V curve for DSSC with thick CNT paper as a counter electrode at 1 sun.

Inset: dark J-V.

Counter Electrode	V_{OC} (V) \pm (0.005)	J_{SC} (mA/cm²)	FF (%)	η (%)
Stack of Two Films	0.425	5.4 \pm 0.5	33 \pm 1	0.8 \pm 0.1
Stack of Four Films	0.488	6.9 \pm 0.7	51 \pm 1	1.8 \pm 0.2
Thick paper	0.500	4.6 \pm 0.5	60 \pm 1	1.4 \pm 0.1

Table 5-2: Efficiencies of DSSCs with stacks of two, four CNT films and thick paper counter electrodes.

5.4. CONCLUSIONS

Standard DSSCs were successfully optimized to achieve reproducible efficiencies ~10%. Issues were found in CNT thin films and thick paper regarding their detachment from filter paper. This CNT film/paper work was not pursued further.

CHAPTER 6 APPLICATION OF CVD CNTs IN DSSCs

This chapter deals with the results and discussion regarding applications of CNTs in counter electrode of DSSC as an alternative to Pt.

6.1. INTRODUCTION

Several strategies to incorporate CNTs into DSSCs have been investigated, including spray-coating the electrode with a suspension of CNTs in solvent^{167,168} and deposition of a CNT-containing paste^{169,170} or slurry.¹⁷¹ Another approach involves CNTs grown on other substrates and subsequently transferred to a transparent conducting oxide (TCO) coated substrate, typically, fluorine-doped tin oxide (FTO) on glass. In this regard, Dong et al. achieved 5.5% efficiency using VASWCNTs that are transferred to FTO after growing on a Si substrate.¹⁷² In 2012, Hao et al. achieved 5.25% efficiency with VASWCNTs counter electrodes in which CNTs were similarly grown on Si and then transferred to FTO.¹⁷³ These approaches have some limitations such as poor availability of catalytic surface area, and poor electron transport due to contact resistance. Vertically aligned carbon nanotubes (VACNTs) directly grown on substrates are one approach to overcoming these issues. So far, few studies have been done in which CNTs are directly grown on FTO substrates using chemical vapour deposition methods. In 2010, Sayer et al. achieved 0.77% efficiency by using a directly grown MWCNT counter electrode.¹⁷⁴ In 2011, an efficiency of around 6% was achieved using VACNTs directly grown on a graphene substrate.¹⁷⁵ A detailed comparison of these works is given in Table 6-1. Extensive effort is needed to study CNTs directly grown on various substrates, and to optimize the growth conditions for CVD methods.

CNTs	Method	Dye	Electrolyte	η (%)	Ref.
VASWCNTs	WA-CVD	N719	I/I ₃ ⁻	5.5	172
VASWCNTs	WA-CVD	N719	T ₂ /T ⁻	5.25	173
MWCNTs	MW plasma CVD	Anthocyanin	I/I ₃ ⁻	0.77	174
VACNTs	WA-CVD	N719	I/I ₃ ⁻	6.0	175

Table 6-1: Comparison of DSSCs with VACNTs CE already available in literature.

6.2. CNTs GROWTH (VARIOUS SYNTHESIS METHODS ON VARIOUS SUBSTRATES)

With the aim to develop CNT growth expertise, we initially focused on well-known substrates for CNT growth, such as SiO₂ passivated Si. Iron was used as a catalyst, deposited using sputtering and electron beam methods. CVD method 1 (NH₃-C₂H₄) was used as discussed in chapter 4.2.3.1. Experimental methods were as in chapter 4.2.3 except where otherwise stated. Following CVD, there was a visible film of black material on the SiO₂/Si substrate; VACNTs were obtained for both Fe deposition methods and are shown in Figure 6-1 (a-d).

After successful growth of VACNTs on SiO₂/Si, CNT growth was attempted on FTO using the above CVD method 1, but was unsuccessful. FTO could not withstand the high growth temperature of 750°C. Therefore, a low growth temperature suitable for FTO was attempted. For this purpose, CNTs were grown on various substrates (FTO, Quartz, Stainless Steel (316) and Aluminum Alloy (6061)) at different growth temperatures (500°C-580°C) with Invar 426 alloy (42% Ni, 52% Fe and 6% CO, w/w/w) catalyst using CVD method 2 discussed in chapter 4.2.3.2. SEM top views of CNTs grown on these substrates at low temperature (580°C) are shown in Figure 6-2 (a-d). The CNTs viewed from the top appear tangled and randomly oriented. There is also a variation in their diameters. In Figure 6-2 (b), CNTs were grown directly on a stainless steel (SS) substrate without depositing any catalyst as the iron and nickel content of SS was thought to be sufficient to catalyze CNT growth.

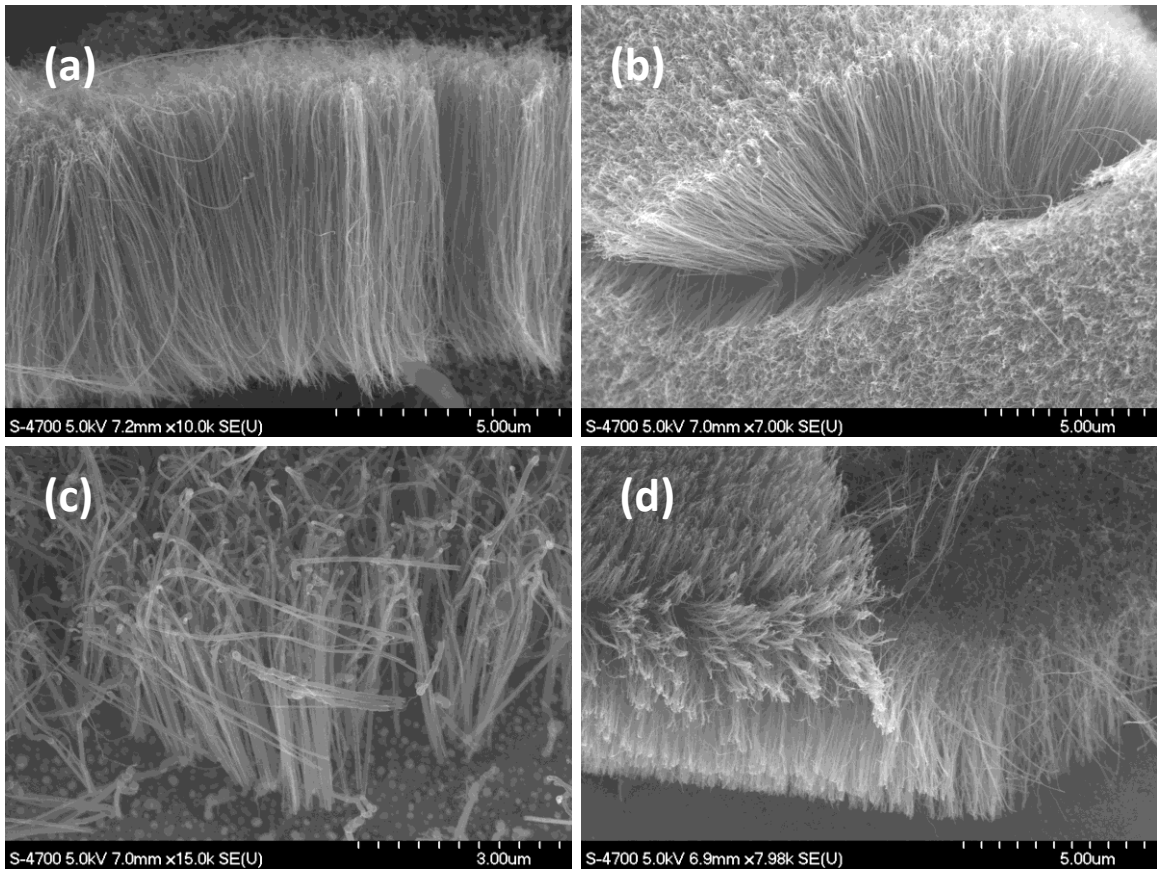


Figure 6-1: SEM of VACNTs grown with CVD method with electron beam evaporation deposited (a, b) and sputtered (c, d) Fe samples.

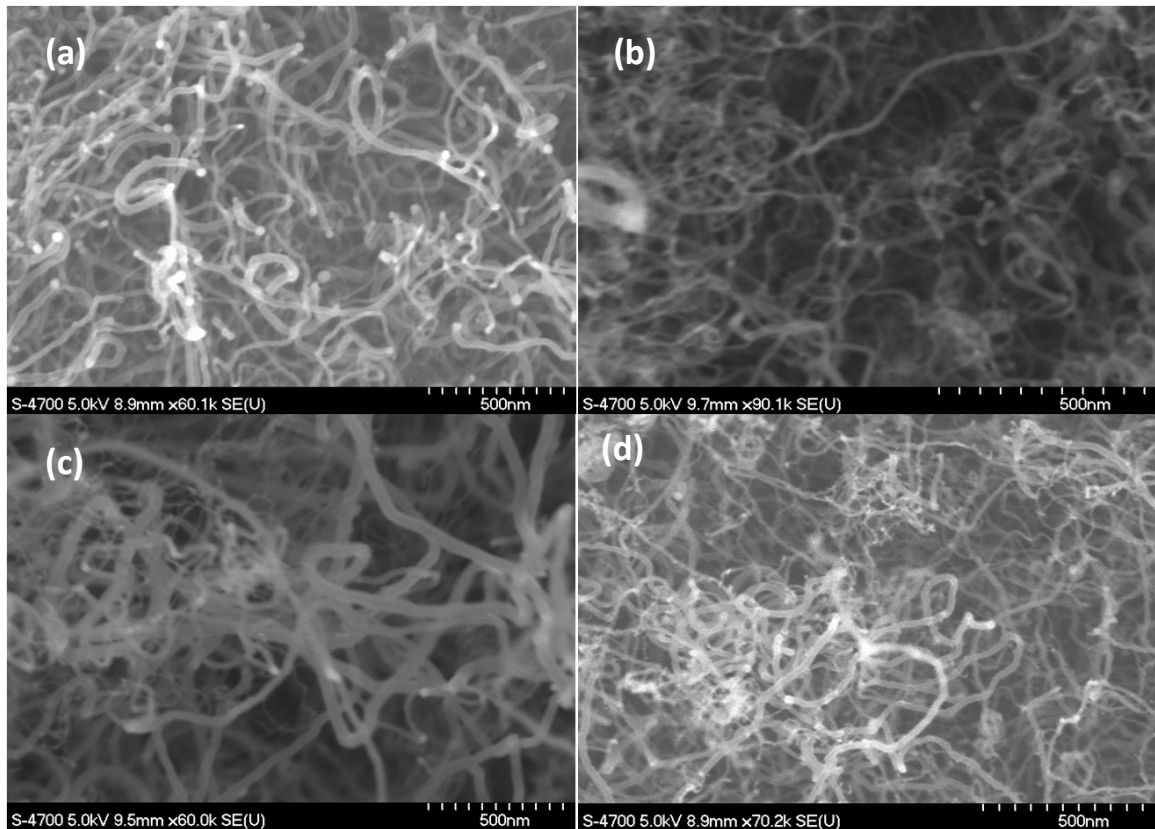


Figure 6-2: SEM of CNTs grown at 580°C on a) Aluminum Alloy/Cr/Invar; b) Directly on SS; c) SS/Invar; d) Quartz/Cr/Invar.

When we applied these growth conditions to grow CNTs on FTO, we were still not successful.

After several unsuccessful trials, a systematic investigation was undertaken. For this purpose, three well known CVD recipes for growing CNTs were applied on FTO glass in the absence of catalysts, to evaluate the impact of growth conditions on FTO:

1. Water assisted CVD method (WA-CVD)
2. CVD method with MeOH (MeOH-CVD)
3. CVD method with ammonia and ethylene gases ($\text{NH}_3\text{-C}_2\text{H}_4$ -CVD)

These methods are discussed in detail in chapter 4.2.3.

We examined the FTO, before and after exposure to growth conditions, and results are discussed as follows.

Before exposure to CNT growth conditions, the FTO glass had a sheet resistance and optical transmission close to the values provided by the manufacturer, i.e., 15 Ohms/square and 80%, respectively. A SEM micrograph of as-received FTO, Figure 6-3 (a), showed an interconnected multicrystalline structure with a 100-200 nm grain size. After exposure, isolated islands with size distributions in the range of 100 nm-10 μm were observed for all samples (Figure 6-3(b-d)).

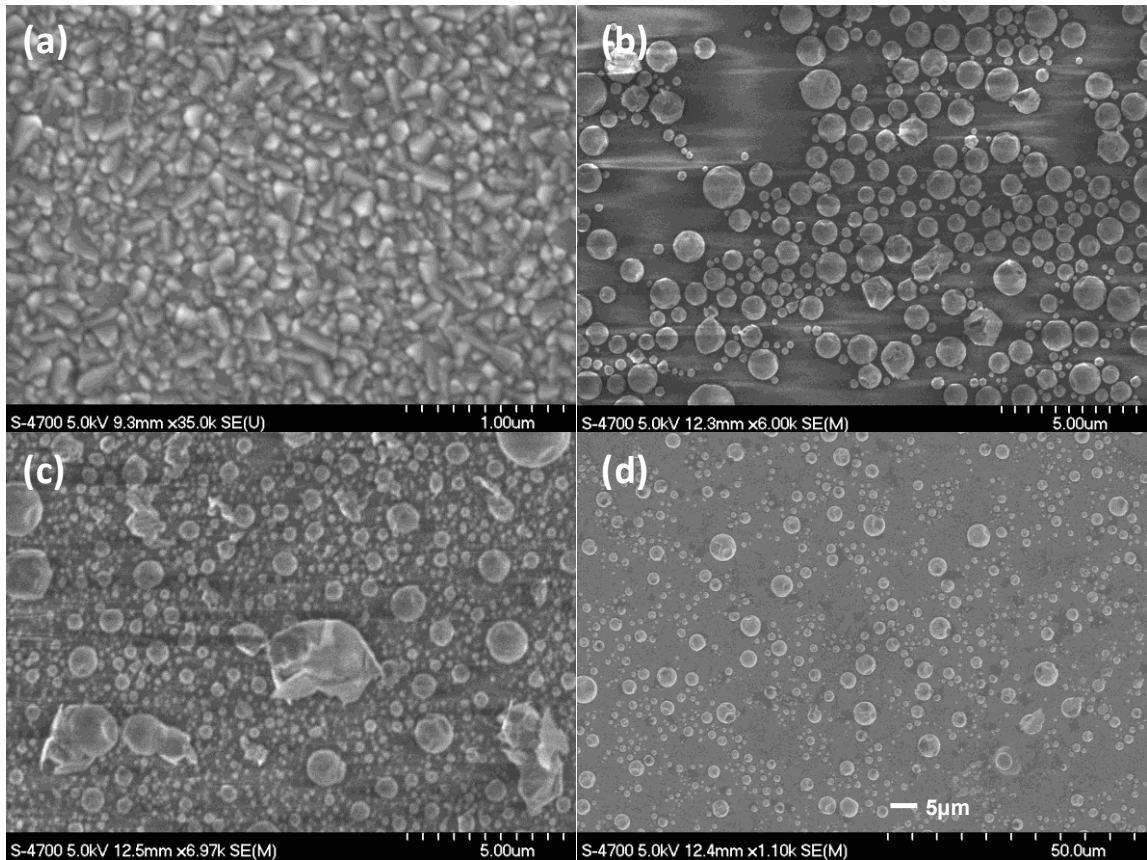


Figure 6-3: SEM of (a) As-received FTO, post-exposure to: (b) WA growth conditions, (c) MeOH growth conditions, (d) $\text{NH}_3\text{-C}_2\text{H}_4$ growth conditions.

We proposed that during exposure to NH_3 or H_2 at elevated temperatures, the oxide is reduced to metallic tin, which de-wets the surface leaving these isolated islands on the

glass substrate (see XPS results in following section). Following growth conditions and further exposure to air, this metallic tin oxidized to form SnO_x , possibly a mixture of SnO and SnO_2 .

The above interpretation was also supported with the fact that during X-ray photoelectron spectroscopy (XPS) measurements of these samples, charging was observed due to the low conductivity of these samples. The energy scales of the spectra were shifted due to this charging phenomenon and were corrected to align the binding energies of the adventitious carbon C 1s peak.

In each case, two key observations were made: Firstly, after exposure to growth conditions, all three samples showed strong intensity from the Si 2s and 2p core levels, at binding energies ~ 155 and ~ 103 eV, respectively, due to the exposed glass substrate. No Si peaks were observed for as-received FTO glass substrates. Secondly, F 1s emission, observed on as-received FTO glass, was completely absent after exposure to growth conditions, indicating a loss of the dopant from the conducting oxide. FTO coated glass was therefore deemed unsuitable as a substrate for VACNTs growth. A summary of these results is provided in Figure 6-4. A much higher C 1s peak was found for the $\text{NH}_3\text{-C}_2\text{H}_4$ sample, indicating a higher concentration of carbon on this surface, possibly due to the deposition of carbonaceous materials during growth procedure. Due to the surface carbon layer, the intensity of all Sn, Si and O features associated with the substrate were significantly attenuated compared with other samples.

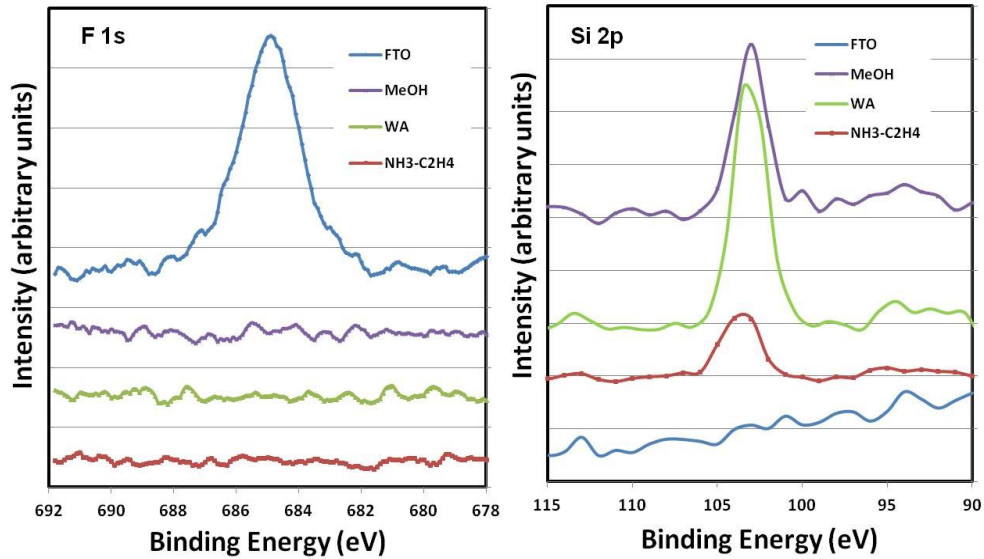


Figure 6-4: The XPS – F 1s signal is completely absent following exposure to growth conditions (left), indicating a loss of the dopant from the conducting oxide. The appearance of the Si 2p peak following exposure indicates de-wetting of the SnO_x revealing the glass substrate beneath the FTO (right), consistent with interpretation of the SEM results.

Figure 6-5 shows the optical transmission spectra of unexposed and exposed FTO samples. As-received FTO has a maximum of 80% optical transmission, whereas exposed FTO samples exhibit 20%-30% transmission. The samples no longer appear transparent, but rather translucent, indicating strong scattering of the incident light.

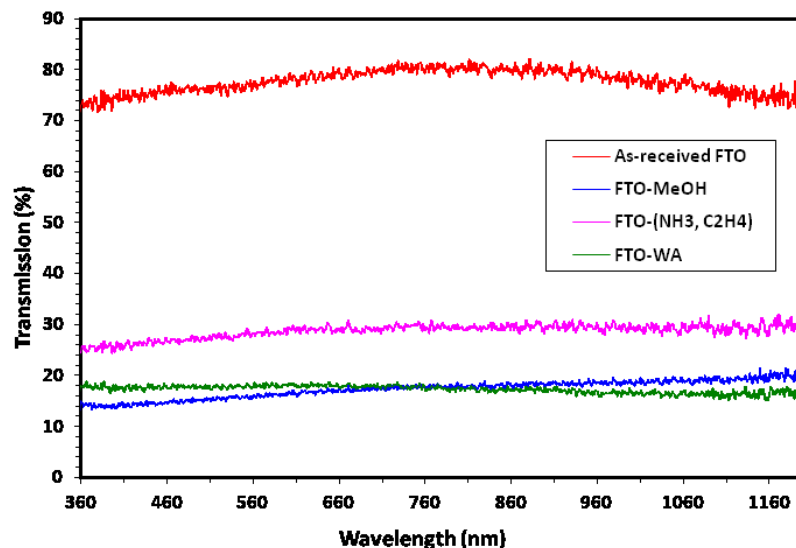


Figure 6-5: UV-vis spectra of as-received and post-exposure FTO.

Sheet resistances of these samples were also measured using four-probe method. As-received FTO has the sheet resistance 15 Ohms/square while the exposed samples of FTO are no longer conducting. The measurement of the sheet resistance was limited by the input impedance of the meter. This observed high resistance was due to the loss of a continuous conduction path in the plane of the surface of FTO glass substrate as discussed already. Therefore, having the above experimental evidence, we proposed that FTO is not a suitable substrate for direct growth of CNTs.

6.3. DSSCs WITH CNT COUNTER ELECTRODES BY THE MEOH CVD METHOD

CNTs were grown directly on Quartz/Cr (65 nm)/invar (6.5 nm) substrate using the MeOH CVD method 3 discussed in chapter 4.2.3.3; these CNTs were used as catalyst in counter electrodes for DSSCs. Photoanodes were fabricated following the procedure explained in chapter 4.1.4, including blocking layer of TiO₂ but without TiCl₄ treatment. After sealing, DSSCs were tested using the standard conditions described in chapter 2.5.5. J-V curves under dark and various illumination intensities are shown in Figure 6-6 and Figure 6-7, respectively, and metrics extracted from these curves are shown in Table

6-2. At 1 sun, an efficiency of 3.7% was achieved. V_{OC} and J_{SC} increase whereas fill factor decreases with increasing illumination intensity due to IR^2 losses.

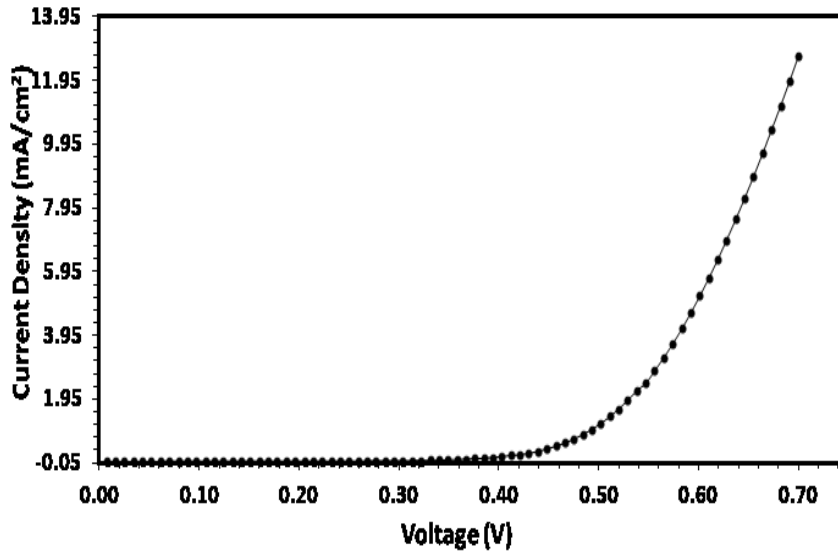


Figure 6-6: DSSC with CNT CE grown with the MeOH-CVD in the dark without $TiCl_4$ treatment.

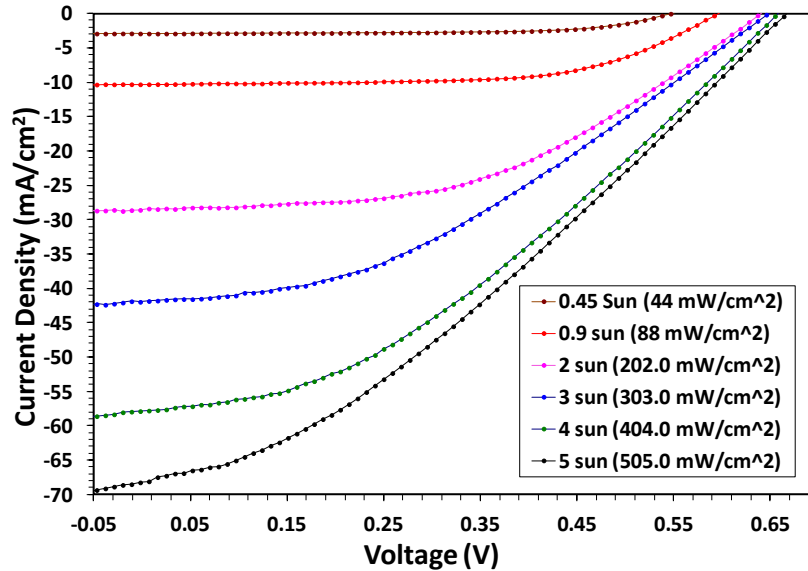


Figure 6-7: DSSC with CNT CE grown with the MeOH-CVD under various light intensities, without $TiCl_4$ treatment.

Sun	V_{OC} (V) ± 0.005	J_{SC} (mA/cm ²)	FF (%)	η (%)
0.45 Sun (44 mW/cm ²)	0.547	2.9 \pm 0.3	64 \pm 1	2.1 \pm 0.2
0.9 Sun (88 mW/cm ²)	0.601	10 \pm 1 (12*)	60 \pm 1	3.7 \pm 0.4
2 Sun (202.0 mW/cm ²)	0.637	29 \pm 3	47 \pm 1	4.3 \pm 0.4
3 Sun (303.0 mW/cm ²)	0.646	42 \pm 4	38 \pm 1	3.4 \pm 0.3
4 Sun (404.0 mW/cm ²)	0.655	58 \pm 6	36 \pm 1	3.4 \pm 0.3
5 Sun (505.0 mW/cm ²)	0.664	68 \pm 7	33 \pm 1	2.9 \pm 0.3

Table 6-2: Metrics extracted from DSSC with CNT CE grown with MeOH-CVD under various light intensities without TiCl₄ treatment. *At 1 sun, the current densities have been scaled linearly to 1 sun (101.0 mW/cm²) as the data were mistakenly collected at 88 mW/cm². Note that in this regime the photocurrent varies linearly with illumination.

6.4. GROWTH OF CNTs USING THE WATER ASSISTED METHOD (WA-CVD)

6.4.1. Synthesis

Finally, the WA-CVD method was used to grow MW-VACNTs on stainless steel (316) substrates. Details of the growth procedure were presented in chapter 4. MW-VACNTs were grown at different exposure times of ethylene gas, i.e., 20 s, 40 s, 80 s and 160 s.

6.4.2. Characterization

6.4.2.1. Scanning electron microscopy (SEM)

In order to determine the growth rate (length/time), we characterized these MW-VACNTs using SEM. The length of each sample was measured from the resulting micrographs (Figure 6-9 (a-d)) and plotted versus exposure time as shown in Figure 6-8. A growth rate of 0.9 μ m/s was found from the slope of the plot.

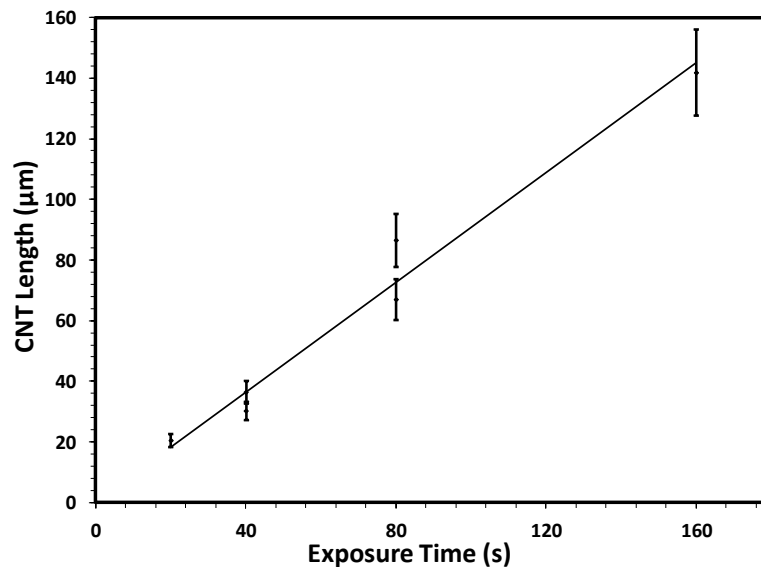


Figure 6-8: Growth of MW-VACNTs (exposure time versus CNT length). Each data point represents the average of 5 samples.

6.4.3. DSSC fabrication and characterization

Counter electrodes of MW-VACNTS were prepared using 10 s, 20 s, 40 s and 60 s growth exposures on SS substrates using the WA-CVD method 4 described in chapter 4.2.3.4. Photoanodes were prepared using the procedure described in chapter 4.1, including the spin-coated TiO₂ blocking layer, but without TiCl₄ treatment.

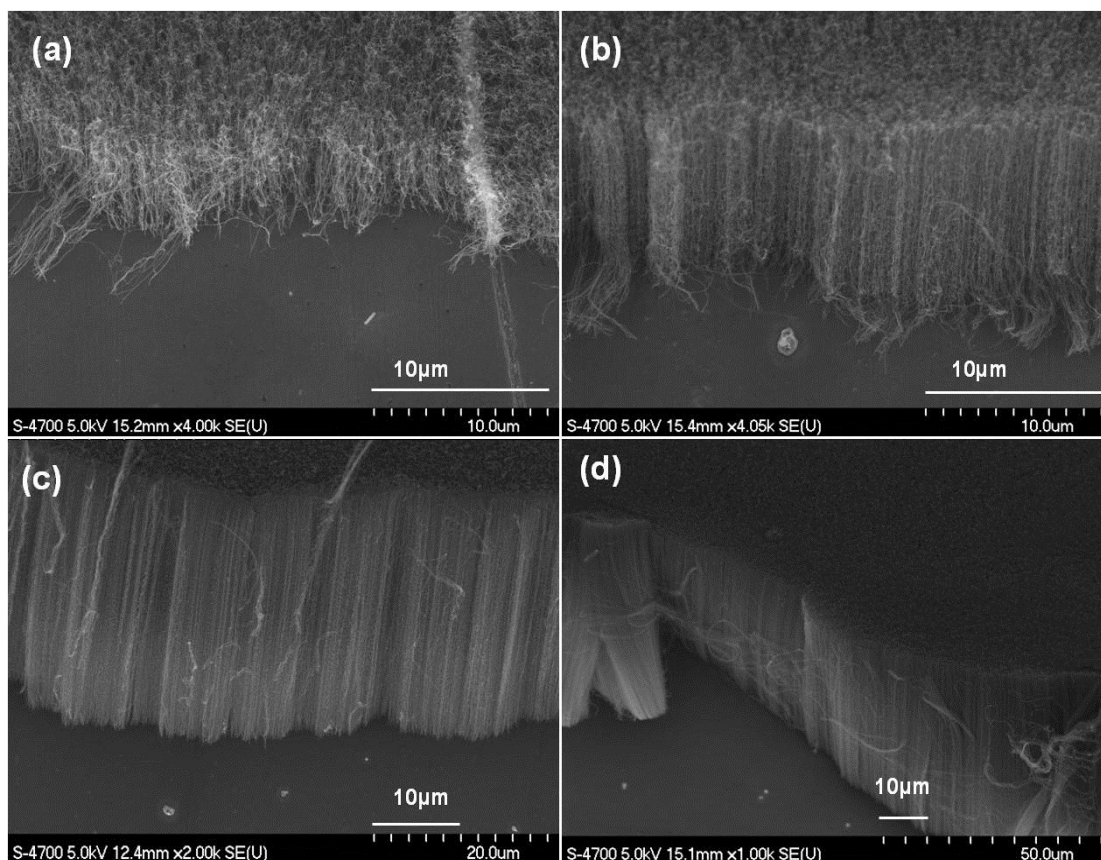


Figure 6-9: Growth of MW-VACNTs on SS with different exposure times a) 10 s b) 20 s c) 40 s and d) 60 s.

6.4.3.1. Current density-voltage measurements (J-V curves)

After fabrication of DSSCs using these CEs, J-V curves under dark and illumination were measured. In the dark, all devices show similar dark currents (at $V < 450$ mV), regardless of the exposure time of ethylene, see Figure 6-10. However, dark current increased with increasing exposure time at high forward bias ($V > 450$ mV). This is accounted for the catalytic activity of the VA-MWCNT counter electrodes. In the dark under forward bias, electrons enter the cell through the photoanode reducing I_3^- to I^- , whereas oxidation of I^- takes place at the counter electrode. For short length VA-MWCNTs, the rate of oxidation of I^- is slow as compared to long VA-MWCNTs, limiting the J-V slopes at voltages > 450 mV.

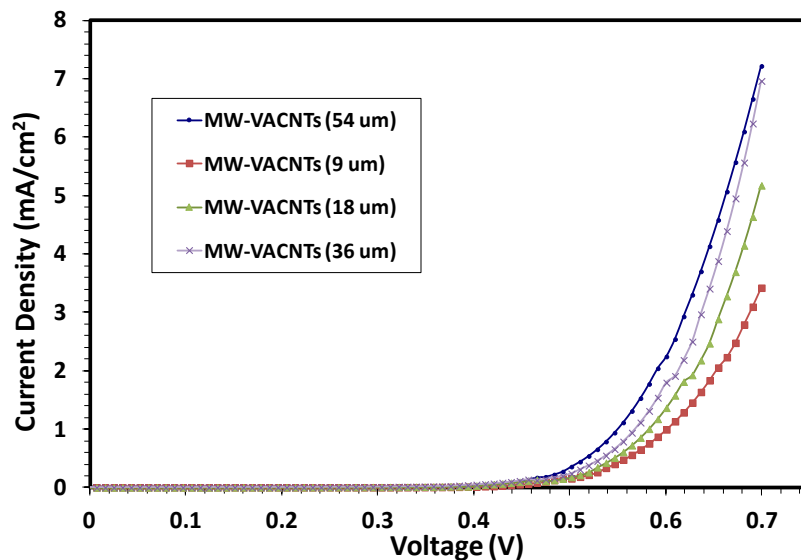


Figure 6-10: Dark J-V curves of DSSCs with MW-VACNTs counter electrodes.

J-V curves under 1 sun illumination are shown in Figure 6-11. Performance determining metrics are extracted from the J-V curves and are shown in Table 6-3. Under illumination, CE with 36 μm length MW-VACNTs had the best performance with respect to each parameter, e.g., $\eta = 5.7\%$, $\sim 86\%$ efficient of that of a similar DSSC with Pt counter electrode.

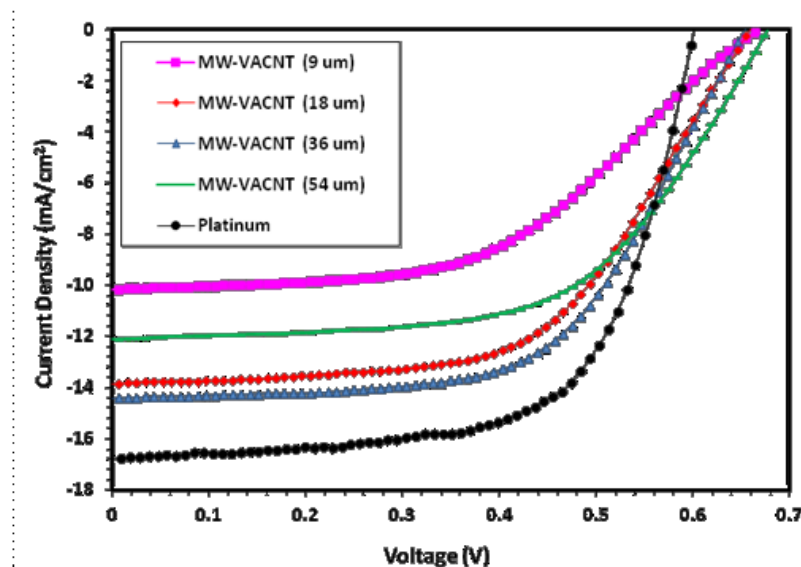


Figure 6-11: J-V curves of DSSCs with MW-VACNTs and Pt CEs under 1 sun.

Specific series resistance was estimated from the slope of the J–V curve around Voc. Its value is less ($15.6\pm 1.6 \text{ Ohms}\cdot\text{cm}^2$) for a 36 μm length MW-VACNTs as compared to other samples. Voc values of all MW-VACNTs DSSCs are similar but higher as compared to Pt-based DSSC.

CNTs Length (μm)	Voc (V) ± 0.005	Jsc (mA/cm^2)	FF (%)	η (%)	Rs under Illumination ($\Omega\cdot\text{cm}^2$)
9	0.664	10 \pm 1	50 \pm 1	3.4 \pm 0.3	26.5 \pm 2.7
18	0.655	13.9 \pm 1.4	57 \pm 1	5.2 \pm 0.5	17.0 \pm 1.7
36	0.646	14.4 \pm 1.4	60 \pm 1	5.7 \pm 0.6	15.6 \pm 1.6
54	0.673	12.1 \pm 1.2	54 \pm 1	4.4 \pm 0.4	19.5 \pm 1.9
Pt	0.592	16.8 \pm 1.7	66 \pm 1	6.6 \pm 0.7	6.3 \pm 0.6

Table 6-3: Metrics extracted from J-V curves of DSSCs with MW-VACNTs and Pt CEs under 1 sun illumination.

6.4.3.2. Electrochemical impedance spectroscopy (EIS)

In order to understand this cause of decrease in efficiency, EIS measurements were taken in the dark. In this case, the MW-VACNT electrode was taken as the working electrode (WE) and Pt was used as both the CE and reference electrode (RE), resulting in two terminal electrochemical cells. EIS plots and equivalent circuits to fit these plots using *z-view* are shown in Figure 6-12 and Figure 6-13, respectively. A parallel combination of a charge transfer resistance (R_{CT}) and a non-ideal capacitance (constant phase element: CPE) was used to model each electrode/electrolyte interface. The Pt–MW-VACNT cell exhibits the superposition of two semicircles in the complex-*z* plane: the smaller circle for smaller Re (*z*) corresponds to the Pt/electrolyte interface, and the larger circle for larger Re (*z*) corresponds to the MW-VACNT/electrolyte interface. The diameter of semicircles, related to the R_{CT} of these MW-VACNT electrodes, became smaller as the length (*l*) increased up to 36 μm and then increased for longer CNTs. This indicates that the charge transfer resistance was minimized at $l = 36 \mu\text{m}$. Any variation in the reduction of triiodide to iodide at the MW-VACNT electrode affects the oxidation of iodide at the

Pt electrode. In other words, variation in the R_{CT} at MW-VACNT/electrolyte interface affects R_{CT} of Pt/electrolyte interface which also affects the capacitance. This variation for Pt electrode can be seen in Figure 6-14 in which higher frequency region is made enlarged. It is noted that this variation is not systematic but rather random. It is most likely due to unintended variability in the fabrication of these electrochemical cells.

Capacitance versus length measurements are also plotted, see Figure 6-15. The maximum capacitance was obtained for 36 μm MW-VACNTs; this capacitance is related to the surface area of the electrode. Therefore, electrodes with 36 μm MW-VACNTs have a higher effective surface area as compared to the rest of the samples.

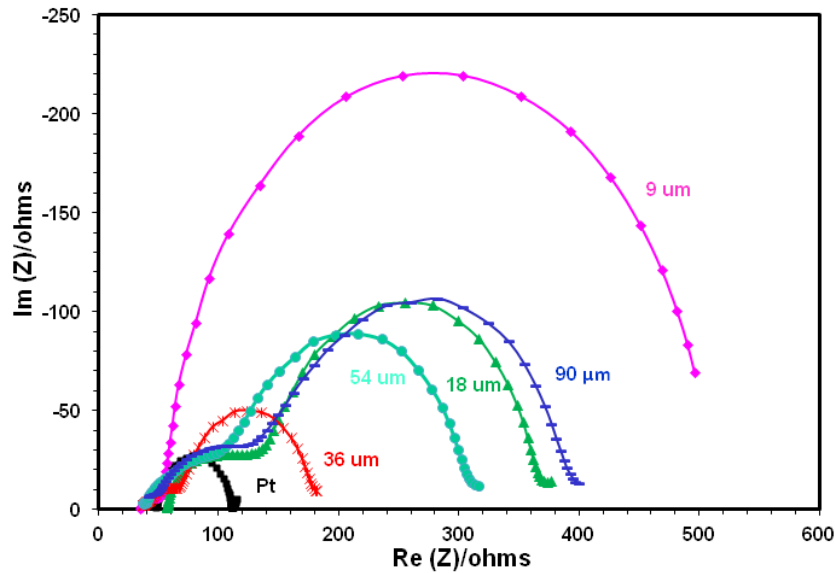


Figure 6-12: Electrochemical impedance spectroscopy of Pt–Pt and MW-VACNT–Pt. cells in dark (measured data).

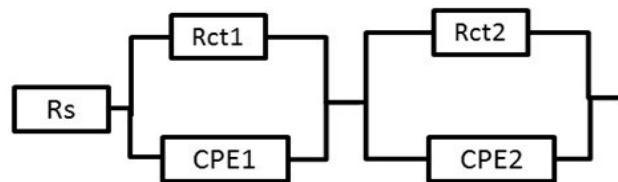


Figure 6-13: Equivalent circuit used to fit EIS plots for MW-VACNT-Pt cells.

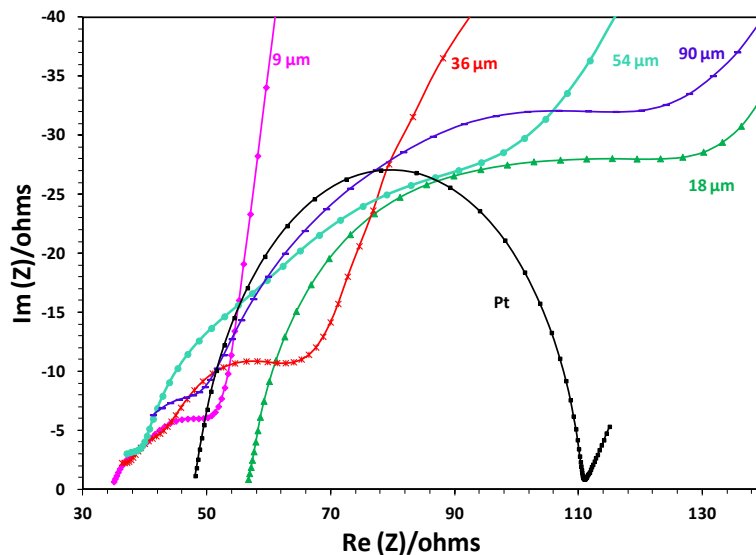


Figure 6-14: An enlargement of the high frequency side of the above EIS spectra.

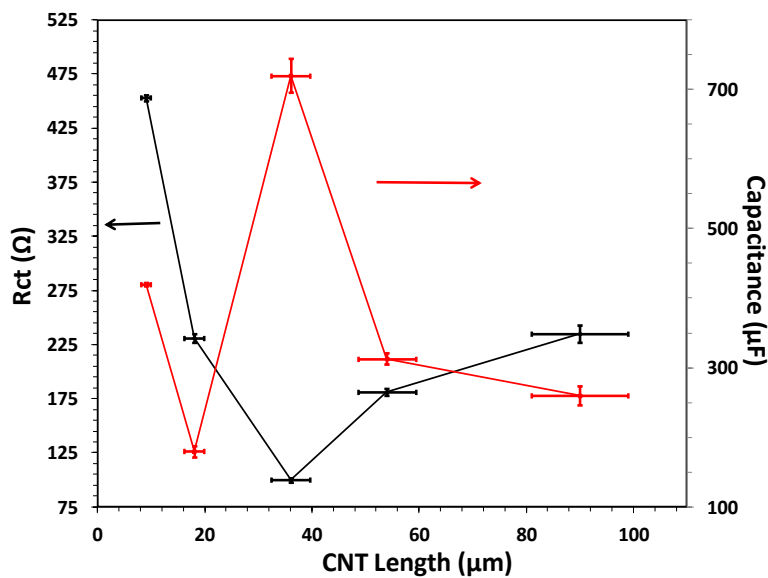


Figure 6-15: R_{CT} and capacitance of MW-VACNT/electrolyte interface –Pt as a function of CNT length from EIS of two terminal electrochemical cells characterized in the dark.

6.4.3.3. Cyclic voltammetry (CV)

Cyclic voltammetry was also done for these electrochemical cells in the dark, see Figure 6-16. The cyclic voltammograms clearly indicate that the magnitudes of over-potentials needed to reach the peak reduction and oxidation currents are minimum for the 36 μm

long MW-VACNTs as compared to the rest of the samples. Therefore, 36 μm long MW-VACNTs electrochemical cells have shown higher electrocatalytic activity.

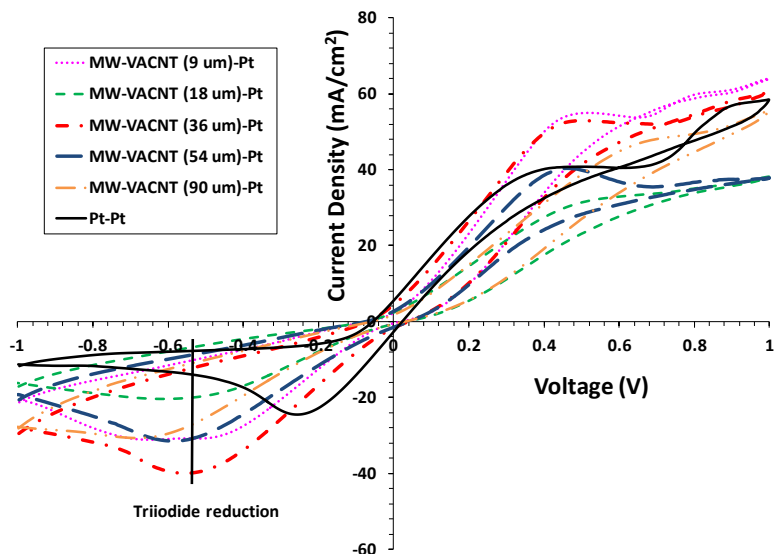


Figure 6-16: Cyclic voltammograms of MW-VACNT-Pt cells with varying CNT lengths in the dark.

6.4.3.4. Small angle X-ray scattering (SAXS)

From EIS measurements, we found that 36 μm long CNTs have the highest effective surface area. To further investigate the cause of this high effective surface area of 36 μm long CNTs, SAXS was performed. MW-VACNTs with various lengths were grown on Cu foil (5 μm in thickness). For SAXS measurements, Cu foil (5 μm) was used as substrate because X-rays attenuate relatively less with Cu as compared to Fe, Ni and Cr, which are the main constituents of stainless steel. SAXS plots are shown in Figure 6-17. It was found that with increasing length, the mean radius of CNTs decreased (see Figure 6-18). In other words, the CNTs taper with increasing length. This may be related to the increase in surface area of the CNTs.

Effectively, the electrolyte is only penetrating the top portion of the nanotube forest. It could also be the case that ion transport cannot reach the entire length of the nanotubes.

Therefore, there is some effective layer of electrolyte on top which is contributing to charge transfer. When CNTs are shorter than this effective distance, then the entire CNTs are in that effective region. As the CNT length increases, the surface area increases, the R_{CT} goes down and the capacitance goes up. When the CNTs are longer than that effective region and if the CNTs were to stay exactly same, R_{CT} and capacitance would stay constant. However, our SAXS measurements show that as the CNTs get longer, their radii become smaller. As the bottom of CNT is already grown, the number of tubes per unit area stays constant, so the radius of the entire tube does not change. We proposed that tapering is happening and therefore only their top surface area gets smaller. As CNTs get longer, the penetration depth stays the same but their radii at the top get smaller. For this reason, the overall area goes down, R_{CT} goes up and the capacitance goes down. In other words, as the CNTs initially get longer, R_{CT} decreases and the capacitance increases. Upon reaching the point where the CNTs are longer than the effective region, the surface area again decreases as the tube diameters decrease, making R_{CT} higher and the capacitance smaller. Thus, an optimum CNT length exists that minimizes R_{CT} and the best results are from CNTs having the largest surface area within this effective distance.

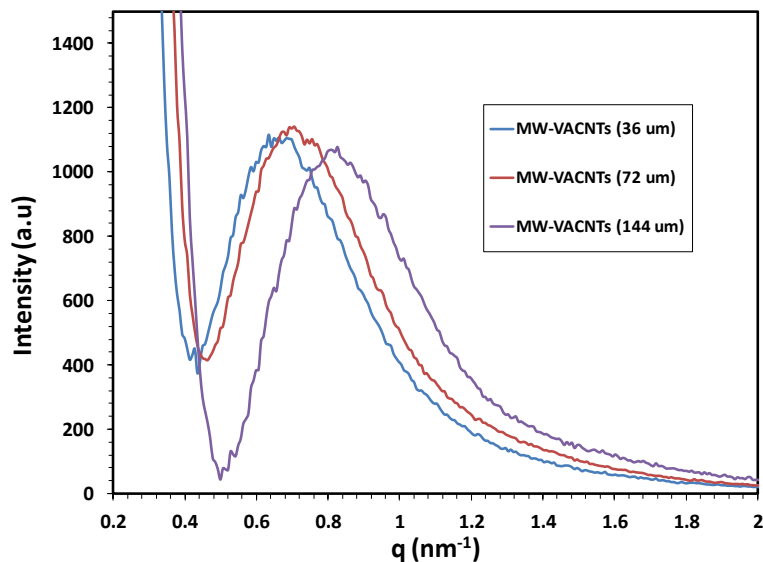


Figure 6-17: SAXS of MW-VACNTs with different lengths grown on Cu foil (5 μm).

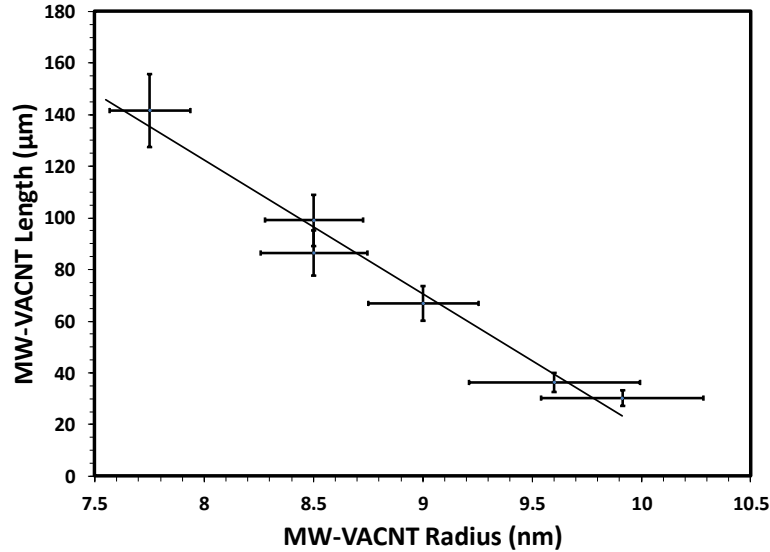


Figure 6-18: Effect of MW-VACNTs length on radius extracted from SAXS data.

6.4.3.5. Electrical transport measurements using Hg drop method

Electrical transport measurements were made on MW-VACNT/ Al_2O_3 /stainless steel electrodes and bare Al_2O_3 /stainless steel substrates using a Hg drop electrode in contact with the top surface of each sample. Conduction through the MW-VACNT/ Al_2O_3 to the stainless steel substrate was found to be Ohmic, with a specific resistance much less than the series resistance present in the DSSCs. Conduction through the bare Al_2O_3 was found to be exponential in voltage, consistent with electron tunneling through the oxide, with a differential resistance (at zero volts) larger in magnitude than that of the MW-VACNT/ Al_2O_3 samples. This indicates that the current does not actually pass through the Al_2O_3 , but most likely through pinholes that allow direct contact between the MW-VACNT forest and the substrate.

6.4.3.6. Thermal gravimetric analysis (TGA)

Thermal stability of MW-VACNTs was studied using TGA. TGA and DTG plots of MW-VACNTs are shown in Figure 6-19. MW-VACNTs lost all their mass at 674°C but still 1% residue is left behind, which is most probably iron catalyst.

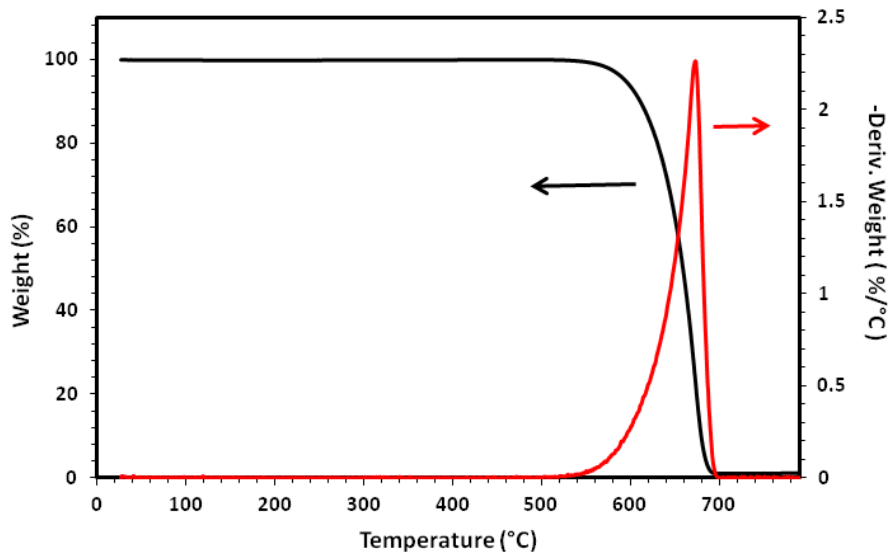


Figure 6-19: TGA and DTG plots of MW-VACNTs grown with WA-CVD.

6.5. CONCLUSIONS

XPS and electrical studies showed that FTO-coated glass is not a suitable substrate for direct growth of MW-VACNTs. In the presence of the process gases at elevated temperatures, the fluorine is leached from the FTO, and the tin oxide is reduced to tin metal, which de-wets from the surface, leaving isolated islands of tin coated with native oxide. Inexpensive substrates including aluminum and stainless steel can be used as substrates for CNT growth. DSSCs have been demonstrated with comparable metrics to those constructed using a traditional Pt counter electrode. Length versus exposure time studies showed that growth rate of MW-VACNTs was $\sim 0.9 \mu\text{m}/\text{sec}$ for WA-CVD method. J-V, EIS, CV and SAXS measurements showed that MW-VACNTs with a $36 \mu\text{m}$ length gave good overall performance i.e., $\sim 86\%$ as efficient as Pt-based DSSCs. SAXS measurements showed that with increasing growth time, the radius of MW-VACNTs decreased. Although the series resistance and short-circuit current density of the CNT cell was slightly inferior as compared to Pt-based DSSCs, improving the growth conditions and functionalization of the nanotubes to optimize cell efficiency are promising routes to producing Pt-free DSSCs that do not sacrifice efficiency.

CHAPTER 7 APPLICATION OF CARBON

DERIVED FROM NCC IN DSSCs

In this chapter, application of carbon derived from pyrolysis of nanocrystalline cellulose (NCC) as the counter electrode of DSSCs is discussed. The effect of pyrolysis on the conductivities of the substrates is also discussed. Finally, characterization of these carbon films and performance of DSSCs fabricated is also discussed.

7.1. INTRODUCTION

Nanocrystalline cellulose (NCC) is an emerging nanomaterial that has been studied extensively since its discovery¹⁷⁶ due to its easy availability, low-cost, renewability, non-toxicity and unique optical properties.¹⁷⁷ It has been used in many diverse applications such as nanocomposite films¹⁷⁸, drug delivery¹⁷⁹, and lithium battery products.¹⁸⁰ It has recently been demonstrated as a substrate for “recyclable” organic solar cells.¹⁸¹

7.2. CHARACTERIZATION OF NCC FILMS AND DSSCs

Many substrates were investigated, including fluorine-doped tin oxide coated glass (FTO), stainless steels, indium tin oxide (ITO), and various metal coatings (Cr, Au) on either FTO or ITO. Preparations of NCC films are discussed in chapter 4.3. Metal nitrides were formed during the pyrolysis under N₂ of NCC films deposited on different metal films. These metal nitrides had insulating characteristics exhibiting high sheet resistance. For this reason, NCC films deposited on different metals and their coatings are not suitable for DSSC fabrication. The results reported in this chapter were obtained using FTO-coated glass.

7.2.1. Appearance of drop-cast NCC films

Images of NCC drop-cast films before and after pyrolysis are shown in Figure 7-1 (a, b). The as-cast NCC films were transparent, as can be seen in Figure 7-1 (a). After pyrolysis,

the optically transparent NCC films were transformed into opaque black films; see Figure 7-1 (b). The mechanisms of cellulose pyrolysis are described elsewhere.¹⁸² Low temperature ($\sim 600^{\circ}\text{C}$) carbonization of NCC introduces micropore formation in the final black film.¹⁸³ This can be advantageous as it enhances the surface area of this mesoporous carbon film relative to unpyrolyzed NCC, which presents a large electrode area for the reduction of triiodide.

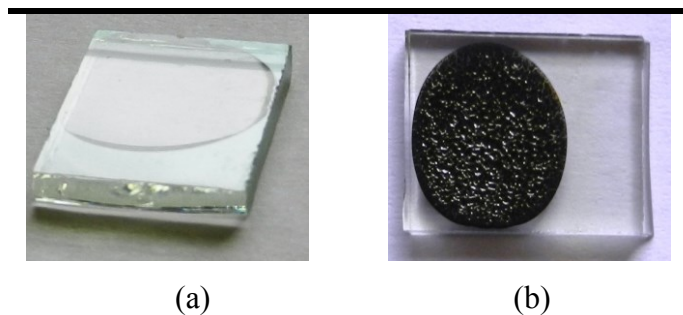


Figure 7-1: a) Drop-cast NCC film on FTO before pyrolysis, b) Drop-cast NCC film on FTO after pyrolysis.

7.2.2. Atomic force microscopy (AFM)

AFM images of these drop-cast films of NCC were also collected in order to study the morphology (Figure 7-2 (a, b)). AFM indicates significant changes in morphology. At first glance, the vertical scales of the two AFM micrographs appear similar. Before pyrolysis, the samples exhibited rod-like nanostructures in agreement with previous studies.¹⁸⁴ Following pyrolysis, the image appears to consist of identical triangular features of differing heights. These are AFM tip artifacts, indicating the presence of a large density of sharp, high aspect ratio asperities on the surface. In effect, each of these asperities is imaging the AFM tip.

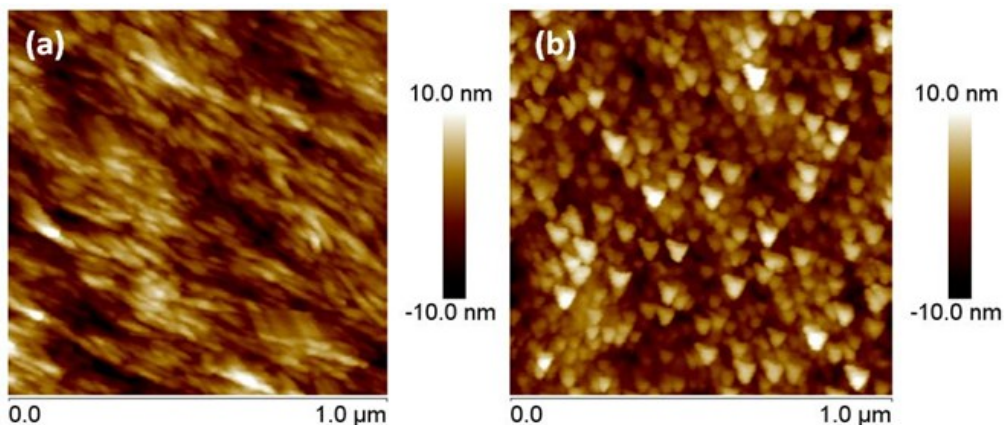


Figure 7-2: a) NCC film as-cast on FTO, b) Pyrolyzed NCC film on FTO.

7.2.3. Thermogravimetric analysis (TGA)

Thermogravimetric analysis was performed to evaluate the thermal stability of pyrolyzed NCC. TGA data along with its first derivative with respect to temperature (DTG) of 1 hr pyrolyzed NCC are plotted in Figure 7-3. From the TGA and DTG curves, two stages are observed. The first is at $T < 125^{\circ}\text{C}$ and the second in the range 314°C - 422°C . The initial mass loss in the first stage is attributed to the evaporation of adsorbed water in pyrolyzed NCC. The mass loss in the second stage corresponds to the combustion of pyrolyzed NCC (char) along with the production of CO which undergoes gas-phase oxidation to CO_2 .^{185,186} Most of the mass loss occurs below 500°C but still $\sim 10\%$ residue is left. The temperature window of the second stage observed here has been assigned to the combustion of amorphous carbon in previous studies.^{187,188} This finding is in agreement with previous reports, using XRD to determine the presence of amorphous carbon following pyrolysis of NCC under nitrogen.¹⁸⁹ TGA of NCC pyrolyzed at 4 hrs and 8 hrs at 600°C was also conducted and it was found to be indistinguishable from that of the 1 hr sample (see Figure 7-4), indicating that even 1 hr pyrolysis is sufficient to completely convert NCC to amorphous carbon.

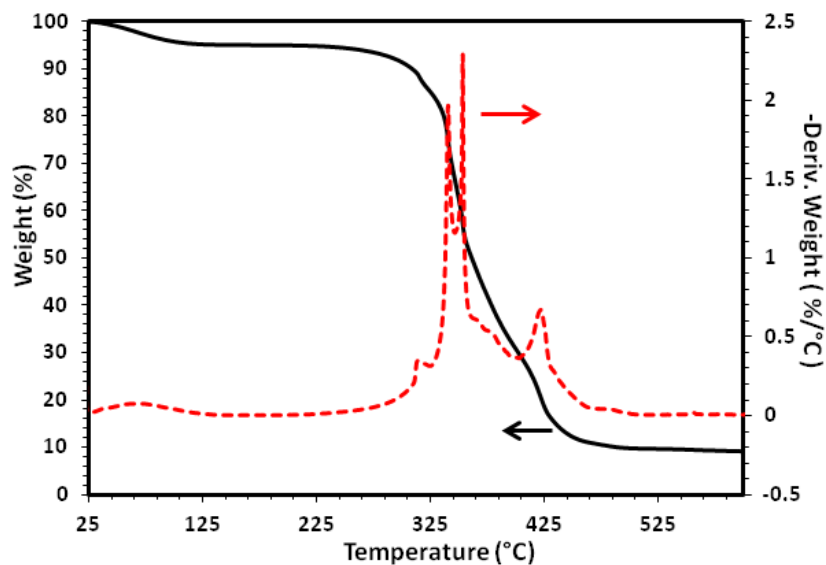


Figure 7-3: TGA and DTG of 1 hr pyrolyzed NCC.

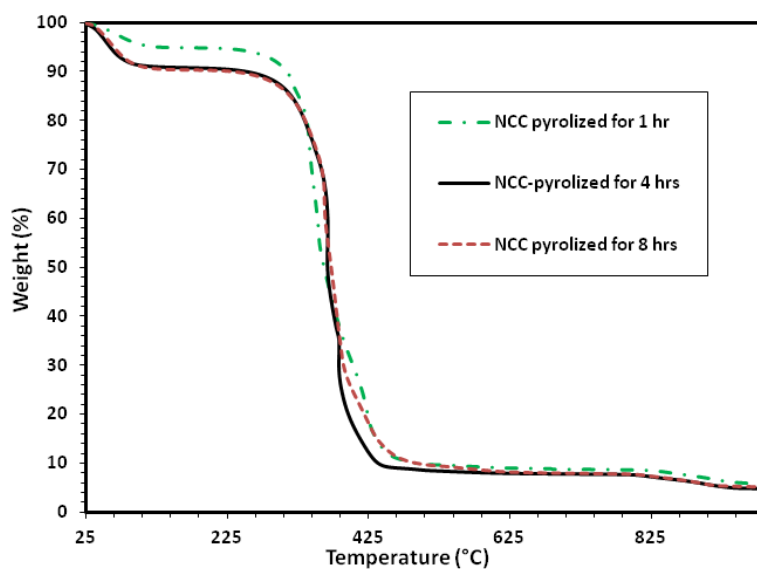


Figure 7-4: TGA of NCC pyrolyzed for 1, 4 and 8 hrs.

7.2.4. DSSC fabrication using drop-cast NCC films

DSSCs were fabricated using 1 hr pyrolyzed NCC films on FTO as counter electrode. Fabrication of photoanodes was performed as discussed in chapter 4.1 including the spin-coated TiO₂ blocking layer, but without TiCl₄ treatment. 60 μm Surlyn was used as a spacer between the photoanode and counter electrode.

7.2.5. Current density-voltage (J-V) analysis

Dark and illuminated J-V curves for DSSC constructed using the NCC counter electrodes are illustrated in Figure 7-5 and Figure 7-6, respectively. Performance metrics of this DSSC extracted from J-V curves are given in Table 7-1. At 1 sun illumination, the cell achieves a power conversion efficiency of 3.8%, a fill factor of 58%, and an open-circuit voltage of 0.7 V. By analyzing the slope of the J-V curves around the open-circuit point, we note that these cells contain a significant series resistance. At one sun, the specific series resistance is approximately $20 \text{ Ohm}\cdot\text{cm}^2$ ($R \approx 500 \text{ Ohms}$), and at four suns, it is approximately $12 \text{ Ohm}\cdot\text{cm}^2$ ($R \approx 300 \text{ Ohms}$). Given the near-square geometry of the substrate, the series resistance contributed by the FTO would be comparable to its sheet resistance following pyrolysis ($\approx 300\text{-}500 \text{ Ohms/square}$). We therefore conclude that the majority of the series resistance observed in the J-V curves is, in fact, due to the substrate itself, and not due to transport in the NCC film, electrolyte, or due to charge transfer at the electrolyte/counter electrode interface. This is obviously not ideal, as losses in the substrate, and not the cell, are therefore responsible for limiting the fill factor and power conversion efficiency at higher illumination. This highlights the importance of developing substrates that can better withstand the pyrolysis processing conditions.

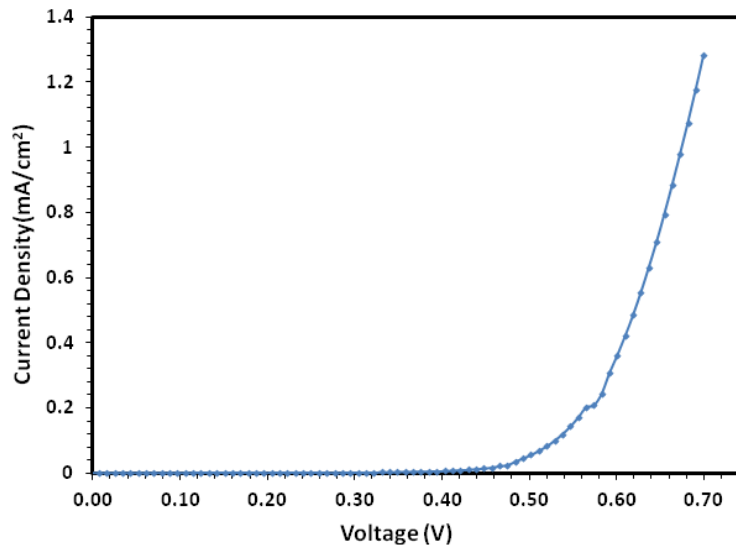


Figure 7-5: Dark J-V curve of DSSC with drop-cast NCC derived carbon CE.

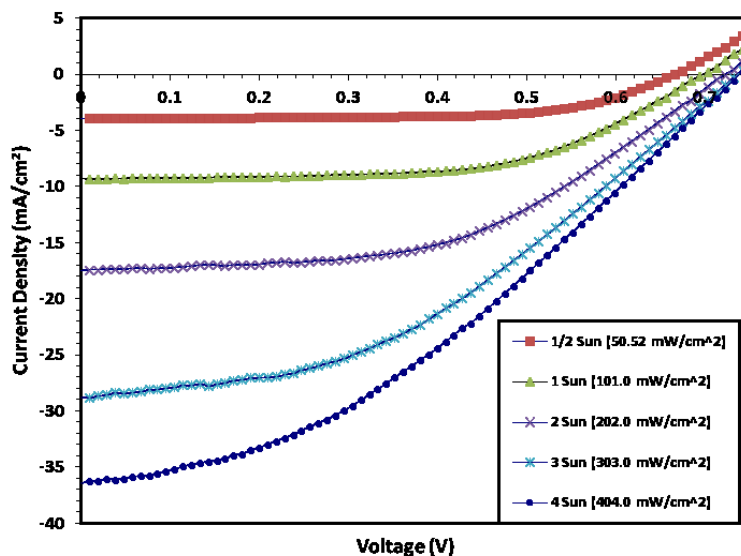


Figure 7-6: J-V curves of DSSC with drop-cast NCC derived carbon CE under various sun intensities.

Sun	V_{OC} (V) ± 0.005	J_{SC} (mA/cm ²)	FF (%)	η (%)
1/2 Sun	0.674	3.9 \pm 0.4	65 \pm 1	3.4 \pm 0.3
1 Sun	0.703	9 \pm 1.0	58 \pm 1	3.8 \pm 0.4
2 Sun	0.722	18 \pm 2	49 \pm 1	3.1 \pm 0.3
3 Sun	0.731	30 \pm 3	41 \pm 1	2.8 \pm 0.3
4 Sun	0.741	37 \pm 4	36 \pm 1	2.4 \pm 0.2

Table 7-1: Metrics extracted from J-V curves of DSSC with drop-cast NCC derived carbon CE under various sun intensities.

The performance metrics of these cells as function of illumination are presented in Figure 7-7 and Figure 7-8. We found that V_{OC} scales as the logarithm of the illumination intensity as expected (see Equation 8-1, Figure 7-8). The inset plot shows a linear increase of short-circuit current density (J_{SC}) with increasing illumination. The power conversion efficiency peaks at 1 sun (3.8%) and declines to 2.4% at four suns. We attribute much of this decline to I^2R losses in the substrate contribution to the series resistance, as discussed above. The decreasing FF with increasing illumination is also indicative of these I^2R losses.

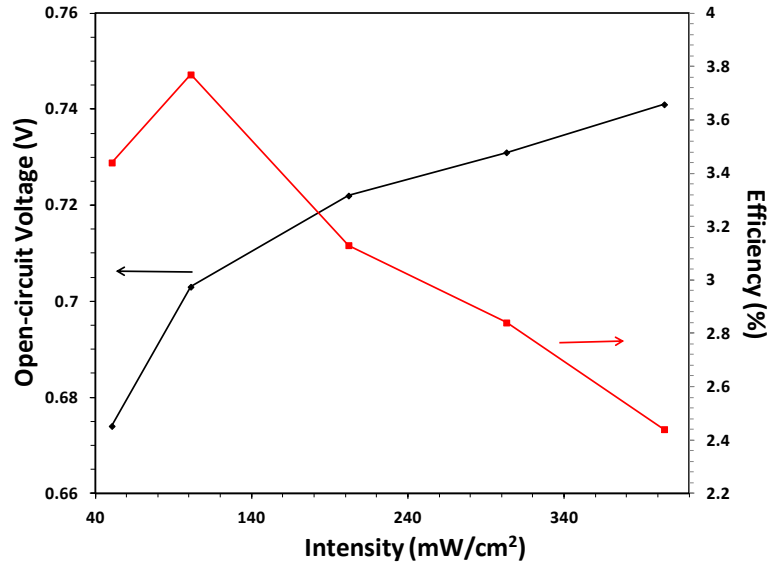


Figure 7-7: Cell metrics of DSSC with drop-cast NCC-derived carbon CE under various illumination intensities.

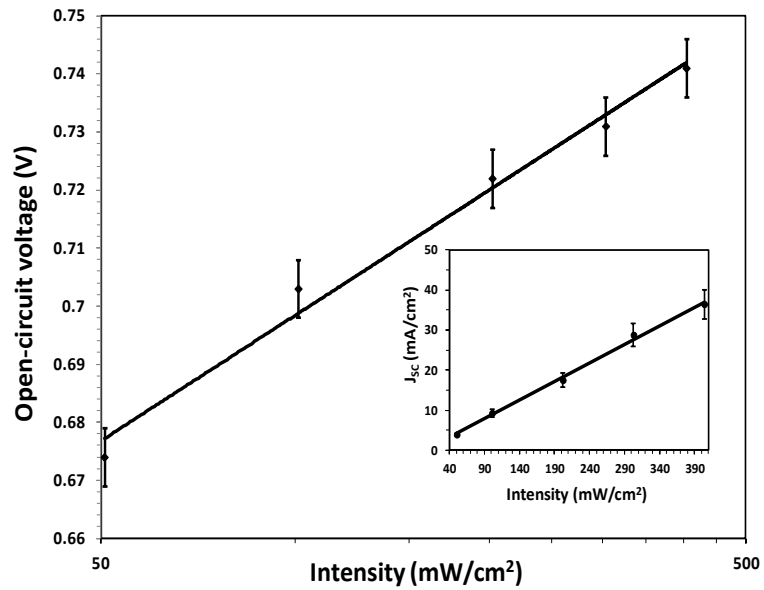


Figure 7-8: Open-circuit voltage of DSSC with drop-cast NCC derived carbon CE under various sun intensities. Inset: short-circuit current density as a function of illumination intensity.

7.2.6. Electrochemical impedance spectroscopy (EIS)

EIS was also conducted for FTO/NCC two terminal symmetric cells. This symmetric electrochemical cell was filled with same electrolyte used in DSSC fabrication. A silicone O-ring (I.D 7 mm, area 0.385 cm^2) was used as spacer. A Nyquist plot is shown in Figure 7-9; the data were fit using *z-view*. An equivalent circuit consisting of a parallel combination of a resistor and a CPE was used to model NCC/electrolyte interface. The diameter of the semicircle (99 Ohms) corresponds to the series combination of the charge transfer resistance at the two electrodes. The specific charge transfer resistance is therefore $19 \pm 1 \text{ Ohm} \cdot \text{cm}^2$ for the NCC/electrolyte interface, comparable to the series resistance (R_s) derived from illuminated J-V curves of the DSSCs.

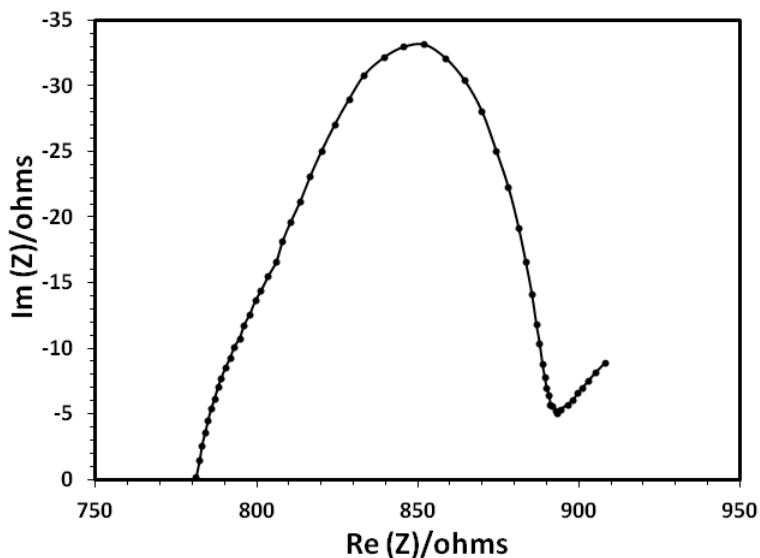


Figure 7-9: Nyquist plot of FTO\NCC two terminal symmetric cell of drop-cast pyrolyzed NCC film electrodes.

7.3. PREPARATION OF NCC FILMS BY SPIN COATING

NCC films were also prepared by spin-coating 5.5 wt% NCC on FTO. The layer was deposited by spin coating in two steps. In first the step, a spinning rate of 600 rpm for 5 minutes was used. In the second step, a spinning rate of 2000 rpm for 5 minutes was used. After spin coating, the sample was annealed for 2 minutes at 125°C on a hot plate

in order to dry the NCC. Following drying, this was pyrolyzed with the same procedure discussed in chapter 4.3.2. DSSCs were fabricated and tested as discussed in chapter 4.1.

7.3.1. Current density-voltage (J-V) analysis

Dark and illuminated J-V curves are shown in Figure 7-10 and Figure 7-11, respectively. Metrics from these curves are shown in Table 7-2. By analyzing the slope of the J-V curves around the open-circuit point, we note that this cell has a lower series resistance as compared to the cell fabricated with drop-casting i.e., at 1 sun, the series resistance of the cell is 334 ohms ($13.4 \text{ Ohm}\cdot\text{cm}^2$) while drop-casted cell has series resistance ~ 500 ohms ($20 \text{ Ohm}\cdot\text{cm}^2$). Due to this lower series resistance, the FF is higher for spin-coated devices. This low series resistance can be related to the thickness of the NCC films: drop-casted films are thicker as compared to spin-coated films. During pyrolysis of NCC, thicker NCC will result in a higher series resistance.

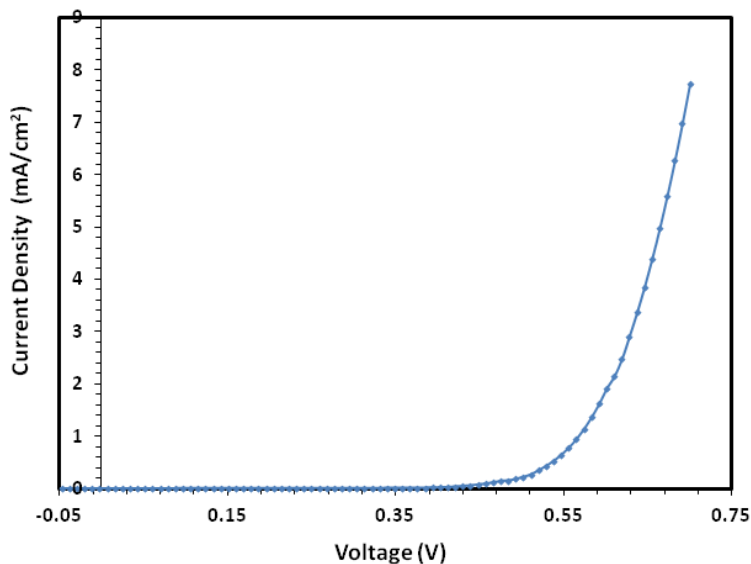


Figure 7-10: Dark J-V curve of spin-coated NCC counter electrode DSSC.

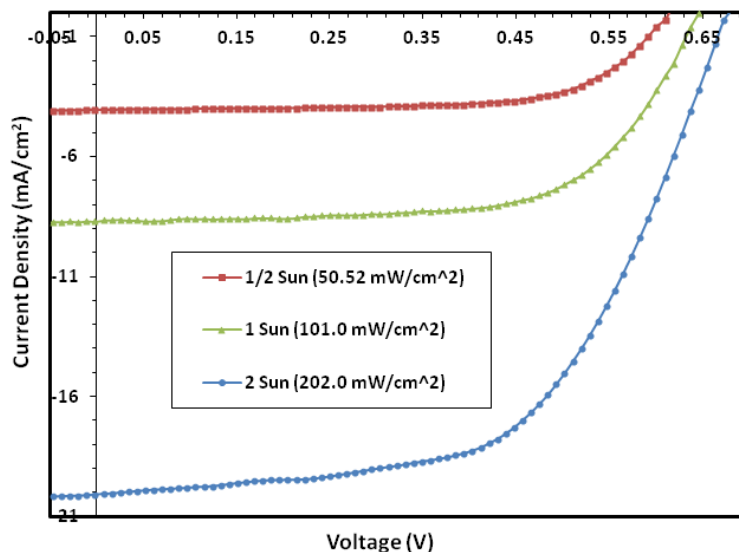


Figure 7-11: J-V curves of spin-coated NCC counter electrode DSSC under various sun intensities.

Sun	V_{OC} (V) ± 0.005	J_{SC} (mA/cm ²)	FF (%)	η (%)
1/2 Sun	0.610	4.1 \pm 0.4	67 \pm 1	3.4 \pm 0.3
1 Sun	0.646	8.7 \pm 0.9	65 \pm 1	3.6 \pm 0.4
2 Sun	0.650	20 \pm 2	60 \pm 1	3.9 \pm 0.4

Table 7-2: Metrics extracted from J-V curves of spin-coated NCC counter electrode DSSC.

7.4. CONCLUSIONS

We have demonstrated a carbon-based counter electrode material for DSSCs derived from nanocrystalline cellulose. The material is abundant, renewable, non-toxic, and sustainable. Power conversion efficiencies of nearly four percent have been measured in standard N3 dye/iodide-triiodide electrolyte DSSCs. High series resistance due to the increased sheet resistance of the FTO substrate during pyrolyzation of the NCC has been identified as a major loss mechanism in the cells. More work is required to identify appropriate counter electrode substrates and optimized NCC deposition techniques that will enable higher power conversion efficiencies.

CHAPTER 8 PRECIOUS METAL-FREE ORGANIC DYES

This chapter deals with the application of precious metal-free organic dye sensitizers in DSSCs based on self-assembled monolayers of phosphonates of simple oligothiophenes. The effect of increasing their conjugation units and incorporation of various anchor groups on device performance is also discussed.

8.1. BACKGROUND

A variety of functional groups can be used to bind the organic and organometallic dyes to the oxide but carboxylate and phosphonate groups are commonly used. The carboxylate group is comprised of delocalized electronic states due to its conjugated nature. Therefore, electron transfer to the oxide is thought to be easier as compared to phosphonate groups which are not conjugated. On the other hand, phosphonate groups are known to be more stable in terms of desorption from oxide surface under aqueous and alkaline conditions. Brennan et al. found higher solar conversion efficiency (0.57%) for carboxylate-linked porphyrin sensitizers as compared to their phosphonate counterparts (0.25%). They found that the carboxylate linkage is more quickly hydrolyzed and desorbed from the oxide surface under alkaline conditions than the phosphonate linkage¹⁹⁰. Bae et al. found that the phosphonate linkage was more stable than the carboxylate-linked ruthenium sensitizer on TiO₂ in aqueous conditions¹⁹¹. In a combined theoretical and experimental study, Bauer et al. found phosphonates are more strongly bound to aluminum oxide than carboxylates by studying adsorption and desorption of n-alkyl phosphonic and carboxylic acids on AlO_x surfaces¹⁹². Some other metal-free dyes have been studied from theoretical perspective^{193,194,195}, but not yet experimentally.^{196,197}

The goal of this work was to use metal-free self-assembled monolayers of phosphonates of simple oligothiophenes as dye sensitizers in DSSCs in lieu of conventional ruthenium based dyes. The effect of systematic structural modification of these systems in terms of

increasing number of thiophene units on the power-conversion efficiency of DSSCs was studied. The behavior and role of carboxylate and phosphonate anchoring groups (4TCC and 4TCP) was also studied towards the chemical stability of the monolayer to water, photoelectronic coupling with the chromophore, chemical absorptivity on the TiO₂ surface, and overall performance of DSSCs.

In previous studies, organic dyes adsorbed on TiO₂ have been characterized by various techniques including UV-vis absorption spectroscopy, water wetting contact angle measurements, atomic force microscopy (AFM), ellipsometry and x-ray photoelectron spectroscopy (XPS)¹⁹⁸, but the loading of these dyes has not been measured directly. A few studies have been done in which indirect measurements of dye loadings were studied¹⁹⁹. In order to understand the role of dye loading on DSSCs performance, direct measurements of surface molecular loading were made by quartz crystal microgravimetry (QCM). In our work, the molecular loadings of 3TP-6TP were comparable; the performance of DSSCs with these dyes can be associated with the change in the number of thiophene units.

8.2. SYNTHESIS OF ORGANIC DYE SENSITIZERS AND THEIR CHARACTERIZATION

All organic dyes used in this work were synthesized and characterized, and density functional theory (DFT) calculations performed, by Prof. Jeffrey Schwartz and Dr. Kung-Ching Liao (Princeton University). Fabrication and analysis of DSSCs using these dyes were done by the author at Dalhousie University.

8.2.1. Oligothiophene dyes

α -Oligothiophen-2-yl phosphonic acids 3TP, 4TP, 5TP and 6TP were synthesized²⁰⁰; their structures are shown in Figure 8-1. UV-vis absorption spectra of nTP for n = [3,6] in THF solution are shown in Figure 8-2, and important parameters extracted from these spectra are given in Table 8-1. These parameters, including structure and energy

potentials of 3TP-6TP, were calculated using density functional theory (DFT) (B3LYP/6-31G*). Absorption wavelength maxima (λ_{max}) of 3TP-6TP indicated red-shifting and an increase in absorption coefficient with increasing number of thiophene units. This can be attributed to the effective conjugation length of the chromophores.²⁰¹ The λ_{max} and molar extinction coefficients (ϵ) of 3TP-6TP were comparable to the unsubstituted α -oligothiophenes (3T-6T)²⁰¹, which indicates that the phosphonate groups of 3TP to 6TP do not strongly take part in conjugation with the α -oligothiophene motifs¹⁹⁶.

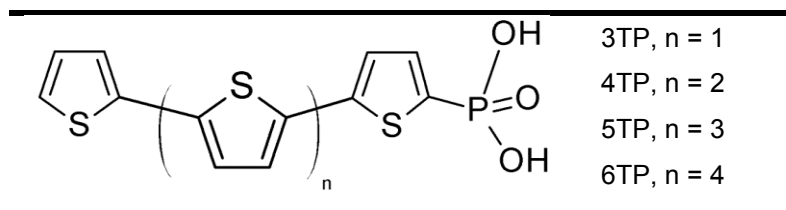


Figure 8-1: The structure of oligothiophene phosphonates dye sensitizers.

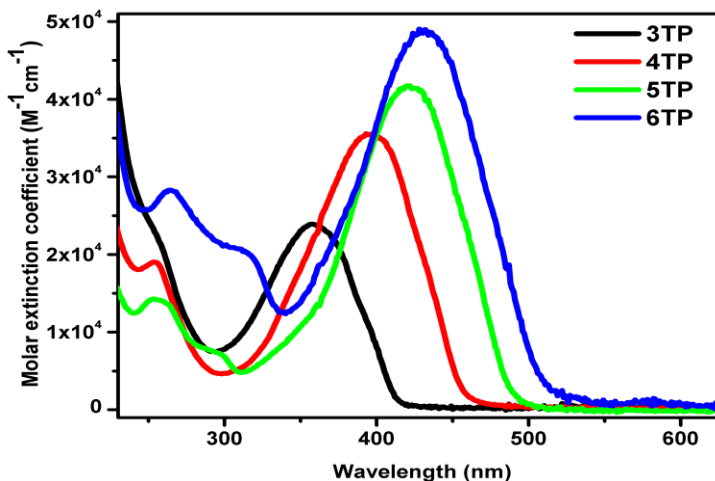


Figure 8-2: Absorption spectra of 3TP-6TP in THF.

Dye	λ_{max} (nm)	ϵ ($10^4 \times \text{M}^{-1} \text{cm}^{-1}$)	HOMO/LUMO (eV)	Band gap (eV)
3TP	357	2.38	-5.51/-2.20	3.31
4TP	395	3.55	-5.18/-2.22	2.96
5TP	421	4.16	-5.01/-2.27	2.74
6TP	430	4.89	-4.94/-2.38	2.56

Table 8-1: Photophysical properties and comparative parameters for the oligothiophene dyes.

Molecular loadings of 3TP-6TP on $\text{TiO}_2/\text{SiO}_2/\text{Si}$ were prepared using the “tethering by aggregation and growth” (T-BAG) method²⁰² and were measured using QCM. In a typical T-BAG procedure, sample substrates are held vertically in the dye solution. As the solution evaporates slowly, the meniscus travels across the substrate’s surface leaving behind the monolayer of dye molecules that are segregated at the solution/gas interface in analogy with Langmuir-Blodgett methods. In this case, dyes are weakly physisorbed from solution onto the substrate. Following evaporation, this sample substrate is heated in order to get chemisorbed SAMs of dyes on the substrates. The sample is then rinsed copiously to remove any remaining physisorbed layers. This process is repeated several times to get a saturated SAM on the sample.

Molecular loadings of oligothiophene samples that were prepared simply by dipping $\text{TiO}_2/\text{SiO}_2/\text{Si}$ in their solutions were also measured. In this case, reduction of molecular loading was observed as compared to the T-BAG method prepared samples. Surface morphology of TiO_2 deposited on SiO_2/Si substrate were studied using AFM, see Figure 8-3. SAMs of 4TP formed on TiO_2 layer by the T-BAG method were also studied using AFM, see Figure 8-4. Surface-conforming coverage was found to be comparable to that of the underlying oxide with rms roughness values of 0.24 nm and 0.28 nm, respectively. Ellipsometry was used to measure the thicknesses of SAMs of 3TP-6TP grown on TiO_2 surfaces, see Table 8-2.

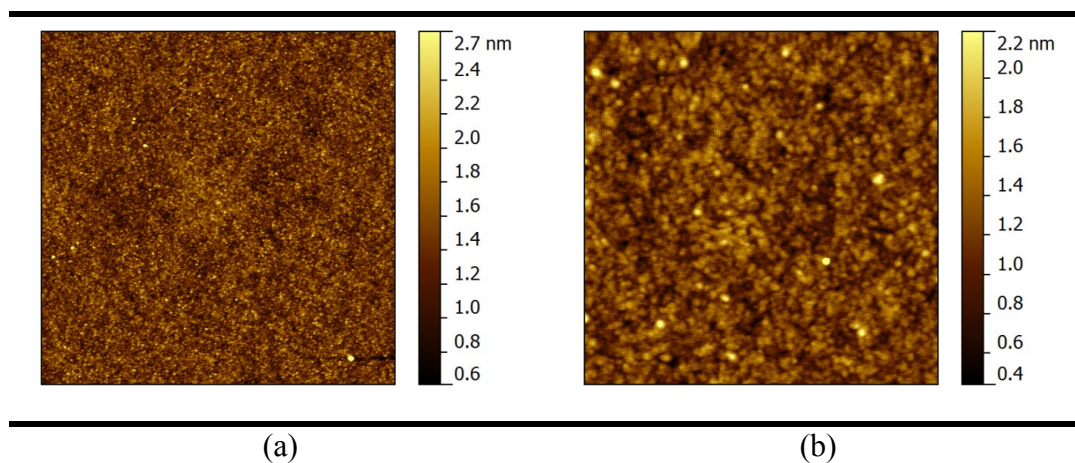


Figure 8-3: AFM images of TiO₂ (2 nm)/SiO₂/Si: (a) 5 μm x 5 μm (rms roughness: 0.28 nm); (b) 1 μm x 1 μm (rms roughness: 0.37 nm).

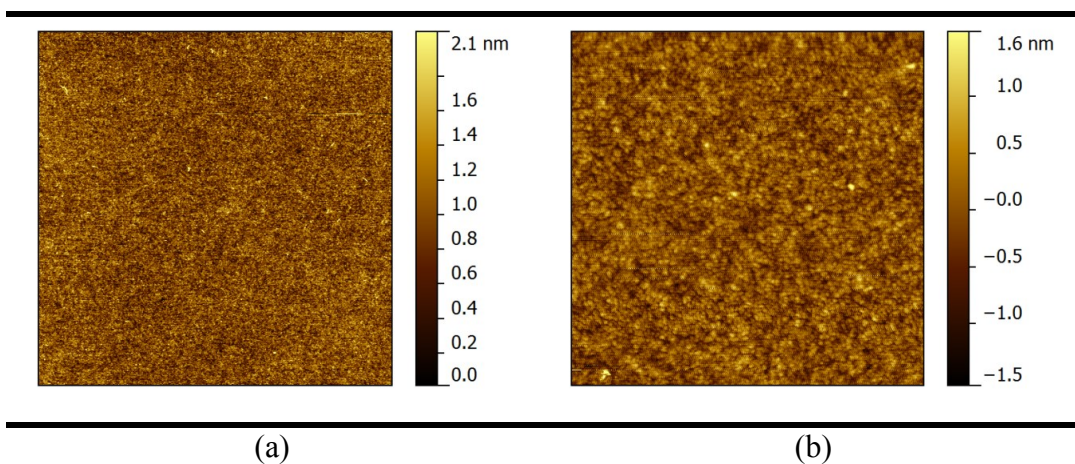


Figure 8-4: AFM images of 4TP (1.5 nm)/TiO₂/SiO₂/Si: (a) 5 μm x 5 μm (rms roughness: 0.24 nm); (b) 1 μm x 1 μm (rms roughness: 0.38 nm).

Dye	Contact angle (°)	Film thickness (nm)	Molecular loading (nmol/cm ²)
3TP	80	1.1	0.64 ^a (0.58) ^b
4TP	82	1.5	0.65 ^a (0.55) ^b
5TP	76	1.8	0.61 ^a (0.49) ^b
6TP	79	2.1	0.62 ^a (0.51) ^b

Table 8-2: Monolayer characterization parameters of 3TP-6TP dyes; a (SAMs prepared by T-BAG method); b (SAMs prepared by dipping in 0.1 mM in THF).

8.2.2. Cyanovinyl carboxylate and cyanovinyl phosphonate dyes

Cyanovinyl carboxylate was used as an electron-withdrawing group in the design of organic dyes.²⁰³ Their role was to shift the absorption maxima towards the visible portion of the solar spectrum. While comparing carboxylate and phosphonate anchoring groups, studies have shown that dyes with phosphonate anchors adsorbed on semiconductors can result in faster injection times and higher total power conversion efficiencies than carboxylate anchors¹⁹⁶. Therefore, phosphonate and carboxylate anchors attached to cyanovinyl-conjugated oligothiophene dyes are studied here. Structures of the cyanovinyl carboxylates and cyanovinyl phosphonates are shown in Figure 8-5. UV-vis absorption spectra of these compounds in THF solution are also measured and the important parameters extracted from these spectra are given in Table 8-3. These parameters, including structure and energy potentials, were calculated via DFT (B3LYP/6-31G*).

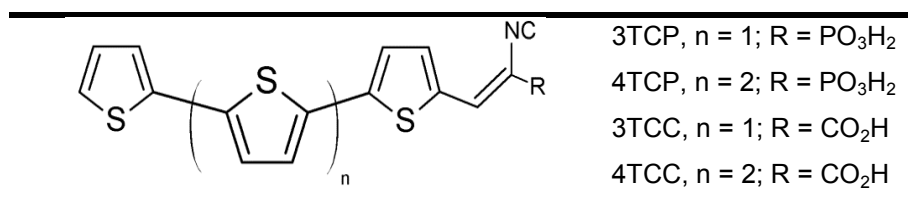


Figure 8-5: The structure of cyanovinyl carboxylate and cyanovinyl phosphonate dyes.

A comparison of absorption spectra of the cyanovinyl carboxylate- and cyanovinyl phosphonate-terminated oligothiophene dyes and the effect of the cyanovinyl group are shown in Figure 8-6 and Figure 8-7, respectively. A red-shift of their absorption maxima with higher extinction coefficients was observed as compared to their oligothiophene dye counterparts (Table 8-1). Phosphonate-terminated dyes absorbed at shorter wavelengths, but with larger band widths and higher extinction coefficients compared to their carboxylate analogs. This is associated with the electron-withdrawing character of cyanovinyl carboxylate and cyanovinyl phosphonate groups.

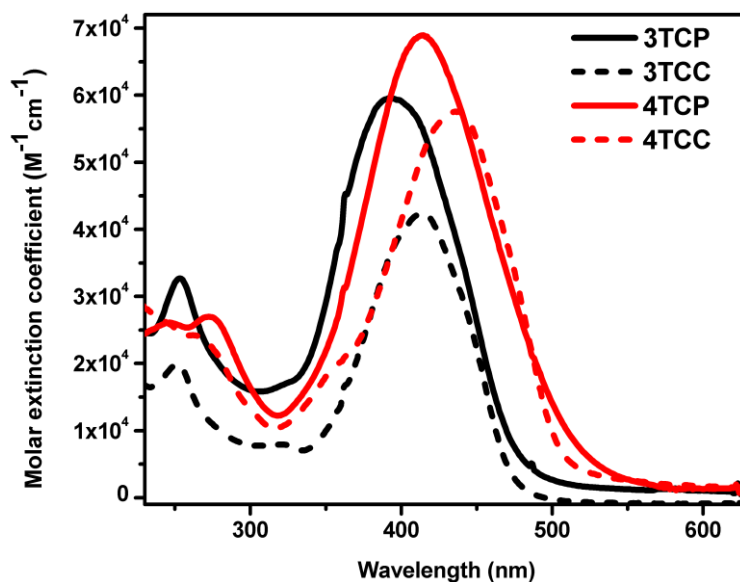


Figure 8-6: Absorption spectra in THF of cyanovinyl phosphonate species (3TCP, 4TCP) with cyanovinyl carboxylate species (3TCC, 4TCC).

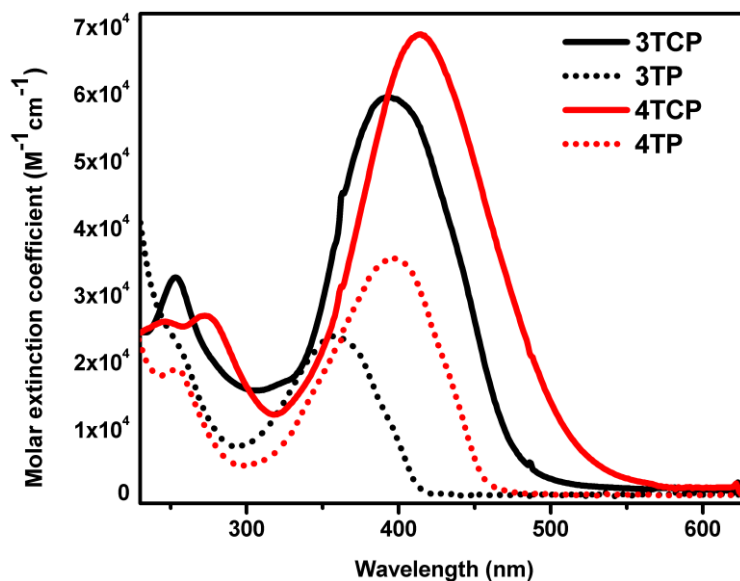


Figure 8-7: Absorption spectra in THF of cyanovinyl-substituted oligothiophene phosphonate (3TCP, 4TCP) with their unsubstituted phosphonate congeners (3TP, 4TP).

Dye	λ_{\max} (nm)	ϵ ($10^4 \times \text{M}^{-1}\text{cm}^{-1}$)	HOMO/LUMO (eV)	Band gap (eV)
3TCP	392 ^a (413) ^b	5.96	-5.42/-2.51	2.91
3TCC	413 ^a (416) ^b	4.23	-5.39/-2.56	2.83
4TCP	413 ^a (438) ^b	6.90	-5.10/-2.57	2.53
4TCC	436 ^a (440) ^b	5.77	-5.07/-2.62	2.45

Table 8-3: Photophysical properties and comparative parameters for the cyanovinyl carboxylate and cyanovinyl phosphonate dye sensitizers. ^a Absorptions of charge-transfer transition were measured in THF. ^b Absorption spectra were measured in DMF.

SAMs of 3TCP, 4TCP, 3TCC and 4TCC were prepared using T-BAG and simple dipping methods. Figure 8-8 showed the AFM images of 4TCP/TiO₂/SiO₂/Si and 4TCC/TiO₂/SiO₂/Si prepared using the T-BAG method from 1 μM solution in THF. Both of the images showed a conforming monolayer with the same homogeneity and surface roughness as that of the underlying oxide. Molecular loadings of these samples are also given in Table 8-4. In the case of the dipping process, low concentration solutions of 4TCP and 4TCC were prepared in THF/methanol (1:1) and TiO₂ substrates were soaked for 24 hours in 0.1 mM solutions of 4TCP and 4TCC in THF/methanol (1:1). QCM measurements revealed that 4TCC derivatives did not promote dense packing (0.04 nmol/cm²) as compared to 4TCP derivatives (0.44 nmol/cm²). This can be associated with the acidity of the phosphonic and carboxylic acids.^{204,205} The chemical bonding stabilities of 4TCP and 4TCC were also studied. Substrates were dipped for 5 min in DI water and rinsed with copious amount of dimethyl sulfoxide (6 cycles of dip and rinse). After rinsing, molecular loadings of these samples were measured by QCM. It was found that the molecular loading of 4TCC on TiO₂ decreased by 28% (from 0.47 to 0.34 nmol/cm²), whereas the molecular loading of 4TCP was reduced by only 6%. This shows that phosphonates were more strongly chemisorbed onto TiO₂ as compared to carboxylates.

Dye	Contact angle (°)	Film thickness (nm)	Molecular loading (nmol/cm ²)
3TCP	76	1.7	0.47 ^a (0.41) ^b
3TCC	72	1.8	0.51 ^a (0.43) ^b
4TCP	80	2.0	0.52 ^a (0.44) ^b
4TCC	70	2.0	0.55 ^a (0.47) ^c

Table 8-4: Monolayer characterization parameters of phosphonate and carboxylate dyes; ^a(SAMs prepared by T-BAG method); ^bSAMs prepared by dipping in 0.1 mM in THF; ^cSAMs prepared by dipping in 0.1 mM saturated dye solution (~2 mM in THF).

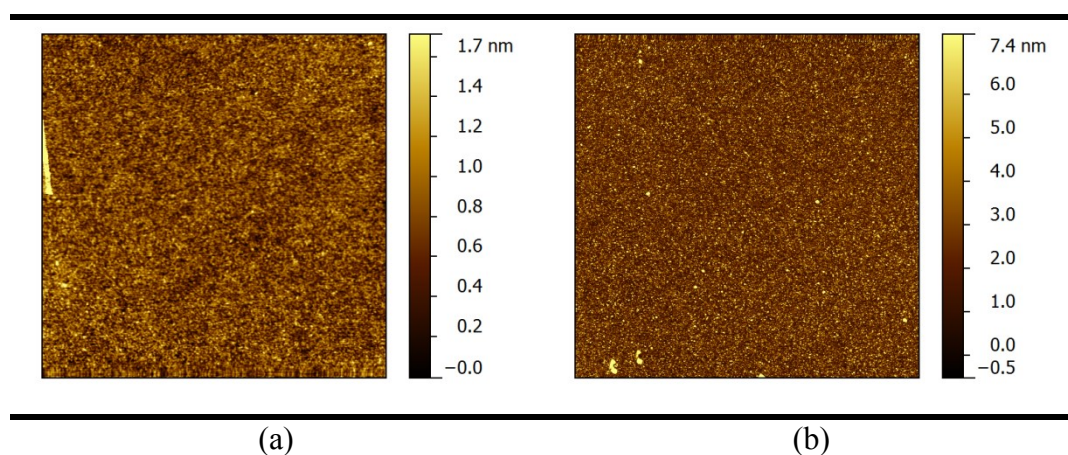


Figure 8-8: AFM images of (a) 4TCP (2 nm)/TiO₂/SiO₂/Si (rms roughness: 0.37 nm) and (b) 4TCC (2.0 nm)/TiO₂/SiO₂/Si (rms roughness: 0.42 nm). Scan area is 5 μm x 5 μm.

8.3. A NOTE ON DSSC FABRICATION

Photoanodes were prepared using the procedure described in chapter 4.1, including the spin-coated TiO₂ blocking layer, but without TiCl₄ treatment unless stated. These were sent to Prof. Jeffrey Schwartz and Dr. Kung-ching Liao (Princeton University) to deposit SAMs of the above discussed dye sensitizers. In normal DSSCs, before soaking in N3 dye, the TiO₂ photoanode was heated to 80°C to eliminate any moisture in the nanoporous TiO₂ matrix. In the case of depositing monolayers of these dyes, no pre-heating was performed.

8.4. DSSCs USING OLIGOTHIOPHENE PHOSPHONATE AND CARBOXYLATE

J-V curves of DSSCs fabricated with oligothiophene phosphonates 3TP-6TP are shown in Figure 8-9 and the metrics extracted from J-V curves are shown in Table 8-5. With increasing number of thiophene units in the dyes, V_{OC} increased monotonically from 0.43 V to 0.58 V, whereas the J_{SC} and efficiency increased exponentially. This improvement of device performance can be due to a number of reasons. Firstly, as the dye molecular loading for each SAM was comparable, the improvement can be associated to the red-shift absorption in the spectrum. A decreasing gap is necessary, but not sufficient, to produce higher efficiencies. For efficient DSSCs, the dye HOMO and LUMO positioning is of great importance. The LUMO of the dye must be positioned above the CB minimum of TiO_2 (~ -4.3 eV relative to the vacuum²⁰⁶) for efficient electron injection. Similarly, HOMO of the dye must be positioned below the redox potential level (~ -4.85 eV, 0.35 V vs SHE²⁰⁷ for I/I_3^-) of the redox couple for efficient dye regeneration. The computed HOMO and LUMO levels for the dyes reported here all meet these necessary criteria.

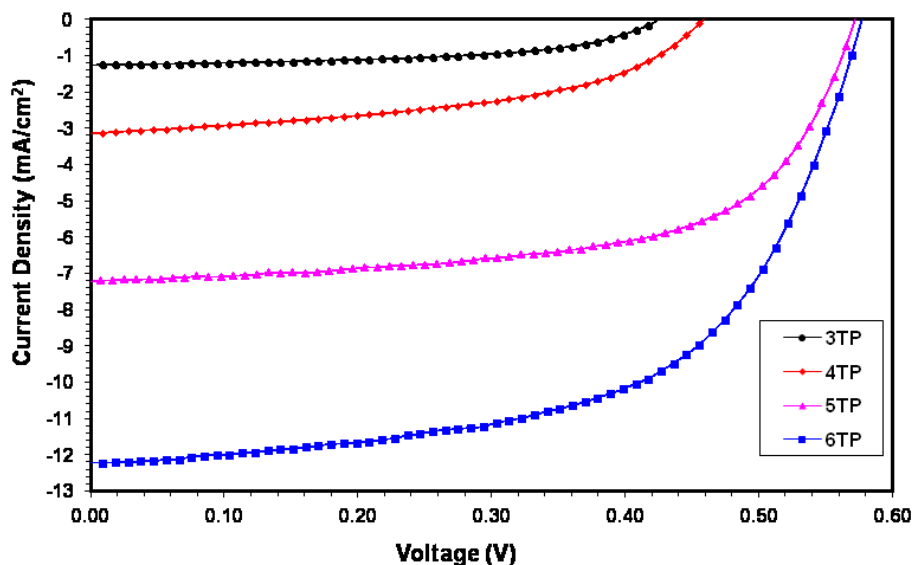


Figure 8-9: J-V curves for 3TP-6TP DSSCs at 1 sun.

DSSCs fabricated from (cyanovinyl) phosphonate (4TCP) gave 2.3% efficiency at 1 sun. This was more than 50% and 200% greater than those for 4TCC and 4TP DSSCs, respectively, as shown in Table 8-5. This higher efficiency can be correlated to the absorbance of 4TCP with a larger band width (full bandwidth at half height, *ca.* 100 nm) and higher extinction coefficient ($\epsilon = 6.9 \times 10^4 \text{ M}^{-1}\text{cm}^{-1}$) compared to its carboxylate (4TCC) or simple thiophene phosphonate (4TP) analogs, as shown in Figure 8-10 and Figure 8-11. 3T dyes also showed the same behavior. Therefore, we proposed that device efficiency of nT DSSCs was nTCP > nTCC > nTP as shown in Figure 8-12.

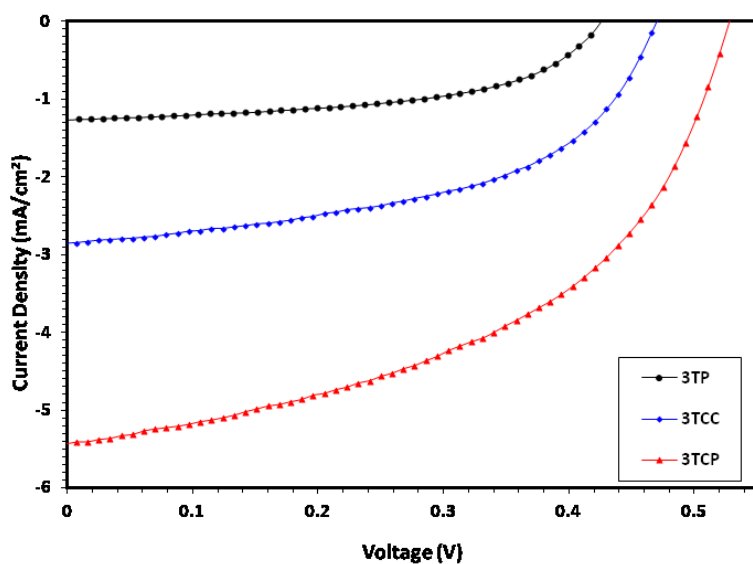


Figure 8-10: J-V curves for 3TP, 3TCC and 3TCP DSSCs at 1 sun.

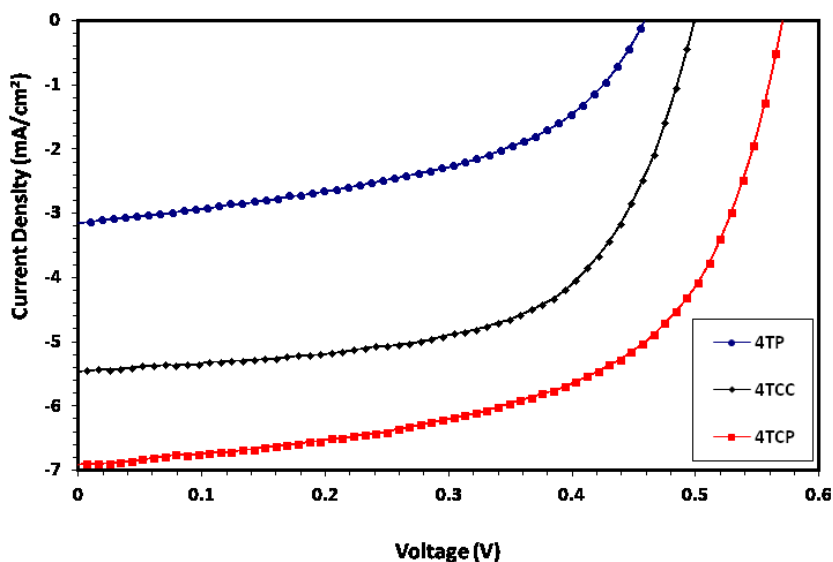


Figure 8-11: J-V curves for 4TP, 4TCC and 4TCP DSSCs at 1 sun.

Dye	V_{OC} (V) ± 0.005	J_{SC} (mA/cm ²)	FF (%)	η (%)
3TP	0.427	1.3 \pm 0.1	54 \pm 1	0.3 \pm 0.1
4TP	0.465	3.1 \pm 0.3	48 \pm 1	0.7 \pm 0.1
5TP	0.574	7.2 \pm 0.7	61 \pm 1	2.5 \pm 0.3
6TP	0.579	12.2 \pm 1.2	59 \pm 1	4.1 \pm 0.4
6TP*	0.592	15.9 \pm 1.6	51 \pm 1	4.8 \pm 0.5
3TCP	0.529	5.4 \pm 0.5	48 \pm 1	1.4 \pm 0.1
3TCC	0.475	2.9 \pm 0.3	51 \pm 1	0.7 \pm 0.1
4TCP	0.574	6.9 \pm 0.7	58 \pm 1	2.3 \pm 0.2
4TCC	0.502	5.5 \pm 0.6	61 \pm 1	1.7 \pm 0.2

Table 8-5: DSSC performance metrics for oligothiophene and oligothiophene with phosphonate and carboxylate dyes at 1 sun. * TiO₂ with TiCl₄ treatment.

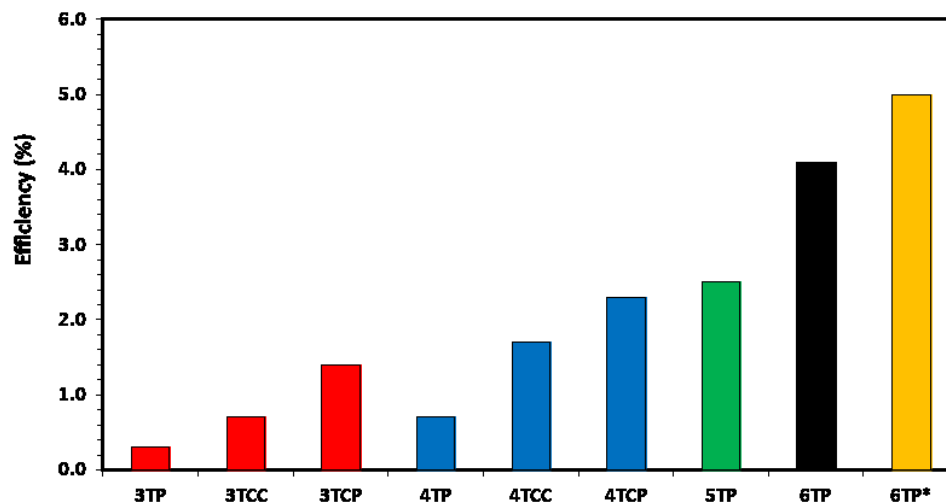


Figure 8-12: Comparative DSSC device performance of (oligothiophene) phosphonate, (cyanovinyl) phosphonate, and (cyanovinyl) carboxylate dyes. *TiO₂ first treated with TiCl₄.

8.5. PERFORMANCE ANALYSIS OF DSSCs

Understanding the short-circuit currents and open-circuit voltages of our nTP-based DSSCs requires analysis of several fundamental photophysical processes. Typically, V_{OC} increases with increasing illumination.²⁰⁸ In our case, we observed that with increase in conjugation length for nTP dyes, V_{OC} and J_{SC} increased monotonically. We suggest that this observed increase in V_{OC} is due to the increase in photocurrent (produced at the same illumination) as the conjugation length of the dye is increased and the absorption spectrum redshifts, aligning more favourably with the solar spectrum. In particular, in simple solar cell models, a photocurrent source (I_p) is placed in parallel with an ideal diode.⁶¹ The magnitude of I_p is a linear function of illumination for a given cell. Under open-circuit conditions, all of the photocurrent, I_p , must pass through the ideal diode, and the diode current must equal the photocurrent. Based on the Shockley diode equation (8-1), V_{OC} increases as the logarithm of the photocurrent.^{208,209} Using the short-circuit current density as a proxy for the photocurrent, we find that V_{OC} does indeed scale as the logarithm of the photocurrent (Figure 8-13), indicating that the observed change in V_{OC}

with an increasing number of thiophene rings can be understood as a result of the increased photocurrent density.

$$I_p = I_s \left(e^{\frac{qV_{OC}}{nk_B T}} - 1 \right) \text{ or } V_{OC} \approx \frac{nk_B T}{q} \ln \left(\frac{I_p}{I_s} \right) \text{ for } \frac{qV_{OC}}{nk_B T} \gg 1 \quad (8-1)$$

Equation 8-1: Diode reverse saturation current, I_s ; electronic charge, q ; ideality factor, n ; Boltzmann's constant, k_B ; temperature, T .

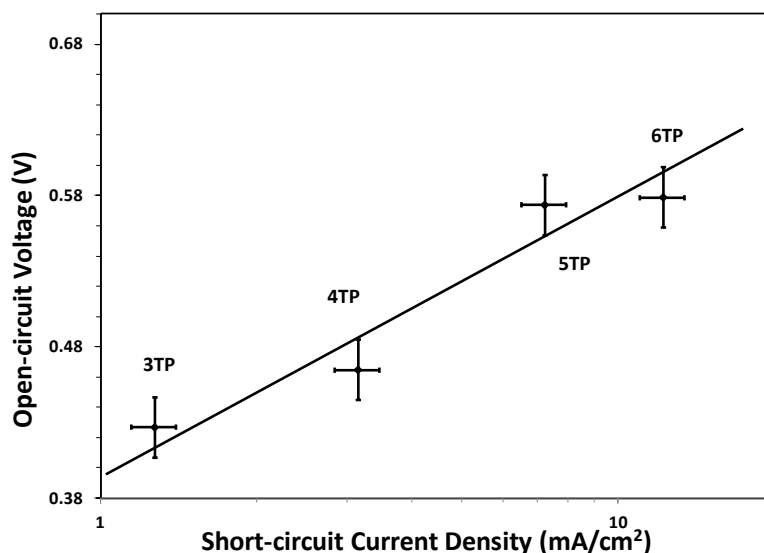


Figure 8-13: Plot of V_{OC} as a function of \ln of J_{SC} for n TP DSSCs.

The strong relationship between the short-circuit current density and the number of thiophene units in the dye reveals an interesting facet of photophysics that pertains to series of congener dyes that differ not only in band gap but also in molecular size. As seen in Table 8-5, the current density approximately doubles with each additional thiophene unit. As expected, the peak molar extinction coefficient increases as the number of thiophene rings also increases, and absorption spectra red-shift toward the maximum of the solar spectrum, near 530 nm (Figure 8-2). Thus, all other structural factors being equal, we would expect that the current produced by these devices will increase as thiophene rings are added to the dye but within the limits of system energetics as discussed in section 8.4. If the dye LUMO (HOMO) position were to approach the TiO_2 CBM (iodide/triiodide redox potential), charge transfer would slow, and would negatively impact the device efficiency.

8.6. CONCLUSIONS

A series of metal-free organic sensitizers based on oligothiophenes and (cyanovinyl)-terminated oligothiophenes was synthesized and successfully used as dye sensitizers in DSSCs. It was found that device performance improved with the increase in conjugation length of the oligothiophene moieties. Structural analysis of dye/TiO₂ substrates made by QCM and AFM showed that these sensitizers adsorbed homogeneously as monolayers without forming any multilayers. QCM studies showed that the molecular loadings of self-assembled monolayers of phosphonates and carboxylates prepared from 1 μM solutions on TiO₂ were denser as compared to a simple solution dipping process of carboxylate dyes onto TiO₂, where concentrations of two to three orders of magnitude greater were required. (Cyanovinyl) phosphonate-terminated oligothiophenes showed broader light absorption spectra and a red-shift in this absorption peak with higher extinction coefficients, as compared to their carboxylate analogs. This observation is in agreement with the superior performance of DSSCs made with phosphonate-compared to analogous carboxylate-terminated dyes. In terms of stability, the carboxylates showed significant dissociation in aqueous media as compared to the phosphonates. Overall, growth of homogeneous SAMs on TiO₂, high molecular loading, and good stability of phosphonate SAMs in terms of desorption under aqueous conditions exhibit great potential of these chromophores as metal-free organic dyes in DSSC technology.

CHAPTER 9 CONCLUSIONS AND FUTURE WORK

In this chapter, the major contributions of the work are summarized in section 9.1 and some key directions for future work are given in Section 9.2.

9.1. THESIS SUMMARY

This thesis provides three significant contributions to the field of DSSCs. The main goal of the work presented in this thesis is to replace precious materials used in the current technology of DSSCs with readily available, sustainable and cheap materials to further reduce the cost of this technology.

The first important step of this work was to understand key concepts necessary to fabricate standard DSSCs with the highest efficiencies possible, as compared to those available in the literature. In this regard, platinum based standard DSSCs were successfully optimized to achieve reproducible efficiencies of ~10% with TiCl_4 treatments.

The first significant contribution presented here was the application of CNTs as an alternative to Pt in the counter electrode of DSSCs. While working on this aspect, four well known CVD methods were used to grow non-aligned and vertically aligned CNTs directly on various commonly used substrates. We found that FTO-coated glass is not a suitable substrate for direct growth of CNTs using CVD methods due to the harsh growth conditions in the presence of process gases. Inexpensive substrates including aluminum and stainless steel were successfully used as substrates for CNT growth. Finally, DSSCs were successfully demonstrated with MW-VACNT electrodes, with metrics comparable to those constructed using Pt-based counter electrode. DSSCs with MW-VACNTs (length 36 μm) gave overall good performance, i.e. ~86% as efficient as Pt-based DSSCs.

The second significant contribution presented here involved the application of carbon derived from nanocrystalline cellulose (NCC) as an alternative to Pt in the counter electrodes of DSSCs. For the first time, we successfully demonstrated a carbon-based counter electrode material for DSSCs derived from NCC. The material is abundant, renewable, non-toxic, and sustainable. This DSSC gave power conversion efficiencies of ~4%, which is ~58% as efficient as Pt-based DSSCs.

Finally, the third contribution in this thesis involved the application of novel metal-free organic dye sensitizers as an alternative to Ru-based dyes used in standard DSSCs. Organic dyes have many advantages over organo-metallic dyes including ease of synthesis and higher extinction coefficients. A series of organic sensitizers based on oligothiophenes and (cyanovinyl)-terminated oligothiophenes were successfully employed as dye sensitizers in DSSCs. Oligothiophenes with cyanovinyl phosphonate showed broader light absorption spectra, red-shifted absorption peak and higher extinction coefficients as compared to their carboxylate analogs. These observations are in agreement with the superior performance of DSSCs made with phosphonate anchors versus carboxylate anchors oligothiophene dyes. Also, device performance improved with the increase in conjugation length of the oligothiophene moieties. DSSCs fabricated with simple oligothiophene sensitizers are ~62% as efficient as the cells based on conventional Ru-based dyes.

Significant contributions are done in this research work to achieve main goals by introducing various alternative materials to Pt and Ru in the fabrication of DSSCs. These materials show comparable performance to standard DSSCs. There is still room for improvements.

9.2. FUTURE RESEARCH DIRECTIONS

A few interesting future research directions are presented here that are the extension of this research work.

- During fabrication of standard Pt-based DSSCs with TiCl_4 treatment, higher J_{SC} and lower V_{OC} were observed for these devices as compared to the values in literature. This low V_{OC} may be due to the presence of HCl in the nanoporous matrix of TiO_2 layer. If this HCl can be eliminated from TiO_2 nanoporous matrix, we believe that the device performance of our standard Pt-based cells could be increased above $\sim 10\%$ efficiency.
- DSSCs fabricated with CNTs were slightly inferior to the Pt-based DSSCs in terms of their series resistance and short-circuit current density. Further improvements to get higher efficiency DSSCs can be made by optimizing CNT growth conditions and modifying/functionalizing the nanotube surfaces. EIS would be used to investigate the impact on charge transfer resistance. Stability tests of these devices under illumination should also be conducted.
- During the pyrolysis of the NCC, high series resistance due to the increased sheet resistance of the FTO substrate has been found as a major loss mechanism in these devices. Therefore, more work is required to identify appropriate counter electrode substrates, optimize NCC deposition techniques to enable higher power conversion efficiencies for these devices. Surface modification/functionalization of NCC should also be done to improve device performance.
- It would be interesting to fabricate DSSCs with 6TCP as it should give higher efficiencies due to further red-shifting of the absorption spectrum and higher extinction coefficients. In addition to this, systematic studies of the effect of various new systems of dyes having LUMO levels with different electron affinities on the efficiency of DSSC can be carried out

BIBLIOGRAPHY

1. Sopian, K.; Wan Daud, W. R., Challenges and future developments in proton exchange membrane fuel cells. *Renewable Energy* **2006**, *31* (5), 719-727.
2. Bisquert, J.; Cahen, D.; Hodes, G.; Rühle, S.; Zaban, A., Physical Chemical Principles of Photovoltaic Conversion with Nanoparticulate, Mesoporous Dye-Sensitized Solar Cells. *The Journal of Physical Chemistry B* **2004**, *108* (24), 8106-8118.
3. Moriarty, P.; Honnery, D., What is the global potential for renewable energy? *Renewable and Sustainable Energy Reviews* **2012**, *16* (1), 244-252.
4. US Department of Energy; Energy Information Administration, **2007**.
5. Chen, C. J, Physics of Solar energy; John Wiley & Sons: New York, **2011**.
6. Lewis, S., Powering the Planet. California Institute of Technology, **2005**.
7. Technology Roadmap, Solar photovoltaic energy, International Energy Agency (IEA).
8. http://www.nrel.gov/ncpv/images/efficiency_chart.jpg, 2013.
9. Chapin, D. M.; Fuller, C. S.; Pearson, G. L., A New Silicon p-n Junction Photocell for Converting Solar Radiation into Electrical Power. *Journal of Applied Physics* **1954**, *25* (5), 676-677.

-
10. Hegedus, S. S.; Luque, A., Status, trends, challenges and the bright future of solar electricity from photovoltaics. In Handbook of Photovoltaic Science and Engineering, Edited by: Hegedus, S.S. and Luque, A. John Wiley & Sons, West Sussex, **2003**.
11. Shockley, W.; Queisser, H. J., Detailed Balance Limit of Efficiency of p-n Junction Solar Cells. *Journal of Applied Physics* **1961**, 32 (3), 510-519.
12. Renewable energy technologies: cost analysis series. International Renewable Energy Agency (IRENA). Volume 1: Power Sector Issue 4/5. Solar Photovoltaics. June 2012.
13. Birkmire, R. W.; Eser, E., Polycrystalline thin film solar cells: Present Status and Future Potential. *Annual Review of Materials Science* **1997**, 27 (1), 625-653.
14. Green, M. A.; Emery, K.; King, D. L.; Hishikawa, Y.; Warta, W., Solar cell efficiency tables (version 29). *Progress in Photovoltaics: Research and applications* **2007**, 15 (1), 35-40.
15. Miles, R. W., Photovoltaic solar cells: Choice of materials and production methods. *Vacuum* 2006, 80 (10), 1090-1097.
16. Deng, X., Schiff, E.A., Amorphous silicon-based solar cells. In Handbook of Photovoltaic Science and Engineering, Edited by S. Hegedus and A. Luque. John Wiley & Sons, West Sussex, 2003.
17. First Solar (2011), First Solar Corporate Overview: Q2 2011, First Solar, Tempe, AZ. http://www.firstsolar.com/~media/WWW/Files/Downloads/PDF/FSLR_CorpOverview.ashx, Consulted in 2013.

-
18. Green, M. A.; Emery, K.; Hishikawa, Y.; Warta, W., Solar cell efficiency tables (version 37). *Progress in Photovoltaics: Research and applications* **2011**, *19* (1), 84-92.
19. Technology Roadmap: Solar Photovoltaic Energy, IEA/OECD, Paris. International Energy Agency (IEA), **2010**.
20. You, J.; Dou, L.; Yoshimura, K.; Kato, T.; Ohya, K.; Moriarty, T.; Emery, K.; Chen, C.-C.; Gao, J.; Li, G.; Yang, Y., A polymer tandem solar cell with 10.6% power conversion efficiency. *Nature Communications* **2013**, *4*, 1446.
21. <http://www.reuters.com/article/2013/01/16/heliatek-gmbh-idUSnBw9hDjSta+114+BSW20130116>.
22. Krebs, F. C.; Norrman, K., Analysis of the failure mechanism for a stable organic photovoltaic during 10 000 h of testing. *Progress in Photovoltaics: Research and Applications* **2007**, *15* (8), 697-712.
23. Reese, M. O.; Morfa, A. J.; White, M. S.; Kopidakis, N.; Shaheen, S. E.; Rumbles, G.; Ginley, D. S., Pathways for the degradation of organic photovoltaic P3HT:PCBM based devices. *Solar Energy Materials and Solar Cells* **2008**, *92* (7), 746-752.
24. Krebs, F. C., Degradation and stability of polymer and organic solar cells. *Solar Energy Materials and Solar Cells* **2008**, *92* (7), 685.
25. Manceau, M.; Chambon, S.; Rivaton, A.; Gardette, J.-L.; Guillerez, S.; Lemaître, N., Effects of long-term UV–visible light irradiation in the absence of oxygen on P3HT and P3HT:PCBM blend. *Solar Energy Materials and Solar Cells* **2010**, *94* (10), 1572-1577.

-
26. Peters, C. H.; Sachs-Quintana, I. T.; Kastrop, J. P.; Beaupré, S.; Leclerc, M.; McGehee, M. D., High Efficiency Polymer Solar Cells with Long Operating Lifetimes. *Advanced Energy Materials* **2011**, *1* (4), 491-494.
27. Gratzel, M., Molecular photovoltaics that mimic photosynthesis. *Pure and Applied Chemistry* **2001**, *73* (3), 459-467.
28. Grätzel, M., Recent Advances in Sensitized Mesoscopic Solar Cells. *Accounts of Chemical Research* **2009**, *42* (11), 1788-1798.
29. Liu, M. Z.; Johnston, M. B.; Snaith, H. J., Efficient planar heterojunction perovskite solar cells by vapour deposition. *Nature* **2013**, *501* (7467), 395-398.
30. Gueymard, C. A., The sun's total and spectral irradiance for solar energy applications and solar radiation models. *Solar Energy* **2004**, *76* (4), 423-453.
31. Willson, R. C.; Hudson, H. S., Solar luminosity variations in solar cycle 21. *Nature* **1988**, *332* (6167), 810-812.
32. Gast, P.R., Solar Radiation, in Handbook of Geo-physics, Edited by C.F. Campen et al., 14-30, **1960**.
33. American Society for Testing and Materials (ASTM) Terrestrial Reference Spectra for Photovoltaic Performance Evaluation (ASTM G173-03 Tables).
34. Papageorgiou, N., Counter-electrode function in nanocrystalline photoelectrochemical cell configurations. *Coordination Chemistry Reviews* **2004**, *248* (13-14), 1421-1446.

-
35. Koo, B. K.; Lee, D. Y.; Kim, H. J.; Lee, W. J.; Song, J. S.; Kim, H. J., Seasoning effect of dye-sensitized solar cells with different counter electrodes. *Journal of Electroceramics* **2006**, *17* (1), 79-82.
36. Wang, X.-F.; Tamiaki, H., Cyclic tetrapyrrole based molecules for dye-sensitized solar cells. *Energy & Environmental Science*, **2010**, *3*, 94–106.
37. Millington, K. R.; Fincher, K. W.; King, A. L., Mordant dyes as sensitizers in dye-sensitized solar cells. *Solar Energy Materials & Solar Cells* **2007**, *91*, 1618–1630.
38. Wang, M.; Anghel, A. M.; Marsan, B.; Cevey Ha, N.-L.; Pootrakulchote, N.; Zakeeruddin, S. M.; Grätzel, M., CoS Supersedes Pt as Efficient Electrocatalyst for Triiodide Reduction in Dye-Sensitized Solar Cells. *Journal of the American Chemical Society* **2009**, *131* (44), 15976-15977.
39. Lin, J.-Y.; Liao, J.-H.; Chou, S.-W., Cathodic electrodeposition of highly porous cobalt sulfide counter electrodes for dye-sensitized solar cells. *Electrochimica Acta* **2011**, *56* (24), 8818-8826.
40. Lin, J.-Y.; Liao, J.-H.; Wei, T.-C., Honeycomb-like CoS Counter Electrodes for Transparent Dye-Sensitized Solar Cells. *Electrochemical and Solid-State Letters* **2011**, *14* (4), D41-D44.
41. Lin, J.-Y., Mesoporous Electrodeposited-CoS Film as a Counter Electrode Catalyst in Dye-Sensitized Solar Cells. *Journal of The Electrochemical Society* **2012**, *159* (2), D65.

-
42. Zhang, X.; Wang, S.; Lu, S.; Su, J.; He, T., Influence of doping anions on structure and properties of electro-polymerized polypyrrole counter electrodes for use in dye-sensitized solar cells. *Journal of Power Sources* **2014**, *246* (0), 491-498.
43. Yin, X.; Wu, F.; Fu, N.; Han, J.; Chen, D.; Xu, P.; He, M.; Lin, Y., Facile Synthesis of Poly(3,4-ethylenedioxythiophene) Film via Solid-State Polymerization as High-Performance Pt-Free Counter Electrodes for Plastic Dye-Sensitized Solar Cells. *ACS Applied Materials & Interfaces* **2013**, *5* (17), 8423-8429.
44. Zhang, X. N.; Zhang, J.; Cui, Y. Z.; Feng, J. W.; Zhu, Y. J., Carbon/Polymer Composite Counter-Electrode Application in Dye-Sensitized Solar Cells. *Journal of Applied Polymer Science* **2013**, *128* (1), 75-79.
45. Wu, H.; Lv, Z.; Chu, Z.; Wang, D.; Hou, S.; Zou, D., Graphite and platinum's catalytic selectivity for disulfide/thiolate (T_2/T^-) and triiodide/iodide (I_3^-/I^-). *Journal of Materials Chemistry* **2011**, *21* (38), 14815-14820.
46. Veerappan, G.; Bojan, K.; Rhee, S.-W., Sub-micrometer-sized graphite as a conducting and catalytic counter electrode for dye-sensitized solar cells. *ACS Applied Materials & Interfaces* **2011**, *3* (3), 857-862.
47. Murakami, T. N.; Ito, S.; Wang, Q.; Nazeeruddin, M. K.; Bessho, T.; Cesar, I.; Liska, P.; Humphry-Baker, R.; Comte, P.; Pechy, P.; Gratzel, M., Highly efficient dye-sensitized solar cells based on carbon black counter electrodes. *Journal of The Electrochemical Society* **2006**, *153* (12), A2255-A2261.
48. Chen, Y.; Zhu, Y. J.; Chen, Z. G., Three-dimensional ordered macroporous carbon as counter electrodes in dye-sensitized solar cells. *Thin Solid Films* **2013**, *539*, 122-126.

-
49. Imoto, K.; Takahashi, K.; Yamaguchi, T.; Komura, T.; Nakamura, J.-i.; Murata, K., High-performance carbon counter electrode for dye-sensitized solar cells. *Solar Energy Materials and Solar Cells* **2003**, *79* (4), 459-469.
50. Huang, Z.; Liu, X.; Li, K.; Li, D.; Luo, Y.; Li, H.; Song, W.; Chen, L.; Meng, Q., Application of carbon materials as counter electrodes of dye-sensitized solar cells. *Electrochemistry Communications* **2007**, *9* (4), 596-598.
51. Lee, W. J.; Ramasamy, E.; Lee, D. Y.; Song, J. S., Efficient dye-sensitized solar cells with catalytic multiwall carbon nanotube counter electrodes. *ACS Applied Materials & Interfaces* **2009**, *1* (6), 1145-1149.
52. Huang, S.; Sun, H.; Huang, X.; Zhang, Q.; Li, D.; Luo, Y.; Meng, Q., Carbon nanotube counter electrode for high-efficient fibrous dye-sensitized solar cells. *Nanoscale Research Letters* **2012**, *7* (1), 1-7.
53. Hao, F.; Wang, Z.; Luo, Q.; Lou, J.; Li, J.; Wang, J.; Fan, S.; Jiang, K.; Lin, H., Highly catalytic cross-stacked superaligned carbon nanotube sheets for iodine-free dye-sensitized solar cells. *Journal of Materials Chemistry* **2012**, *22* (42), 22756-22762.
54. Hino, T.; Ogawa, Y.; Kuramoto, N., Preparation of functionalized and non-functionalized fullerene thin films on ITO glasses and the application to a counter electrode in a dye-sensitized solar cell. *Carbon* **2006**, *44* (5), 880-887.
55. Kavan, L.; Yum, J.-H.; Grätzel, M., Graphene Nanoplatelets Outperforming Platinum as the Electrocatalyst in Co-Bipyridine-Mediated Dye-Sensitized Solar Cells. *Nano Letters* **2011**, *11* (12), 5501-5506.

-
56. Roy-Mayhew, J. D.; Boschloo, G.; Hagfeldt, A.; Aksay, I. A., Functionalized Graphene Sheets as a Versatile Replacement for Platinum in Dye-Sensitized Solar Cells. *ACS Applied Materials & Interfaces* **2012**, *4* (5), 2794-2800.
57. Kay, A.; Gratzel, M., Low cost photovoltaic modules based on dye sensitized nanocrystalline titanium dioxide and carbon powder. *Sol Energ Mat Sol C* **1996**, *44* (1), 99-117.
58. Wroblowa, H. S.; Saunders, A., Flow-through Electrodes .2. I_3^-/I^- Redox Couple. *Journal of Electroanalytical Chemistry* **1973**, *42* (3), 329-346.
59. Tarasevich, M.R.; Khrushcheva, E.I.; in: B.E. Conway, J.O'M. Bockris, R.E. White (Eds.), *Modern Aspects of Electrochemistry*, Plenum Press, New York, **1989**, 19, 295.
60. Nam, J. G.; Park, Y. J.; Kim, B. S.; Lee, J. S., Enhancement of the efficiency of dye-sensitized solar cell by utilizing carbon nanotube counter electrode. *Scripta Materialia* **2010**, *62* (3), 148-150.
61. Ito, S.; Miura, H.; Uchida, S.; Takata, M.; Sumioka, K.; Liska, P.; Comte, P.; Pechy, P.; Gratzel, M., High-conversion-efficiency organic dye-sensitized solar cells with a novel indoline dye. *Chemical Communications* **2008**, (41), 5194-5196.
62. Hwang, S.; Lee, J. H.; Park, C.; Lee, H.; Kim, C.; Park, C.; Lee, M.-H.; Lee, W.; Park, J.; Kim, K.; Park, N.-G.; Kim, C., A highly efficient organic sensitizer for dye-sensitized solar cells. *Chemical Communications* **2007**, (46), 4887-4889.
63. Wang, Z. S.; Cui, Y.; Hara, K.; Dan-oh, Y.; Kasada, C.; Shinpo, A., A High-Light-Harvesting-Efficiency Coumarin Dye for Stable Dye-Sensitized Solar Cells. *Advanced Materials* **2007**, *19* (8), 1138-1141.

-
64. Mishra, A.; Ma, C.-Q.; Bäuerle, P., Functional Oligothiophenes: Molecular Design for Multidimensional Nanoarchitectures and Their Applications†. *Chemical Reviews* **2009**, *109* (3), 1141-1276.
65. Lee, S.-H. A.; Abrams, N. M.; Hoertz, P. G.; Barber, G. D.; Halaoui, L. I.; Mallouk, T. E., Coupling of Titania Inverse Opals to Nanocrystalline Titania Layers in Dye-Sensitized Solar Cells†. *The Journal of Physical Chemistry B* **2008**, *112* (46), 14415-14421.
66. Cahen, D.; Hodes, G.; Gratzel, M.; Guillemoles, J. F.; Riess, I., Nature of photovoltaic action in dye-sensitized solar cells. *J. Phys. Chem. B* **2000**, *104* (9), 2053-2059.
67. Hara, K.; Arakawa, H., Current status of dye-sensitized solar cells. Semiconductor photochemistry and photophysics. Editors V. Ramamurthy and Kirk, S. Schanze. **2003**, *10*, 123-171.
68. Hagfeldt, A.; Grätzel, M., Molecular Photovoltaics. *Accounts of Chemical Research* **2000**, *33* (5), 269-277.
69. Asbury, J. B.; Ellingson, R. J.; Ghosh, H. N.; Ferrere, S.; Nozik, A. J.; Lian, T. Q., Femtosecond IR study of excited-state relaxation and electron-injection dynamics of Ru(dcbpy)₂(NCS)₂ in solution and on nanocrystalline TiO₂ and Al₂O₃ thin films. *Journal of Physical Chemistry B* **1999**, *103* (16), 3110-3119.
70. Ramakrishna, G.; Jose, D. A.; Kumar, D. K.; Das, A.; Palit, D. K.; Ghosh, H. N., Strongly coupled ruthenium-polypyridyl complexes for efficient electron injection in

dye-sensitized semiconductor nanoparticles. *J. Phys. Chem. B* **2005**, *109* (32), 15445-15453.

71. Kuang, D.; Ito, S.; Wenger, B.; Klein, C.; Moser, J.-E.; Humphry-Baker, R.; Zakeeruddin, S. M.; Grätzel, M., High Molar Extinction Coefficient Heteroleptic Ruthenium Complexes for Thin Film Dye-Sensitized Solar Cells. *Journal of the American Chemical Society* **2006**, *128* (12), 4146-4154.

72. Benkő, G.; Kallioinen, J.; Korppi-Tommola, J. E. I.; Yartsev, A. P.; Sundström, V., Photoinduced Ultrafast Dye-to-Semiconductor Electron Injection from Nonthermalized and Thermalized Donor States. *Journal of the American Chemical Society* **2001**, *124* (3), 489-493.

73. Janne Halme, Dye-sensitized nanostructured and organic photovoltaic cells: technical review and preliminary tests. Master thesis, Helsinki University of Technology, **2002**.

74. Gratzel, M.; Klug, D. R.; Durrant, J. R., , Dye-Sensitized Mesoscopic Solar Cells. *Nanostructured and Photoelectrochemical Systems For Solar Photon Conversion*. Editors Mary D. Archer and Arthur J. Nozik **2008**, *3*, 503-536.

75. Hagfeldt, A.; Graetzel, M., Light-Induced Redox Reactions in Nanocrystalline Systems. *Chemical Reviews* **1995**, *95* (1), 49-68.

76. Tachibana, Y.; Moser, J. E.; Grätzel, M.; Klug, D. R.; Durrant, J. R., Subpicosecond Interfacial Charge Separation in Dye-Sensitized Nanocrystalline Titanium Dioxide Films. *The Journal of Physical Chemistry* **1996**, *100* (51), 20056-20062.

77. Hannappel, T.; Burfeindt, B.; Storck, W.; Willig, F., Measurement of Ultrafast Photoinduced Electron Transfer from Chemically Anchored Ru-Dye Molecules into Empty Electronic States in a Colloidal Anatase TiO₂ Film. *The Journal of Physical Chemistry B* **1997**, *101* (35), 6799-6802.

78. Cao, F.; Oskam, G.; Meyer, G. J.; Searson, P. C., Electron Transport in Porous Nanocrystalline TiO₂ Photoelectrochemical Cells. *The Journal of Physical Chemistry* **1996**, *100* (42), 17021-17027.

79. Solbrand, A.; Lindström, H.; Rensmo, H.; Hagfeldt, A.; Lindquist, S.-E.; Södergren, S., Electron Transport in the Nanostructured TiO₂-Electrolyte System Studied with Time-Resolved Photocurrents. *The Journal of Physical Chemistry B* **1997**, *101* (14), 2514-2518.

80. Solbrand, A.; Henningsson, A.; Södergren, S.; Lindström, H.; Hagfeldt, A.; Lindquist, S.-E. J., Charge Transport Properties in Dye-Sensitized Nanostructured TiO₂ Thin Film Electrodes Studied by Photoinduced Current Transients. *The Journal of Physical Chemistry* **1999**, *103*, 1078-1083.

81. Sommeling, P. M.; Rieffe, H. C.; van Roosmalen, J. A. M.; Schönecker, A.; Kroon, J. M.; Wienke, J. A.; Hirsch, A., Spectral response and IV-characterization of dye-sensitized nanocrystalline TiO₂ solar cells. *Solar Energy Materials and Solar Cells* **2000**, *62* (4), 399-410.

82. Hoyer, P.; Weller, H., Potential-Dependent Electron Injection in Nanoporous Colloidal ZnO Films. *The Journal of Physical Chemistry* **1995**, *99* (38), 14096-14100.

-
83. Schwarzburg, K.; Willig, F., Influence of trap filling on photocurrent transients in polycrystalline TiO₂. *Applied Physics Letters*. **1991**, 58 (22), 2520-2522.
84. de Jongh, P. E.; Vanmaekelbergh, D., Trap-Limited Electronic Transport in Assemblies of Nanometer-Size TiO₂ Particles. *Physical Review Letters* **1996**, 77 (16), 3427.
85. de Jongh, P. E.; Vanmaekelbergh, D., Investigation of the Electronic Transport Properties of Nanocrystalline Particulate TiO₂ Electrodes by Intensity-Modulated Photocurrent Spectroscopy. *The Journal of Physical Chemistry B* **1997**, 101 (14), 2716-2722.
86. Koenenkamp, R.; Henninger, R.; Hoyer, P., Photocarrier transport in colloidal titanium dioxide films. *The Journal of Physical Chemistry* **1993**, 97 (28), 7328-7330.
87. Wahl, A.; Augustynski, J., Charge Carrier Transport in Nanostructured Anatase TiO₂ Films Assisted by the Self-Doping of Nanoparticles. *The Journal of Physical Chemistry B* **1998**, 102 (40), 7820-7828.
88. van de Lagemaat, J.; Frank, A. J., Effect of the Surface-State Distribution on Electron Transport in Dye-Sensitized TiO₂ Solar Cells: Nonlinear Electron-Transport Kinetics. *The Journal of Physical Chemistry B* **2000**, 104 (18), 4292-4294.
89. O'Regan, B.; Moser, J.; Anderson, M.; Graetzel, M., Vectorial electron injection into transparent semiconductor membranes and electric field effects on the dynamics of light-induced charge separation. *The Journal of Physical Chemistry* **1990**, 94 (24), 8720-8726.

-
90. Soedergren, S.; Hagfeldt, A.; Olsson, J.; Lindquist, S.-E., Theoretical Models for the Action Spectrum and the Current-Voltage Characteristics of Microporous Semiconductor Films in Photoelectrochemical Cells. *The Journal of Physical Chemistry* **1994**, *98* (21), 5552-5556.
91. Solbrand, A.; Lindström, H.; Rensmo, H.; Hagfeldt, A.; Lindquist, S.-E.; Södergren, S., Electron Transport in the Nanostructured TiO₂-Electrolyte System Studied with Time-Resolved Photocurrents. *The Journal of Physical Chemistry B* **1997**, *101* (14), 2514-2518.
92. Dloczik, L.; Ilperuma, O.; Lauermann, I.; Peter, L. M.; Ponomarev, E. A.; Redmond, G.; Shaw, N. J.; Uhlendorf, I., Dynamic Response of Dye-Sensitized Nanocrystalline Solar Cells: Characterization by Intensity-Modulated Photocurrent Spectroscopy. *The Journal of Physical Chemistry B* **1997**, *101* (49), 10281-10289.
93. Bisquert, J.; Vikhrenko, V. S., Interpretation of the Time Constants Measured by Kinetic Techniques in Nanostructured Semiconductor Electrodes and Dye-Sensitized Solar Cells. *The Journal of Physical Chemistry B* **2004**, *108* (7), 2313-2322.
94. Fisher, A. C.; Peter, L. M.; Ponomarev, E. A.; Walker, A. B.; Wijayantha, K. G. U., Intensity Dependence of the Back Reaction and Transport of Electrons in Dye-Sensitized Nanocrystalline TiO₂ Solar Cells. *The Journal of Physical Chemistry B* **2000**, *104* (5), 949-958.
95. Bisquert, J., Chemical Diffusion Coefficient of Electrons in Nanostructured Semiconductor Electrodes and Dye-Sensitized Solar Cells. *The Journal of Physical Chemistry B* **2004**, *108* (7), 2323-2332.

-
96. Kopidakis, N.; Neale, N. R.; Zhu, K.; van de Lagemaat, J.; Frank, A. J., Spatial location of transport-limiting traps in TiO₂ nanoparticle films in dye-sensitized solar cells. *Applied Physics Letters* **2005**, *87* (20), 2021061-2021063.
97. Zhu, K.; Kopidakis, N.; Neale, N. R.; van de Lagemaat, J.; Frank, A. J., Influence of Surface Area on Charge Transport and Recombination in Dye-Sensitized TiO₂ Solar Cells. *The Journal of Physical Chemistry B* **2006**, *110* (50), 25174-25180.
98. Hagfeldt, A.; Boschloo, G.; Sun, L.; Kloo, L.; Pettersson, H., Dye-Sensitized Solar Cells. *Chemical Reviews* **2010**, *110* (11), 6595-6663.
99. Benkstein, K. D.; Kopidakis, N.; van de Lagemaat, J.; Frank, A. J., Influence of the Percolation Network Geometry on Electron Transport in Dye-Sensitized Titanium Dioxide Solar Cells. *The Journal of Physical Chemistry B* **2003**, *107* (31), 7759-7767.
100. Peter, L. M.; Wijayantha, K. G. U., Electron transport and back reaction in dye sensitized nanocrystalline photovoltaic cells. *Electrochimica Acta* **2000**, *45* (28), 4543-4551.
101. Frank A. J., Kopidakis N. and van de Lagemaat J., Electrons in nanostructured TiO₂ solar cells: transport, recombination and photovoltaic properties. *Coordination Chem. Rev.* **2004**, *248*, 1165–1179.
102. Ferber, J.; Stangl, R.; Luther, J., An electrical model of the dye-sensitized solar cell. *Solar Energy Materials and Solar Cells* **1998**, *53* (1-2), 29-54.

103. Hagfeldt, A.; Didriksson, B.; Palmqvist, T.; Lindström, H.; Södergren, S.; Rensmo, H.; Lindquist, S.-E., Verification of high efficiencies for the Grätzel-cell. A 7% efficient solar cell based on dye-sensitized colloidal TiO₂ films. *Solar Energy Materials and Solar Cells* **1994**, *31* (4), 481-488.

104. Papageorgiou, N.; Maier, W. F.; Gratzel, M., An Iodine/Triiodide Reduction Electrocatalyst for Aqueous and Organic Media. *Journal of The Electrochemical Society* **1997**, *144* (3), 876-884.

105. Hagfeldt, A.; Boschloo, G.; Sun, L.; Kloo, L.; Pettersson, H., Dye-Sensitized Solar Cells. *Chemical Reviews* **2010**, *110* (11), 6595-6663.

106. Papageorgiou, N.; Athanassov, Y.; Armand, M.; Bonhote, P.; Pettersson, H.; Azam, A.; Gratzel, M., The Performance and Stability of Ambient Temperature Molten Salts for Solar Cell Applications. *Journal of The Electrochemical Society* **1996**, *143* (10), 3099-3108.

107. Haque, S. A.; Tachibana, Y.; Klug, D. R.; Durrant, J. R., Charge Recombination Kinetics in Dye-Sensitized Nanocrystalline Titanium Dioxide Films under Externally Applied Bias. *The Journal of Physical Chemistry B* **1998**, *102* (10), 1745-1749.

108. Haque, S. A.; Tachibana, Y.; Willis, R. L.; Moser, J. E.; Gratzel, M.; Klug, D. R.; Durrant, J. R., Parameters influencing charge recombination kinetics in dye-sensitized nanocrystalline titanium dioxide films. *J. Phys. Chem. B* **2000**, *104* (3), 538-547.

109. Kuciauskas, D.; Freund, M. S.; Gray, H. B.; Winkler, J. R.; Lewis, N. S., Electron Transfer Dynamics in Nanocrystalline Titanium Dioxide Solar Cells Sensitized with Ruthenium or Osmium Polypyridyl Complexes. *The Journal of Physical Chemistry B* **2000**, *105* (2), 392-403.

-
110. Iijima, S., Helical Microtubules of Graphitic Carbon. *Nature* **1991**, *354* (6348), 56-58.
111. Saito, R.; Dresselhaus, G.; Dresselhaus, M.S., *Physical Properties of Carbon Nanotubes*, Imperial College Press, London, 1998.
112. Dirk, M. G.; Nazario, M., Carbon nanotubes and related structures: synthesis, characterization, functionalization, and applications (WILEY-VCH Verlag GmbH & Co. KGaA, Weinheim, **2010**).
113. Szabó, A.; Perri, C.; Csató, A.; Giordano, G.; Vuono, D.; Nagy, J. B., Synthesis Methods of Carbon Nanotubes and Related Materials. *Materials* **2010**, *3* (5), 3092-3140.
114. Popov, V. N., Carbon nanotubes: properties and application. *Materials Science and Engineering: R: Reports* **2004**, *43* (3), 61-102.
115. Journet, C.; Bernier, P., Production of carbon nanotubes. *Appl Phys A* **1998**, *67* (1), 1-9.
116. Terranova, M. L.; Sessa, V.; Rossi, M., The World of Carbon Nanotubes: An Overview of CVD Growth Methodologies. *Chemical Vapor Deposition* **2006**, *12* (6), 315-325.
117. Endo, M., Grow Carbon-Fibers in the Vapor-Phase. *Chemtech* **1988**, *18* (9), 568-576.
118. Tibbetts, G. G., Vapor-grown carbon fibers: Status and prospects. *Carbon* **1989**, *27* (5), 745-747.

-
119. Ci, L.; Wei, J.; Wei, B.; Liang, J.; Xu, C.; Wu, D., Carbon nanofibers and single-walled carbon nanotubes prepared by the floating catalyst method. *Carbon* **2001**, *39* (3), 329-335.
120. Ishioka, M.; Okada, T.; Matsubara, K., Formation and characteristics of vapor grown carbon fibers prepared in Linz-Donawitz converter gas. *Carbon* **1992**, *30* (7), 975-979.
121. Fonseca, A.; Hernadi, K.; Piedigrosso, P.; Colomer, J. F.; Mukhopadhyay, K.; Doome, R.; Lazarescu, S.; Biro, L. P.; Lambin, P.; Thiry, P. A.; Bernaerts, D.; Nagy, J. B., Synthesis of single- and multi-wall carbon nanotubes over supported catalysts. *Applied Physics A* **1998**, *67* (1), 11-22.
122. Ivanov, V.; Nagy, J. B.; Lambin, P.; Lucas, A.; Zhang, X. B.; Zhang, X. F.; Bernaerts, D.; Van Tendeloo, G.; Amelinckx, S.; Van Landuyt, J., The study of carbon nanotubules produced by catalytic method. *Chemical Physics Letters* **1994**, *223* (4), 329-335.
123. Colomer, J. F.; Stephan, C.; Lefrant, S.; Van Tendeloo, G.; Willems, I.; Kónya, Z.; Fonseca, A.; Laurent, C.; Nagy, J. B., Large-scale synthesis of single-wall carbon nanotubes by catalytic chemical vapor deposition (CCVD) method. *Chemical Physics Letters* **2000**, *317* (1-2), 83-89.
124. Mathur, A.; Tweedie, M.; Roy, S. S.; Maguire, P. D.; McLaughlin, J. A., Electrical and Raman Spectroscopic Studies of Vertically Aligned Multi-Walled Carbon Nanotubes. *Journal of Nanoscience and Nanotechnology* **2009**, *9* (7), 4392-4396.
125. Ren, Z. F.; Huang, Z. P.; Xu, J. W.; Wang, J. H.; Bush, P.; Siegal, M. P.; Provencio, P. N., Synthesis of Large Arrays of Well-Aligned Carbon Nanotubes on Glass. *Science* **1998**, *282* (5391), 1105.

126. Wang, N.; Tang, Z. K.; Li, G. D.; Chen, J. S., Materials science: Single-walled 4 A carbon nanotube arrays. *Nature* **2000**, *408* (6808), 50-55.

127. Melechko, A. V.; Merkulov, V. I.; McKnight, T. E.; Guillorn, M. A.; Klein, K. L.; Lowndes, D. H.; Simpson, M. L., Vertically aligned carbon nanofibers and related structures: Controlled synthesis and directed assembly. *Journal of Applied Physics* **2005**, *97* (4).

128. Zhang, G.; Mann, D.; Zhang, L.; Javey, A.; Li, Y.; Yenilmez, E.; Wang, Q.; McVittie, J. P.; Nishi, Y.; Gibbons, J.; Dai, H., Ultra-high-yield growth of vertical single-walled carbon nanotubes: Hidden roles of hydrogen and oxygen. *Proceedings of the National Academy of Sciences of the United States of America* **2005**, *102* (45), 16141-16145.

129. Seidel, R. V.; Graham, A. P.; Duesberg, G. S.; Liebau, M.; Unger, E., Kreupl, F.; Hoenlein, W., Faster and smaller with carbon nanotubes, Paper presented at the 12th GAAS Symposium, Amsterdam October 11–15, **2004**.

130. Unalan, H. E.; Fanchini, G.; Kanwal, A.; Du Pasquier, A.; Chhowalla, M., Design Criteria for Transparent Single-Wall Carbon Nanotube Thin-Film Transistors. *Nano Letters* **2006**, *6* (4), 677-682.

131. Cao, Q.; Hur, S. H.; Zhu, Z. T.; Sun, Y. G.; Wang, C. J.; Meitl, M. A.; Shim, M.; Rogers, J. A., Highly Bendable, Transparent Thin-Film Transistors That Use Carbon-Nanotube-Based Conductors and Semiconductors with Elastomeric Dielectrics. *Advanced Materials* **2006**, *18* (3), 304-309.

132. Li, J.; Hu, L.; Wang, L.; Zhou, Y.; Grüner, G.; Marks, T. J., Organic Light-Emitting Diodes Having Carbon Nanotube Anodes. *Nano Letters* **2006**, *6* (11), 2472-2477.

-
133. Takenobu, T.; Takahashi, T.; Kanbara, T.; Tsukagoshi, K.; Aoyagi, Y.; Iwasa, Y., High-performance transparent flexible transistors using carbon nanotube films. *Appl. Phys. Lett.* **2006**, *88* (3).
134. Das, R. K.; Liu, B.; Reynolds, J. R.; Rinzler, A. G., Engineered Macroporosity in Single-Wall Carbon Nanotube Films. *Nano Letters* **2009**, *9* (2), 677-683.
135. Trancik, J. E.; Barton, S. C.; Hone, J., Transparent and Catalytic Carbon Nanotube Films. *Nano Letters* **2008**, *8* (4), 982-987.
136. Liu, D.; Fina, M.; Guo, J. H.; Chen, X. B.; Liu, G.; Johnson, S. G.; Mao, S. S., Organic light-emitting diodes with carbon nanotube cathode-organic interface layer. *Applied Physics Letters* **2009**, *94* (1), 0131101-0131103.
137. Behnam, A.; Bosman, G.; Ural, A., Percolation scaling of $1/f$ noise in single-walled carbon nanotube films. *Physical Review B* **2008**, *78* (8), 085431.
138. Gruner, G., Carbon nanotube films for transparent and plastic electronics. *Journal of Materials Chemistry* **2006**, *16* (35), 3533-3539.
139. Cao, Q.; Rogers, J. A., Ultrathin Films of Single-Walled Carbon Nanotubes for Electronics and Sensors: A Review of Fundamental and Applied Aspects. *Advanced Materials* **2009**, *21* (1), 29-53.
140. Wu, Z.; Chen, Z.; Du, X.; Logan, J. M.; Sippel, J.; Nikolou, M.; Kamaras, K.; Reynolds, J. R.; Tanner, D. B.; Hebard, A. F.; Rinzler, A. G., Transparent, Conductive Carbon Nanotube Films. *Science* **2004**, *305* (5688), 1273-1276.

141. Burnside, S. D.; Shklover, V.; Barbe, C.; Comte, P.; Arendse, F.; Brooks, K.; Gratzel, M., Self-organization of TiO₂ nanoparticles in thin films. *Chemistry of Materials* **1998**, *10* (9), 2419-2425.

142. Kalyanasundaram, K., Grätzel, M., Applications of functionalized transition metal complexes in photonic and optoelectronic devices. *Coordination Chemistry Reviews* **1998**, *177*, 347-414.

143. Hagfeldt, A.; Didriksson, B.; Palmqvist, T.; Lindstrom, H.; Sodergren, S.; Rensmo, H.; Lindquist, S. E., Verification of High Efficiencies for the Gratzel-Cell - a 7-Percent Efficient Solar-Cell Based on Dye-Sensitized Colloidal TiO₂ Films. *Solar Energy Materials & Solar Cells C* **1994**, *31* (4), 481-488.

144. Barbe, C.J.; Arendse, F.; Comte, P.; Jirousek, M.; Lenmann, F.; Shklover, V.; Gratzel, M., Nanocrystalline Titanium Oxide Electrodes for Photovoltaic Applications. *Journal of American Ceramic Society* **1997**, *80* (12), 3157-71.

145. Ito, S.; Liska, P.; Comte, P.; Charvet, R.; Pechy, P.; Bach, U.; Schmidt-Mende, L.; Zakeeruddin, S. M.; Kay, A.; Nazeeruddin, M. K.; Gratzel, M., Control of dark current in photoelectrochemical (TiO₂/I⁻I₃⁻) and dye-sensitized solar cells. *Chemical Communications* **2005**, (34), 4351-4353.

146. Blackburn, J. L.; Barnes, T. M.; Beard, M. C.; Kim, Y. H.; Tenent, R. C.; McDonald, T. J.; To, B.; Coutts, T. J.; Heben, M. J., Transparent conductive single-walled carbon nanotube networks with precisely tunable ratios of semiconducting and metallic nanotubes. *Acs Nano* **2008**, *2* (6), 1266-1274.

147. Aguirre, C. M.; Auvray, S.; Pigeon, S.; Izquierdo, R.; Desjardins, P.; Martel, R., Carbon nanotube sheets as electrodes in organic light-emitting diodes. *Applied Physics Letters* **2006**, *88* (18), 1831041-1831043.

148. Jakubinek, M.B., Thermal and electrical conductivity of carbon nanotube materials. PhD Thesis, Dalhousie University, Halifax, Nova Scotia, **2009**.

149. Liu, C-K., Vertically aligned carbon nanotubes as proton exchange membrane fuel cell catalyst support. Master Thesis, Dalhousie University, Halifax, Nova Scotia, **2007**.

150. Chhowalla, M.; Teo, K. B. K.; Ducati, C.; Rupesinghe, N. L.; Amaratunga, G. A. J.; Ferrari, A. C.; Roy, D.; Robertson, J.; Milne, W. I., Growth process conditions of vertically aligned carbon nanotubes using plasma enhanced chemical vapor deposition. *Journal of Applied Physics* **2001**, *90* (10), 5308-5317.

151. Melechko, A. V.; Merkulov, V. I.; Lowndes, D. H.; Guillorn, M. A.; Simpson, M. L., Transition between 'base' and 'tip' carbon nanofiber growth modes. *Chemical Physics Letters* **2002**, *356* (5-6), 527-533.

152. Merkulov, V. I.; Guillorn, M. A.; Lowndes, D. H.; Simpson, M. L.; Voelkl, E., Shaping carbon nanostructures by controlling the synthesis process. *Applied Physics Letters* **2001**, *79* (8), 1178-1180.

153. Ma, J.; Park, C.; Rodriguez, N. M.; Baker, R. T. K., Characteristics of copper particles supported on various types of graphite nanofibers. *Journal of Physical Chemistry B* **2001**, *105* (48), 11994-12002.

-
154. Merkulov, V. I.; Hensley, D. K.; Melechko, A. V.; Guillorn, M. A.; Lowndes, D. H.; Simpson, M. L., Control mechanisms for the growth of isolated vertically aligned carbon nanofibers. *Journal of Physical Chemistry B* **2002**, *106* (41), 10570-10577.
155. Merkulov, V.; Melechko, A. V.; Guillorn, M. A.; Lowndes, D. H.; Simpson, M. L., Growth rate of plasma-synthesized vertically aligned carbon nanofibers. *Chem Phys Lett* **2002**, *361* (5-6), 492-498.
156. Kratschmer, W.; Lamb, L. D.; Fostiropoulos, K.; Huffman, D. R., Solid C-60 - a new form of carbon. *Nature* **1990**, *347* (6291), 354-358.
157. Kim, M. S.; Rodriguez, N. M.; Baker, R. T. K., The interaction of hydrocarbons with copper nickel and nickel in the formation of carbon filaments. *J. Catal.* **1991**, *131* (1), 60-73.
158. Brown, J. C.; Gulari, E., Hydrogen production from methanol decomposition over Pt/Al₂O₃ and ceria promoted Pt/Al₂O₃ catalysts. *Catalysis Communications* **2004**, *5* (8), 431-436.
159. Hakvoort, G.; Xiaoding, X., Decomposition of methanol vapour over solid catalyst, measured by DSC. *Journal of Thermal Analysis* **1991**, *37* (6), 1269-1279.
160. de Souza Lima, M. M.; Borsali, R., Rodlike Cellulose Microcrystals: Structure, Properties, and Applications. *Macromolecular Rapid Communications* **2004**, *25* (7), 771-787.
161. Elazzouzi-Hafraoui, S.; Nishiyama, Y.; Putaux, J.-L.; Heux, L.; Dubreuil, F.; Rochas, C., The Shape and Size Distribution of Crystalline Nanoparticles Prepared by Acid Hydrolysis of Native Cellulose. *Biomacromolecules* **2007**, *9* (1), 57-65.

-
162. Cranston, E. D.; Gray, D. G., Morphological and Optical Characterization of Polyelectrolyte Multilayers Incorporating Nanocrystalline Cellulose. *Biomacromolecules* **2006**, *7* (9), 2522-2530.
163. Hirschorn, B.; Orazem, M. E.; Tribollet, B.; Vivier, V.; Frateur, I.; Musiani, M., Constant-Phase-Element Behavior Caused by Resistivity Distributions in Films: I. Theory. *Journal of The Electrochemical Society* **2010**, *157* (12), C452-C457.
164. Briggs, D., Surface Analysis of Polymers by XPS and Static SIMS, vol. 1, p 49. Cambridge University Press, UK, **1998**.
165. Abowitz, G.; Arnold, E., Simple Mercury Drop Electrode for MOS Measurements. *Review of Scientific Instruments* **1967**, *38* (4), 564-565.
- ¹⁶⁶. Binnig, G.; Quate, C. F.; Gerber, C., Atomic Force Microscope. *Physical Review Letters* **1986**, *56* (9), 930-933.
167. Ramasamy, E.; Lee, W. J.; Lee, D. Y.; Song, J. S., Spray coated multi-wall carbon nanotube counter electrode for tri-iodide reduction in dye-sensitized solar cells. *Electrochemistry Communications* **2008**, *10* (7), 1087-1089.
168. Won Jae Lee, Easwaramoorthi Ramasamy, Dong Yoon Lee, Bok Ki Min and Jae Sung Song, "Dye-sensitized solar cells with spray-coated CNT counter electrode", Proc. SPIE 6038, 60381T, **2005**.
169. Lee, W. J.; Ramasamy, E.; Lee, D. Y.; Song, J. S., Efficient Dye-Sensitized Cells with Catalytic Multiwall Carbon Nanotube Counter Electrodes. *ACS Applied Materials & Interfaces* **2009**, *1* (6), 1145-1149.

170. Huang S, Sun H, Huang X, Zhang Q, Li D, Luo Y, Meng Q. Carbon nanotube counter electrode for high-efficient fibrous dye-sensitized solar cells. *Nanoscale Research Letters*, **2012** ,7(1), 222.

171. Lee,W.J., Lee, D.Y., Kim, I.S., Jeong, S.J., and Song, J.S., Spray-coated carbon nanotube counter electrodes for dye-sensitized solar cells, *Transactions on Electrical And Electronics Materials*, **2005**, 6 (4), 140–143.

172 Dong, P.; Pint, C. L.; Hainey, M.; Mirri, F.; Zhan, Y.; Zhang, J.; Pasquali, M.; Hauge, R. H.; Verduzco, R.; Jiang, M.; Lin, H.; Lou, J., Vertically Aligned Single-Walled Carbon Nanotubes as Low-cost and High Electrocatalytic Counter Electrode for Dye-Sensitized Solar Cells. *ACS Applied Materials & Interfaces* **2011**, 3 (8), 3157-3161.

173 Hao, F.; Dong, P.; Zhang, J.; Zhang, Y. C.; Loya, P. E.; Hauge, R. H.; Li, J. B.; Lou, J.; Lin, H., High Electrocatalytic Activity of Vertically Aligned Single-Walled Carbon Nanotubes towards Sulfide Redox Shuttles. *Scientific Reports* **2012**, 368 (2), 1-6.

174. Robert A. Sayer, Stephen L. Hodson, and Timothy S. Fisher. Improved Efficiency of Dye-Sensitized Solar Cells Using a Vertically Aligned Carbon Nanotube Counter Electrode. *Journal of Solar Energy Engineering* 132.2 (**2010**): 021007.

175. Li, S.; Luo, Y.; Lv, W.; Yu, W.; Wu, S.; Hou, P.; Yang, Q.; Meng, Q.; Liu, C.; Cheng, H.-M., Vertically Aligned Carbon Nanotubes Grown on Graphene Paper as Electrodes in Lithium-Ion Batteries and Dye-Sensitized Solar Cells. *Advanced Energy Materials* **2011**, 1 (4), 486-490.

176. Rånby, B. G., Aqueous Colloidal Solutions of Cellulose Micelles. *Acta Chemica Scandinavica* **1949**, *3*, 649-650.

177. Van den Berg, O.; Schroeter, M.; Capadona, J. R.; Weder, C., Nanocomposites based on cellulose whiskers and (semi)conducting conjugated polymers. *Journal of Materials Chemistry* **2007**, *17* (26), 2746-2753.

178. Dufresne, A., Processing of Polymer nanocomposites reinforced with polysaccharide nanocrystals,” *Molecules* **2010**, *15*, 4111–4128.

179. Maren, R.; Shuping, D.; Anjali, H.; Yong Woo, L., Cellulose Nanocrystals for Drug Delivery. In *Polysaccharide Materials: Performance by Design*, American Chemical Society **2009**, 1017, 81-91.

180. Azizi Samir, M. A. S.; Alloin, F.; Gorecki, W.; Sanchez, J.-Y.; Dufresne, A., Nanocomposite Polymer Electrolytes Based on Poly(oxyethylene) and Cellulose Nanocrystals. *The Journal of Physical Chemistry B* **2004**, *108* (30), 10845-10852.

181. Zhou, Y.; Fuentes-Hernandez, C.; Khan, T. M.; Liu, J.-C.; Hsu, J.; Shim, J. W.; Dindar, A.; Youngblood, J. P.; Moon, R. J.; Kippelen, B., Recyclable organic solar cells on cellulose nanocrystal substrates. *Scientific Reports* **2013**, *3*.

182. Lin, Y.-C.; Cho, J.; Tompsett, G. A.; Westmoreland, P. R.; Huber, G. W., Kinetics and Mechanism of Cellulose Pyrolysis. *The Journal of Physical Chemistry C* **2009**, *113* (46), 20097-20107.

183. Ishida, O.; Kim, D. Y.; Kuga, S.; Nishiyama, Y.; Brown, R. M., Microfibrillar carbon from native cellulose. *Cellulose* **2004**, *11* (3-4), 475-480.

184. Habibi, Y.; Lucia, L. A.; Rojas, O. J., Cellulose Nanocrystals: Chemistry, Self-Assembly, and Applications. *Chemical Reviews* **2010**, *110* (6), 3479-3500.

185. Amutio, M.; Lopez, G.; Aguado, R.; Artetxe, M.; Bilbao, J.; Olazar, M., Kinetic study of lignocellulosic biomass oxidative pyrolysis. *Fuel* **2012**, *95* (0), 305-311.

186. Fang, M. X.; Shen, D. K.; Li, Y. X.; Yu, C. J.; Luo, Z. Y.; Cen, K. F., Kinetic study on pyrolysis and combustion of wood under different oxygen concentrations by using TG-FTIR analysis. *Journal of Analytical and Applied Pyrolysis* **2006**, *77* (1), 22-27.

187. Li, J.; Zhang, Y., A simple purification for single-walled carbon nanotubes. *Physica E: Low-dimensional Systems and Nanostructures* **2005**, *28* (3), 309-312.

188. Landi, B. J.; Cress, C. D.; Evans, C. M.; Raffaele, R. P., Thermal Oxidation Profiling of Single-Walled Carbon Nanotubes. *Chemistry of Materials* **2005**, *17* (26), 6819-6834.

189. Shopsowitz, K. E.; Hamad, W. Y.; MacLachlan, M. J., Chiral Nematic Mesoporous Carbon Derived From Nanocrystalline Cellulose. *Angewandte Chemie International Edition* **2011**, *50* (46), 10991-10995.

190. Brennan, B. J.; Llansola Portoles, M. J.; Liddell, P. A.; Moore, T. A.; Moore, A. L.; Gust, D., Comparison of silatrane, phosphonic acid, and carboxylic acid functional groups for attachment of porphyrin sensitizers to TiO₂ in photoelectrochemical cells. *Physical Chemistry Chemical Physics* **2013**, *15* (39), 16605-16614.

191. Bae, E.; Choi, W.; Park, J.; Shin, H. S.; Kim, S. B.; Lee, J. S., Effects of Surface Anchoring Groups (Carboxylate vs Phosphonate) in Ruthenium-Complex-Sensitized

TiO₂ on Visible Light Reactivity in Aqueous Suspensions. *The Journal of Physical Chemistry B* **2004**, 108 (37), 14093-14101.

192. Bauer, T.; Schmaltz, T.; Lenz, T.; Halik, M.; Meyer, B.; Clark, T., Phosphonate- and Carboxylate-Based Self-Assembled Monolayers for Organic Devices: A Theoretical Study of Surface Binding on Aluminum Oxide with Experimental Support. *ACS Applied Materials & Interfaces* **2013**, 5 (13), 6073-6080.

193. Ernstorfer, R.; Gundlach, L.; Felber, S.; Storck, W.; Eichberger, R.; Willig, F., Role of Molecular Anchor Groups in Molecule-to-Semiconductor Electron Transfer. *Journal of Physical Chemistry B* **2006**, 110, 25383-25391.

194. Nilsing, M.; Persson, P.; Lunell, S.; Ojamae, L., Dye-Sensitization of the TiO₂ Rutile (110) Surface by Perylene Dyes: Quantum-Chemical Periodic B3LYP Computations. *Journal of Physical Chemistry C* **2007**, 111, 12116-12123.

195. Ambrosio, F.; Martsinovich, N.; Troisi, A., Effect of the Anchoring Group on Electron Injection: Theoretical Study of Phosphonated Dyes for Dye-Sensitized Solar Cells. *Journal of Physical Chemistry C* **2012**, 116, 2622-2629.

196. Chen, R. K.; Yang, X. C.; Tian, H. N.; Wang, X. N.; Hagfeldt, A.; Sun, L. C., Effect of Tetrahydroquinoline Dyes Structure on the Performance of Organic Dye-Sensitized Solar Cells. *Chemistry of Materials* **2007**, 19, 4007-4015

197. Mulhern, K. R.; Orchard, A.; Watson, D. F.; Detty, M. R., Influence of Surface-Attachment Functionality on the Aggregation, Persistence, and Electron-Transfer Reactivity of Chalcogenorhodamine Dyes on TiO₂. *Langmuir* **2012**, 28, 7071-7082.

198. Rensmo, H.; Westermark, K.; Sodergren, S.; Kohle, O.; Persson, P.; Lunell, S.; Siegbahn, H., XPS Studies of Ru-Polypyridine Complexes for solar Cell Applications. *Journal of Chemical Physics* **1999**, *111*, 2744-2750.

199. Wu, K.-L.; Li, C.-H.; Chi, Y.; Clifford, J. N.; Cabau, L.; Palomares, E.; Cheng, Y.-M.; Pan, H.-A.; Chou, P.-T., Dye Molecular Structure Device Open-Circuit Voltage Correlation in Ru(II) Sensitizers with Heteroleptic Tridentate Chelates for Dye-Sensitized Solar Cells. *Journal of American Chemical Society* **2012**, *134*, 7488-7496.

200. Liao, K.-C.; Anwar, H.; Hill, I. G.; Vertelov, G. K.; Schwartz, J., Comparative Interface Metrics for Metal-Free Monolayer-Based Dye-Sensitized Solar Cells. *ACS Applied Materials & Interfaces* **2012**, *4* (12), 6735-6746.

201. Tour, J. M.; Wu, R. L., Synthesis and UV-Visible Properties of Soluble α -Thiophene Oligomers - Monomer to Octamer. *Macromolecules* **1992**, *25*, 1901-1907.

202. Hanson, E. L.; Schwartz, J.; Nickel, B.; Koch, N.; Danisman, M. F., Bonding Self-Assembled, Compact Organophosphonate Monolayers to the Native Oxide Surface of Silicon. *Journal of the American Chemical Society* **2003**, *125* (51), 16074-16080.

203. Mishra, A.; Fischer, M. K. R.; Bauerle, P., Metal-Free Organic Dyes for Dye-Sensitized Solar Cells: From Structure: Property Relationships to Design Rules. *Angewandte Chemie International Edition* **2009**, *48*, 2474-2499.

204. Hau, S. K.; Cheng, Y.-J.; Yip, H.-L.; Zhang, Y.; Ma, H.; Jen, A. K. Y., Effect of Chemical Modification of Fullerene-Based Self-Assembled Monolayers on the

Performance of Inverted Polymer Solar Cells. *ACS Applied Materials & Interfaces* **2010**, *2*, 1892-1902.

205. Montalti, M.; Wadhwa, S.; Kim, W. Y.; Kipp, R. A.; Schmehl, R. H., Luminescent Ruthenium(II) Bipyridyl–Phosphonic Acid Complexes: pH Dependent Photophysical Behavior and Quenching with Divalent Metal Ions. *Inorganic Chemistry* **1999**, *39*, 76-84.

206. Gratzel, M., Photoelectrochemical cells. *Nature* **2001**, *414* (6861), 338-344.

207. Boschloo, G.; Gibson, E. A.; Hagfeldt, A., Photomodulated Voltammetry of Iodide/Triiodide Redox Electrolytes and Its Relevance to Dye-Sensitized Solar Cells. *The Journal of Physical Chemistry Letters* **2011**, *2* (24), 3016-3020.

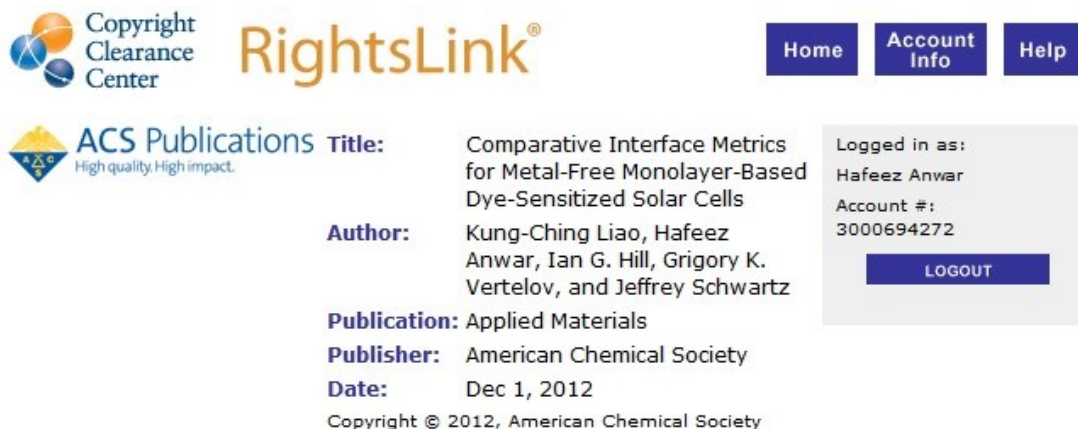
208. Grätzel, M., Dye-sensitized solar cells. *Journal of Photochemistry and Photobiology C: Photochemistry Reviews* **2003**, *4* (2), 145-153.

209. Sze, S., M. Physics of Semiconductor Devices, 2nd ed.; John Wiley & Sons: New York, **1981**.

APPENDIX

This portion contains license permission of my publications from publishers to use in my dissertation.

LICENSE PERMISSION 1



The screenshot displays the Copyright Clearance Center RightsLink interface. At the top left is the Copyright Clearance Center logo. To its right is the RightsLink logo. Further right are three navigation buttons: Home, Account Info, and Help. Below the logos is the ACS Publications logo with the tagline "High quality. High impact." The main content area lists the following details:

- Title:** Comparative Interface Metrics for Metal-Free Monolayer-Based Dye-Sensitized Solar Cells
- Author:** Kung-Ching Liao, Hafeez Anwar, Ian G. Hill, Grigory K. Vertelov, and Jeffrey Schwartz
- Publication:** Applied Materials
- Publisher:** American Chemical Society
- Date:** Dec 1, 2012

At the bottom of this section is the copyright notice: Copyright © 2012, American Chemical Society. On the right side of the interface, there is a user login box showing "Logged in as: Hafeez Anwar" and "Account #: 3000694272" with a LOGOUT button.

PERMISSION/LICENSE IS GRANTED FOR YOUR ORDER AT NO CHARGE

This type of permission/license, instead of the standard Terms & Conditions, is sent to you because no fee is being charged for your order. Please note the following:

- Permission is granted for your request in both print and electronic formats, and translations.
- If figures and/or tables were requested, they may be adapted or used in part.
- Please print this page for your records and send a copy of it to your publisher/graduate school.
- Appropriate credit for the requested material should be given as follows: "Reprinted (adapted) with permission from (COMPLETE REFERENCE CITATION). Copyright (YEAR) American Chemical Society." Insert appropriate information in place of the capitalized words.
- One-time permission is granted only for the use specified in your request. No additional uses are granted (such as derivative works or other editions). For any other uses, please submit a new request.

LICENSE PERMISSION 2

ELSEVIER LICENSE TERMS AND CONDITIONS

This is a License Agreement between Hafeez Anwar ("You") and Elsevier ("Elsevier") provided by Copyright Clearance Center ("CCC"). The license consists of your order details, the terms and conditions provided by Elsevier, and the payment terms and conditions.

All payments must be made in full to CCC. For payment instructions, please see information listed at the bottom of this form.

Supplier	Elsevier Limited The Boulevard,Langford Lane Kidlington,Oxford,OX5 1GB,UK 1982084
Registered Company Number	1982084
Customer name	Hafeez Anwar
Customer address	Dept Physics & Atmospheric Science Halifax, NS B3H 4R2
License number	3225031068068
License date	Sep 09, 2013
Licensed content publisher	Elsevier
Licensed content publication	Solar Energy
Licensed content title	Vertically-aligned carbon nanotube counter electrodes for dye-sensitized solar cells
Licensed content author	Hafeez Anwar,Andrew E. George,Ian G. Hill
Licensed content date	February 2013
Licensed content volume number	88
Licensed content issue number	
Number of pages	8
Start Page	129
End Page	136
Type of Use	reuse in a thesis/dissertation
Portion	full article
Format	electronic
Are you the author of this Elsevier article?	Yes
Will you be translating?	No
Order reference number	
Title of your thesis/dissertation	Precious Metal-free Dye-sensitized Solar Cells
Expected completion date	Dec 2013
Estimated size (number of pages)	160
Elsevier VAT number	GB 494 6272 12
Permissions price	0.00 USD

VAT/Local Sales Tax	0.0 USD / 0.0 GBP
Total	0.00 USD
Terms and Conditions	

INTRODUCTION

1. The publisher for this copyrighted material is Elsevier. By clicking "accept" in connection with completing this licensing transaction, you agree that the following terms and conditions apply to this transaction (along with the Billing and Payment terms and conditions established by Copyright Clearance Center, Inc. ("CCC"), at the time that you opened your Rightslink account and that are available at any time at <http://myaccount.copyright.com>).

GENERAL TERMS

2. Elsevier hereby grants you permission to reproduce the aforementioned material subject to the terms and conditions indicated.

3. Acknowledgement: If any part of the material to be used (for example, figures) has appeared in our publication with credit or acknowledgement to another source, permission must also be sought from that source. If such permission is not obtained then that material may not be included in your publication/copies. Suitable acknowledgement to the source must be made, either as a footnote or in a reference list at the end of your publication, as follows:

“Reprinted from Publication title, Vol /edition number, Author(s), Title of article / title of chapter, Pages No., Copyright (Year), with permission from Elsevier [OR APPLICABLE SOCIETY COPYRIGHT OWNER].” Also Lancet special credit - “Reprinted from The Lancet, Vol. number, Author(s), Title of article, Pages No., Copyright (Year), with permission from Elsevier.”

4. Reproduction of this material is confined to the purpose and/or media for which permission is hereby given.

5. Altering/Modifying Material: Not Permitted. However figures and illustrations may be altered/adapted minimally to serve your work. Any other abbreviations, additions, deletions and/or any other alterations shall be made only with prior written authorization of Elsevier Ltd. (Please contact Elsevier at permissions@elsevier.com)

6. If the permission fee for the requested use of our material is waived in this instance, please be advised that your future requests for Elsevier materials may attract a fee.

7. Reservation of Rights: Publisher reserves all rights not specifically granted in the combination of (i) the license details provided by you and accepted in the course of this licensing transaction, (ii) these terms and conditions and (iii) CCC's Billing and Payment terms and conditions.

8. License Contingent Upon Payment: While you may exercise the rights licensed immediately upon issuance of the license at the end of the licensing process for the transaction, provided that you have disclosed complete and accurate details of your proposed use, no license is finally effective unless and until full payment is received from you (either by publisher or by CCC) as provided in CCC's Billing and Payment terms and conditions. If full payment is not received on a timely basis, then any license preliminarily granted shall be deemed automatically revoked and shall be void as if never granted. Further, in the event that you breach any of these terms and conditions or any of CCC's Billing and Payment terms and conditions, the license is automatically revoked and shall be void as if never granted. Use of materials as described in a revoked license, as well as any use of the materials beyond the scope of an unrevoked license, may constitute copyright infringement and publisher reserves the right to take any and all action to protect its copyright in the materials.

9. Warranties: Publisher makes no representations or warranties with respect to the licensed material.

10. Indemnity: You hereby indemnify and agree to hold harmless publisher and CCC, and their respective officers, directors, employees and agents, from and against any and

all claims arising out of your use of the licensed material other than as specifically authorized pursuant to this license.

11. No Transfer of License: This license is personal to you and may not be sublicensed, assigned, or transferred by you to any other person without publisher's written permission.

12. No Amendment Except in Writing: This license may not be amended except in a writing signed by both parties (or, in the case of publisher, by CCC on publisher's behalf).

13. Objection to Contrary Terms: Publisher hereby objects to any terms contained in any purchase order, acknowledgment, check endorsement or other writing prepared by you, which terms are inconsistent with these terms and conditions or CCC's Billing and Payment terms and conditions. These terms and conditions, together with CCC's Billing and Payment terms and conditions (which are incorporated herein), comprise the entire agreement between you and publisher (and CCC) concerning this licensing transaction. In the event of any conflict between your obligations established by these terms and conditions and those established by CCC's Billing and Payment terms and conditions, these terms and conditions shall control.

14. Revocation: Elsevier or Copyright Clearance Center may deny the permissions described in this License at their sole discretion, for any reason or no reason, with a full refund payable to you. Notice of such denial will be made using the contact information provided by you. Failure to receive such notice will not alter or invalidate the denial. In no event will Elsevier or Copyright Clearance Center be responsible or liable for any costs, expenses or damage incurred by you as a result of a denial of your permission request, other than a refund of the amount(s) paid by you to Elsevier and/or Copyright Clearance Center for denied permissions.

LIMITED LICENSE

The following terms and conditions apply only to specific license types:

15. **Translation:** This permission is granted for non-exclusive world **English** rights only unless your license was granted for translation rights. If you licensed translation rights you may only translate this content into the languages you requested. A professional translator must perform all translations and reproduce the content word for word preserving the integrity of the article. If this license is to re-use 1 or 2 figures then permission is granted for non-exclusive world rights in all languages.

16. **Website:** The following terms and conditions apply to electronic reserve and author websites: **Electronic reserve:** If licensed material is to be posted to website, the web site is to be password-protected and made available only to bona fide students registered on a relevant course if: This license was made in connection with a course, This permission is granted for 1 year only. You may obtain a license for future website posting, All content posted to the web site must maintain the copyright information line on the bottom of each image, A hyper-text must be included to the Homepage of the journal from which you are licensing at <http://www.sciencedirect.com/science/journal/xxxxx> or the Elsevier homepage for books at <http://www.elsevier.com> , and Central Storage: This license does not include permission for a scanned version of the material to be stored in a central repository such as that provided by Heron/XanEdu.

17. **Author website** for journals with the following additional clauses:

All content posted to the web site must maintain the copyright information line on the bottom of each image, and the permission granted is limited to the personal version of your paper. You are not allowed to download and post the published electronic version of your article (whether PDF or HTML, proof or final version), nor may you scan the printed edition to create an electronic version. A hyper-text must be included to the Homepage of the journal from which you are licensing at <http://www.sciencedirect.com/science/journal/xxxxx> . As part of our normal production process, you will receive an e-mail notice when your article appears on Elsevier's online service ScienceDirect (www.sciencedirect.com). That e-mail will include the article's Digital Object Identifier (DOI). This number provides the electronic link to the published

article and should be included in the posting of your personal version. We ask that you wait until you receive this e-mail and have the DOI to do any posting.

Central Storage: This license does not include permission for a scanned version of the material to be stored in a central repository such as that provided by Heron/XanEdu.

18. **Author website** for books with the following additional clauses:

Authors are permitted to place a brief summary of their work online only. A hyper-text must be included to the Elsevier homepage at <http://www.elsevier.com> . All content posted to the web site must maintain the copyright information line on the bottom of each image. You are not allowed to download and post the published electronic version of your chapter, nor may you scan the printed edition to create an electronic version.

Central Storage: This license does not include permission for a scanned version of the material to be stored in a central repository such as that provided by Heron/XanEdu.

19. **Website** (regular and for author): A hyper-text must be included to the Homepage of the journal from which you are licensing at <http://www.sciencedirect.com/science/journal/xxxxx>. or for books to the Elsevier homepage at <http://www.elsevier.com>

20. **Thesis/Dissertation**: If your license is for use in a thesis/dissertation your thesis may be submitted to your institution in either print or electronic form. Should your thesis be published commercially, please reapply for permission. These requirements include permission for the Library and Archives of Canada to supply single copies, on demand, of the complete thesis and include permission for UMI to supply single copies, on demand, of the complete thesis. Should your thesis be published commercially, please reapply for permission.

21. **Other Conditions**:

v1.6

If you would like to pay for this license now, please remit this license along with your payment made payable to "COPYRIGHT CLEARANCE CENTER" otherwise you will be invoiced within 48 hours of the license date. Payment should be in the form of a check or money order referencing your account number and this invoice number RLNK501108854. Once you receive your invoice for this order, you may pay your invoice by credit card. Please follow instructions provided at that time.

Make Payment To: Copyright Clearance Center Dept 001 P.O. Box 843006 Boston, MA 02284-3006

For suggestions or comments regarding this order, contact RightsLink Customer Support: customercare@copyright.com or +1-877-622-5543 (toll free in the US) or +1-978-646-2777.

Gratis licenses (referencing \$0 in the Total field) are free. Please retain this printable license for your reference. No payment is required.